

Evaluation of Enhanced Oil Recovery Application in Tight-Oil Formations

by

Son Thai Tran

A thesis submitted in partial fulfillment of the requirements for the degree of

Doctor of Philosophy

in

Petroleum Engineering

Department of Civil and Environmental Engineering

University of Alberta

© Son Thai Tran, 2021

Abstract

The rapid decline rates and low oil recovery factor (typically less than 10% of the original oil in place) of primary production are well-known challenges in the development of tight-oil formations. Several enhanced-oil-recovery studies and field trials have been conducted with promising results in these formations, however, key oil-recovery mechanisms are poorly understood. This research evaluates mechanisms controlling oil recovery during a natural-gas huff ‘n’ puff (HnP) and fracturing-fluid (FF) leakoff/flowback processes in tight-oil formations.

The main focuses are to investigate gas-transport and oil-recovery mechanisms during a gas HnP process under zero irreducible water saturation (S_{wirr}); and changes in oil effective permeability (k_o^{eff}) caused by FF-leakoff/flowback under $S_{\text{wirr}} > 0$. First, systematic phase-behavior and natural-gas (C_1 and a mixture of $C_1/C_2:70/30$ mol%) HnP studies using Montney fluid/rock samples are conducted to understand the controlling mechanism of gas transport into the plug during injection/soaking and oil recovery during the whole process. Furthermore, Péclet number (N_{Pe}) analysis is performed to quantify the contribution of gas-transport mechanisms during the soaking period. Second, coreflooding tests are performed on Midale carbonate core plugs with a range of porosity and permeability to simulate leakoff/flowback processes. Measured k_o^{eff} before (baseline) and after the leakoff process are compared to evaluate the effects of leakoff fluid properties (FF with nonionic surfactants and fresh water), shut-in duration (3 and 14 days), and rock properties on regained permeability values.

Key conclusions drawn from the phase-behavior and natural-gas HnP studies show that molecular diffusion is the dominant gas-transport mechanism during the soaking period of

the HnP tests ($N_{Pe} = 0.26$ to 0.62). The advective-gas flow caused by differential pressure during gas injection leads to improved gas transport into the plug ($N_{Pe} = 1.58$ to 3.03). Total system compressibility, oil swelling, and vaporization of oil components into the gas phase are the recovery mechanisms observed during gas injection and soaking periods, while gas expansion is the main recovery mechanism during depressurization phase. Overall, gas expansion is the dominant recovery mechanism, accounting for approximately 90% of the oil recovery. During the “puff” period, the expansion and flow of diffused gas drag the oil along its flowpaths, resulting in a significant flow of oil and gas observed on the surface of the plug. The enrichment of injected gas by 30 mol% C₂ enhances the transport of gas into the plug and increases oil recovery compared to pure C₁ cases. According to the results of constant-composition-expansion tests and minimum-miscibility-pressure measurements, increasing C₂ mole fraction in the injection gas significantly reduces minimum miscibility pressure of the oil/gas system and increases the oil-swelling factor.

The results of leakoff/flowback experiments show that adding appropriate surfactants in FF not only significantly reduces k_o^{eff} impairment caused by leakoff, but also improves k_o^{eff} compared with the baseline for a tight plug. FF (with surfactants) significantly reduces effects of aqueous phase trapping and improves k_o^{eff} during flowback compared with fresh water. In terms of shut-in duration, extending the shut-in time does not significantly affect the k_o^{eff} in high-permeability plugs. However, an increase in k_o^{eff} is observed in the tight plug, and this improvement significantly increases by increasing shut-in time. Overall, the improvement in regained k_o^{eff} is primarily because of the reduction of interfacial tension by the surfactants. In the tight plug, the interfacial tension reduction is attributed to the effective mixing of the invaded FF with initial oil/brine, supported by pore-throat size distribution and measured water saturation data.

Preface

Part of Chapter 2 and Chapters 3 and 4 are published in a peer-reviewed journal as Tran, S.; Eghbali, S.; Dehghanpour, H. 2020. Studying Phase Behavior of Oil-Natural Gas Systems for Designing Gas Injection Operations: A Montney Case Study. SPE-201109-PA. *Society of Petroleum Engineers (SPE) Reservoir Evaluation & Engineering Journal.*

Part of Chapter 2 and Chapters 5 and 6 are published in a peer-reviewed journal as Tran, S.; Yassin, M.R; Eghbali, S.; Doranehgard, M.H.; Dehghanpour, H. 2020. Quantifying Oil-Recovery Mechanisms during Natural-Gas Huff ‘n’ Puff Experiments on Ultratight Core Plugs. SPE-200341-PA. In press, *SPE Journal.*

Part of Chapters 2 and 7 are published in a peer-reviewed journal as Tran, S.; Habibi, A; Dehghanpour, H; Hazelton, M.; Rose, J. 2020. Leakoff and Flowback Experiments on Tight Carbonate Core Plugs. SPE-199252-PA. In press, *SPE Drilling & Completion Journal.*

I am responsible for experimental design, running the experiments, performing modeling works, writing, and editing the papers. My co-authors are responsible for providing rocks/fluids samples and relevant data, helping me with experimental and modeling works, providing useful comments and discussions on field practices, and reviewing the manuscript drafts.

Dedication

To my devoted parents, Trần Văn Ký and Mai Thị Bưởi;
and my lovely wife, Ngô Huy Hạnh

Acknowledgments

I would like to express my sincere gratitude to my supervisor, Dr. Hassan Dehghanpour, who not only admitted me to the research group but also helped me to find and define my research focus from scratch. I cannot imagine getting through this program without his undying support, fascinating research ideas, steady encouragement, and friendship.

I would like to especially thank my supervisory committee members, Dr. Alireza Nouri and Dr. Nobuo Maeda, for their questions, suggestions, and guidance throughout the research program. I thank Dr. Selma Guigard and Dr. Mohtada Sadrzadeh for their insightful suggestions during the Candidacy Exam to focus on quantifying the gas-transport mechanism during the soaking period and uncertainties associated with silicone coating. I thank Dr. Jeff Rose, Mr. Brady Webb, Mr. Mike Hazelton, and Mr. Mark Forbes for their thoughtful technical advice to improve the quality of this work.

I am indebted to the Canada First Research Excellence Fund through the University of Alberta-Future Energy Systems (Project T07-P05), and the Natural Sciences and Engineering Research Council for their financial support.

My appreciation is extended towards my colleagues in the research group (Sara Eghbali, Yanmin Xu, Mahmood Reza Yassin, Ali Habibi, Obinna Ezulike, Ashkan Zolfaghari Sharak, Mingxiang Xu, Yingkun Fu, Mohammad Doranehgard, Mohammad Youselfi, Tamer Moussa, Lin Yuan, Maryam Eghvabla, Taregh Soleiman Asl, Khan Athar, and Serge Pegov) for their valuable contributions, fruitful discussions, and encouragement. Furthermore, I appreciate the help of knowledgeable faculty members especially Mr. Todd Kinnee and Mr. John Czuroska who helped me with laboratory experiments.

Table of Contents

Abstract	ii
Preface	iv
Dedication.....	v
Acknowledgments	vi
Table of Contents	vii
List of Tables.....	xi
List of Figures.....	xv
Nomenclature	xix
Chapter 1 : Introduction	1
1.1. Research Motivation	1
1.2. Hypothesis	2
1.3. Research Objectives.....	4
1.4. Dissertation Outline.....	5
Chapter 2 : Background of Enhanced Oil Recovery Applications in Tight-Oil Formations ..	7
2.1. Unconventional Resources.....	7
2.2. Natural-Gas HnP Process in Tight-Oil Formations	12
2.3. Aqueous Phasing Trapping after Hydraulic Fracturing and Remediation Methods .	19
Chapter 3 : Experimental Study on The Phase Behavior of Natural-Gas/Oil Systems	23
3.1. Introduction	23
3.2. Materials.....	23
3.3. Method.....	24
3.4. Results and Discussions.....	31
3.4.1. Measured MMPs of Natural-Gas/Oil Systems	31
3.4.2. Results of CCE Tests	32

3.4.3.	Calculated Oil Density at Different P and T	34
3.4.4.	Visualization of Gas/Oil Interactions at The Interface	36
3.5.	Limitations.....	41
3.6.	Summary	41
	Chapter 4 : Modelling Phase Behavior of Natural-Gas/Oil Systems.....	43
4.1.	Introduction	43
4.2.	Method.....	43
4.3.	Results and Discussions.....	47
4.3.1.	Calibrating EOS Model with Four PCs.....	47
4.3.2.	Calibrating EOS Models with Two and One PCs.....	51
4.3.3.	Thermodynamic Consistency Checks.....	52
4.3.4.	MMP Prediction using Pseudoternary Diagrams	54
4.4.	Limitations.....	57
4.5.	Summary	58
	Chapter 5 : Experimental Study of Gas-Transport and Recovery Mechanisms during A Natural-Gas Huff ‘n’ Puff Cycle	59
5.1.	Introduction	59
5.2.	Materials.....	59
5.3.	Method.....	63
5.4.	Results and Discussions.....	69
5.4.1.	Gas-Transport Mechanisms during Soaking Period.....	69
5.4.2.	Visualization and Quantification of Oil-Recovery Mechanisms during A Natural-Gas HnP Cycle.....	72
5.4.3.	Oil-Recovery Mechanism during Depressurization Phase.....	80
5.5.	Limitations.....	84
5.6.	Summary	85
	Chapter 6 : Quantification of Gas-Transport Mechanisms during Soaking Period of The Natural-Gas HnP Process.....	86

6.1.	Introduction	86
6.2.	Method.....	86
6.3.	Results and Discussions.....	90
6.3.1.	Estimation of D and D_{eff}	90
6.3.2.	Péclet Number Analysis.....	92
6.4.	Limitations.....	97
6.5.	Summary	97
	Chapter 7 : Evaluation of Aqueous Phase Trapping and Remediation Methods.....	99
7.1.	Introduction	99
7.2.	Materials.....	99
7.3.	Method.....	108
7.4.	Results and Discussions.....	115
7.4.1.	Effect of Leakoff Fluids.....	119
7.4.2.	Effect of Shut-In Times	121
7.4.3.	Effect of Plug Properties.....	127
7.5.	Limitations.....	128
7.6.	Summary	128
	Chapter 8 : Conclusions and Future Work	130
8.1.	Conclusions	130
8.2.	Significance of The Work to Unconventional Field Practices.....	131
8.3.	Future Work	134
	Bibliography	135
	Appendices.....	164
	Appendix A. Oil Compositional Analysis, Measured Density Data, One- and Two-PC PR-EOS Calibration, and Two-Phase Equilibrium Data of Different PR-EOS Models	164
	Appendix B. Supplementary Material, Pressure-Decline Data, and Summary of k -plane Data Clustering Method	174

Appendix C. Composition of Midale Reservoir Brine and Physical Properties of the Surfactants	196
--	-----

List of Tables

Table 3–1: Physical properties of the Montney dead oil, and C ₁ /C ₂ (NIST chemistry webbook) at T _{set}	24
Table 3–2: Experimental conditions of the CCE tests using the PVT cell. The temperature is kept at 50°C in all tests.....	28
Table 3–3: Results of the two visualization tests.....	36
Table 4–1: Properties of components in the four-PC EOS model calibrated against oil/C ₁ CCE and MMP data.....	48
Table 4–2: Optimized BIP of the four-PC EOS model calibrated against oil/C ₁ CCE and MMP data	48
Table 4–3: Comparison of the measured data and EOS predictions for the oil/C ₁ system	49
Table 4–4: Properties of components in the four-PC EOS model calibrated against oil/C ₁ /C ₂ CCE and MMP data.....	50
Table 4–5: Optimized BIP of the four-PC EOS model calibrated against oil/C ₁ /C ₂ CCE and MMP data	50
Table 4–6: Comparison of the measured data and EOS predictions for the oil-C ₁ /C ₂ system	51
Table 4–7: Comparison of the measured and predicted MMPs for the oil/C ₁ and oil/C ₁ /C ₂ systems. The slimtube simulation and pseudoternary diagrams are used to calculate MMPs for four-PC and one-, two-PC EOS models, respectively.....	55
Table 5–1: Petrophysical properties of the plug	60
Table 5–2: Mineralogy of the Montney plug from the XRD analysis.....	61
Table 5–3: Initial conditions of the HnP tests. The temperature is kept at 50°C during the tests	64
Table 5–4: Results of the four HnP tests	70

Table 5–5: Oil production by different recovery mechanisms during natural-gas HnP experiments.....	80
Table 5–6: P_{sat} estimation by the calibrated PR-EOS and fractions of free/solution gas in the leaked-off gas at the end of the soaking period. The fraction of free gas is calculated by taking the ratio of mol% of gas at P_f and the mol% of leaked-off gas, for instance, it equals to $58.97/80.25 = 0.73$ in Set 1-C ₁ test.....	82
Table 6–1: Comparison of calculated diffusion coefficient calculated in this study with the literature.....	91
Table 6–2: Comparison of the D_{eff} calculated in this study with the literature.....	92
Table 6–3: N_{Pe} calculations for 1-D transport of natural gas into the oil-saturated plug. The values of porosity, permeability, oil viscosity, and core-plug length are the same for all HnP tests.....	96
Table 6–4: Comparison of the calculated N_{Pe} for diffusion-dominated transport in this work with the literature.....	97
Table 7–1: Petrophysical properties of the plugs from Marly (A and B) and Vuggy (C) units	102
Table 7–2: Mineralogy of plugs A and C obtained from XRD analysis	102
Table 7–3: Composition of the cross-linked gel fracturing fluid.....	107
Table 7–4: Physical properties of Midale crude oil, brine, and fracturing fluid.....	108
Table 7–5: List of experimental conditions of the core flooding tests to simulate leakoff and flowback processes. Except for the freshwater leakoff in Test 2, the remaining leakoff tests were conducted using the FF containing surfactants. One PV of freshwater/FF was injected during the leakoff process of all the tests.....	110
Table 7–6: Measured k_{abs} , k_{oeff} and S_{wirr} of the plugs before and after the aging process	116
Table 7–7: Brine/oil CA values measured on the surface of the plugs before leakoff and after flowback processes	118

Table 7-8: Equilibrium pressure drop and koeff values before leakoff (baseline) and after flowback processes after 3- and 14-day shut-in periods.....	124
Table 7-9: Changes in S_w during FF leakoff and flowback processes (Tests 3, 5 and 7)..	124
Table 7-10: Capillary-number calculations for the leakoff processes for Tests 3 to 8.....	127
Table A-1: Compositional analysis of Montney oil from the simulated distillation method	164
Table A-2: Measured density of oil at different pressures and temperatures	165
Table A-3: Optimized BIP values for the one-PC EOS model	168
Table A-4: Properties of the components in the one-PC EOS model	168
Table A-5: Experimental and predicted P_{sat} using the one-PC EOS model	169
Table A-6: Optimized BIP values for the two-PC EOS model	169
Table A-7: Properties of the components in the two-PC EOS model	169
Table A-8: Experimental and predicted P_{sat} using the two-PC EOS model	169
Table A-9: Two-phase equilibrium data using the four-PC EOS model with Compositions 1 through 4 for the oil/C ₁ systems and Compositions 5 through 8 for the oil/C ₁ /C ₂ systems	170
Table A-10: Two-phase equilibrium data using a two-PC EOS model with Compositions 9 through 12 for the oil/C ₁ systems and the one-PC EOS model with Compositions 13 through 16 for the oil/C ₁ /C ₂ systems	172
Table B-1: Pressure-Decline Data of Oil/C ₁ Test	174
Table B-2: Pressure-Decline Data of Oil/C ₁ /C ₂ Test	176
Table B-3: Pressure-Decline Data of Set 1-C ₁ Test	178
Table B-4: Pressure-Decline Data of Set 1-C ₁ /C ₂ Test	182
Table B-5: Pressure-Decline Data of Set 2-C ₁ Test	186
Table B-6: Pressure-Decline Data of Set 2-C ₁ /C ₂ Test.....	190
Table C-1: Composition of the Midale reservoir brine	196

Table C-2: Physical properties of the surfactants used in the study (provided by Element Technical Services Inc.)	196
--	-----

List of Figures

Figure 1–1: Schematic illustration of gas-transport and oil-recovery mechanisms during the gas HnP process.....	3
Figure 1–2: Schematic illustration of fluid flow and saturation change near the fracture face after hydraulic fracturing of tight-oil reservoirs.....	4
Figure 2–1: Unconventional resources triangle based on reservoir properties (Adapted from Ghori 2013; Ma and Holditch 2015).	8
Figure 2–2: Schematic representation of a hydraulically-fractured well drilled in an unconventional reservoir (adapted from Mydland et al. 2020).....	8
Figure 2–3: Plots of (i) oil and condensate RFs (Gherabati et al., 2017) and (ii) average oil production per well in the Eagle Ford shale (EIA, 2016).	10
Figure 2–4: Location map of the Montney and Midale tight-oil Formations (Canada Energy Regulator 2013).	12
Figure 2–5: Conceptual pore network model showing different phase behaviors in different pore sizes for a gas/oil system with a phase-behavior shift (Alharthy et al. 2013).	15
Figure 2–6: Adsorption of a microemulsion droplet to the oil/water interface of an oil-wet wall. The microemulsion droplet is shown in blue, the nonionic surfactant is shown as red arrows, and the solvent or self-assembled structures is in orange (Bui et al. 2020).	22
Figure 3–1: Simulated distillation results for the Montney oil sample: (a) compositional analysis, (b) true-boiling-point distribution.....	24
Figure 3–2: Experimental setup for conducting VIT tests: a) the visualization system, b) an image of the capillary tubes, and c) a custom-built gas mixer.....	26
Figure 3–3: Schematic of the PVT apparatus for conducting CCE tests.....	27
Figure 3–4: The results of VIT tests for estimating MMPs of three oil/C ₁ /C ₂ systems at 50°C, a) C ₁ /C ₂ – 70.3/29.7 mol%, b) C ₁ /C ₂ – 28.7/71.3 mol%, and c) C ₁ /C ₂ – 100/0 mol%.....	32
Figure 3–5: The results of CCE tests, P_{sat} and calculated SF at 50°C: (a), (b) for oil/C ₁ systems, and (c), (d) for oil/C ₁ /C ₂ systems.....	34
Figure 3–6: Comparison of the measured oil density at different pressures and temperatures with calculated density using Tait equation.....	35

Figure 3–7: Images of oil-gas interfaces at (i) initial conditions at P_{atm} , (ii) end of pressure buildup at P_{set} , and (iii) equilibrium at P_{eq} . The temperature is kept at 50°C during the experiment.....	37
Figure 3–8: Images captured at oil-gas interfaces during the pressure buildup process: (a) vaporizing flows in the oil/C ₁ test, and (b) vaporizing/condensing flows in the oil/C ₁ /C ₂ test at 50°C.....	40
Figure 4–1: Pseudoternary diagrams illustrate a) a vaporizing gas drive and b) a condensing gas drive. O, G, and M represent oil, C ₁ , C ₁ /C ₂ mixture, respectively.....	46
Figure 4–2: Comparison of experimental and predicted P_{sat} using phase envelopes at 50°C: a) two- and four-PC EOS models with C ₁ mol% of 70.1, and b) one- and four-PC EOS model with C ₁ /C ₂ mol% of 69.7/30.3.....	53
Figure 4–3: Equilibrium K -values versus MWs of the components in the four-PC EOS models for a) oil/C ₁ system and b) oil/C ₁ /C ₂ system at 137.90 bar and 50°C.....	54
Figure 4–4: Pseudoternary diagrams of the oil/C ₁ system at 50°C: a) injection pressure of 137.90 bar, and b) injection pressure of 307.51 bar.....	56
Figure 4–5: Pseudoternary diagrams of oil/C ₁ /C ₂ systems at 50°C: a) C ₁ /C ₂ :70.3/29.7 mol%, and b) C ₁ /C ₂ :28.7/71.3 mol%.	57
Figure 5–1: Pore-throat size distribution from the MICP data.....	62
Figure 5–2: SEM images of (a) clay components include illite (IL), and mixed-layers of illite-mica (mi) flakes, (b) dolomite cement (do) is widespread, while silica cement (si) is commonly mixed with illite. Illite mineral is observed as clay ribbons. Inter-crystalline pores (yellow arrows) are located between clays and cements.	62
Figure 5–3: Schematic illustration of fluid flow through the open face of the oil-saturated plug during the natural-gas HnP process.....	64
Figure 5–4: Experimental setup and procedure for conducting HnP tests at T_{set} . P and BPR stand for pressure and back-pressure regulator, respectively. The initial pore pressure (P_i) in Set 1 is atmospheric while it is ~134.45 bar in Set 2.....	65
Figure 5–5: Pressure-decline profiles during (a) ~168 hours soaking period of HnP tests, and (b) soaking period of oil/C ₁ and oil/C ₁ /C ₂ tests at T_{set}	70
Figure 5–6: Images of the plug surface during initial conditions (Step 1), gas injection (Step 2), soaking (Step 3), and depressurization (Step 4) of all tests at T_{set}	74
Figure 5–7: Normalized mole fractions of the vaporized oil components from the GC analysis.	76
Figure 5–8: Oil RFs from the HnP tests measured by the weight-balance method.	79

Figure 5–9: (a) pressure-decline profiles and the images of the surface in Set 1-C ₁ test, and (b) the evolved gas bubbles, merged (yellow arrows), and moved upwards (red arrows) and the produced oil being draining downward caused by gravity (blue arrow) observed on the surface during the depressurization phase of Set 2-C ₁ /C ₂ test.....	83
Figure 6–1: Pressure-decline regions classification by <i>k</i> -plane clustering method: (a) Oil/C ₁ , and (b) Oil/C ₁ /C ₂ (C ₁ /C ₂ :70/30 mol%).	91
Figure 6–2: Pressure-decline regions classification by <i>k</i> -plane clustering method: (a) Set 1-C ₁ , (b) Set 1-C ₁ /C ₂ , (c) Set 2-C ₁ , and (d) Set 2-C ₁ /C ₂	93
Figure 6–3: <i>N_{Pe}</i> profiles during soaking period: (a) Set 1-C ₁ , (b) Set 1-C ₁ /C ₂ , (c) Set 2-C ₁ , and (d) Set 2-C ₁ /C ₂	95
Figure 7–1: Depositional sequences and geological units of the Midale tight carbonate formation (Burrowes, 2001). T.F. represents Three Fingers transitional unit. Circled numbers 1 and 2 show major depositional sequences, while circled number 3 shows a low-permeability zone separating M1 and M3 layers. Layers V2 to V6 in the Lower Vuggy are identified for the purposes of reservoir modeling.....	100
Figure 7–2: Images of the plugs (a) A, (b) B, and (c) C.	101
Figure 7–3: Thin-section images taken at 125x magnification: (a), (b) for plug A with interparticle porosity (yellow arrows) partially occluded by residual hydrocarbon (green arrows), intraparticle porosity partially occluded by dolomite cements (white arrows), and calcite cements (orange arrows); (c), (d) for plug B with interparticle and intraparticle porosity that is partially occluded by dolomite cements, and pyrite nodules (red arrow); and (e), (f) for plug C with a micro-fracture (blue arrow) partially filled with calcite cement, interparticle and intraparticle porosity partially occluded by residual hydrocarbon and dolomite cements.....	104
Figure 7–4: Pore-throat-size distributions from MICP data of plugs (a) A, (b) B, and (c) C.106	
Figure 7–5: Schematic diagram of the core flooding apparatus. DP = differential pressure; N ₂ = Nitrogen.....	109
Figure 7–6: The procedure for the coreflooding tests: (a) simulating leakoff and flowback processes and (b) injection conditions in Steps 2 and 4.....	112
Figure 7–7: IFT values of (a) freshwater/oil and FF/oil systems measured at different mixing levels before the leakoff, and (b) aqueous/oleo systems measured after the flowback processes.	118
Figure 7–8: Pressure-drop profiles measured (a) during freshwater and FF leakoff, and (b) during flowback process of plug B (q = 0.09 cm ³ /min in both processes).	120

Figure 7–9: Pressure-drop profiles measured during (a) FF leakoff ($q = 0.09 \text{ cm}^3/\text{min}$ for plug A and B, and $q = 0.02 \text{ cm}^3/\text{min}$ for plug C), (b) flowback of plug A ($q = 0.025 \text{ cm}^3/\text{min}$), and (c) flowback of plug B ($q = 0.24 \text{ cm}^3/\text{min}$), and (d) flowback of plug C (constant pressures applied at two steps, i.e. 34 bar and 80 bar, for FF clean-up, then switched to $q = 0.007 \text{ cm}^3/\text{min}$ for koeff measurements after 2 injected PV).
.....122

Figure A-1: Two-phase equilibrium K -values vs. MW of PCs in (a) two-PC EOS model and
(b) one-PC EOS model at reservoir pressure and temperature of 137.89 bar and
50°C.....173

Nomenclature

Notations

∂P	= differential pressure in HnP tests, bar
$\partial p/\partial t$	= pressure drop, Pa/s
$\partial p/\partial x$	= pressure drop, Pa/m
δV	= change in oil volume caused by rock/oil compressibility, cm ³
ϕ	= porosity, % bulk volume
a	= tortuosity constant, dimensionless
C	= molar concentration, mol/m ³
c_f	= isothermal coefficient of compressibility of pore volume, 1/bar
C_{PEN}	= volume-shift parameter, cm ³ /mol
D	= diffusion coefficient, m ² /s
DP	= differential pressure in coreflooding tests, bar
F	= formation resistivity
J_x	= molar flux of component x per unit area
k	= permeability, mD [μ D], [nD], [m ²]
k_1	= constant for Eq. 6-2, 1/hour
L	= core-plug length, m
m	= cementation factor, dimensionless
MW	= molecular weight, g/mol
n	= adjustable fitting parameter, dimensionless
N_{cap}	= capillary number, dimensionless
N_{Pe}	= Péclet number, dimensionless
P	= pressure, bar [psig]
P_c	= critical pressure, bar
PV	= pore volume, cm ³

q	= flow rate, cm^3/min
R	= gas constant, J/K/mol
RF	= recovery factor, % of original oil volume in the plug
SF	= swelling factor, fraction
SG	= specific gravity, dimensionless
S_w	= water saturation, fraction
T	= temperature, $^\circ\text{C}$
t	= time, hours
T_b	= boiling-point temperature, $^\circ\text{C}$
T_c	= critical temperature, $^\circ\text{C}$
u	= Darcy velocity, m/s
V	= volume, $\text{cm}^3 [\text{m}^3]$
V_c	= critical volume, cm^3/gmol
Z	= gas compressibility factor, dimensionless
z_i	= mole fraction
z_o	= height of the oil column in the cell in bulk-phase tests, cm
σ	= interfacial tension, mN/m
τ	= tortuosity factor, dimensionless
ω	= acentric factor
θ	= contact angle, degree
μ	= viscosity, $\text{mPa}\cdot\text{s}$
ρ	= density, kg/cm^3
σ	= interfacial tension, mN/m
Superscript	
eff	= effective
Subscripts	

abs	= absolute
atm	= atmosphere
b	= brine
c	= critical
eq	= equilibrium
f	= final
g	= gas
gc	= critical gas
i	= initial
irr	= irreducible
o	= oil
ref	= reference
sat	= saturation
set	= setting conditions for natural gas HnP tests
w	= water

Acronyms

AARD	= average absolute relative deviation, dimensionless
BIP	= binary interaction parameter
BPR	= back-pressure regulator
CA	= contact angle
CCE	= constant composition expansion
EIA	= U.S. Energy Information Administration
EOR	= enhanced oil recovery
EOS	= equation of state
FF	= fracturing fluid
FW	= freshwater

GC	= gas chromatography
HC	= hydrocarbon
HnP	= huff ‘n’ puff
IFT	= interfacial tension
L	= liquid
MICP	= mercury-injection capillary pressure
MMP	= minimum miscibility pressure
NEB	= Canada National Energy Board
PC	= pseudocomponent
PR-EOS	= Peng-Robinson equation of state
PVT	= pressure volume temperature
RPI	= regained permeability index
SDT	= spinning drop tensiometer
SEM	= scanning electron microscope
SI	= shut-in
T.F.	= Three Fingers
V	= vapor
VEF	= volume expansion factor
VIT	= vanishing interfacial tension
XRD	= X-ray diffraction

Chapter 1 : Introduction

1.1.Research Motivation

The goals of this research are driven by the economic (oil recovery factor less than 10% of the initial oil in place) and environmental (methane flaring) implications in developing unconventional reservoirs. These challenges turn out to be an incentive for enhanced-oil-recovery (EOR) technology development. EOR methods targeting unconventional reservoirs differ from those in conventional reservoirs because of heterogeneity, poor quality of the formation and project economic. Consequently, they have been implemented not only during reservoir depletion (e.g., natural-gas HnP), but also during fracturing operation (e.g., flowback enhancers). Although, laboratory studies and pilot tests have shown some early success, controlling mechanisms for oil recovery are not well understood.

Natural-gas HnP is an emerging technology that promises to be a sustainable method to improve recovery of unconventional reservoirs. Several studies have been carried out to evaluate oil-recovery efficiency and mechanism, however, they tend to focus on a single mechanism and do not provide a systematic evaluation of possible mechanisms involved in the process. Furthermore, there are very limited laboratory works to quantitatively and qualitatively investigate the role of gas diffusion and dominant oil-recovery mechanisms involved in the natural-gas HnP process on ultratight rocks. Therefore, a systematic evaluation of gas-transport and recovery mechanisms is crucial to improve the efficiency of the HnP process. A better understanding of these mechanisms helps to develop procedures for field trials.

During hydraulic fracturing operation, a large amount of fracturing water is pumped through the wellbore into the formation, creating a fracture network for hydrocarbon production. This operation can be considered as a HnP process with fracturing water as an injectant. The capillary trapping of water phase near fracture-faces reduces the oil relative permeability and has been a challenging research topic over the last decade. Experimental studies on leakoff and flowback of FF containing flowback enhancers (i.e., surfactants) are well-documented in the literature, however, most of them were conducted using packed columns containing sand, carbonate, shale, or proppant particles, and thus the results did not fully capture the effects of mineralogy and the complex pore structure of tight rocks. Moreover, the extent of permeability impairment and controlling mechanisms of oil recovery during flowback under different reservoir conditions have not been thoroughly studied.

1.2.Hypothesis

The hypothesis is divided into two parts corresponding to (i) gas-transport and recovery mechanisms in a natural-gas HnP cycle under zero irreducible water saturation (S_{wirr}), and (ii) permeability impairment caused by FF fluids leakoff and remediation methods under $S_{wirr} > 0$.

Figure 1-1 shows the sequence of hypothesized events responsible for gas transport into and oil production from the matrix during a HnP cycle in a tight-oil reservoir. At initial conditions, fractures and matrix are at thermodynamic equilibrium and saturated with oil and solution and/or free gas depending on pressure and temperature. Usually, gas HnP is implemented after primary production, and thus, most of the leaked-off fracturing water is expected to be cleaned up. In the ‘huff’ phase, gas is injected into the well and is mainly transported through high-permeability fractures. A dynamic process of gas/oil mixing occurs near fracture/matrix interface, resulting in vaporizing oil

components to the gas phase and oil swelling. In the early soaking period, advection and diffusion remain the main gas-transport mechanisms. As the soaking period progresses, gas may penetrate deeper into the matrix and swell the oil by the diffusive transport. In the depressurization phase, gas expansion is expected to be the dominant recovery mechanism.

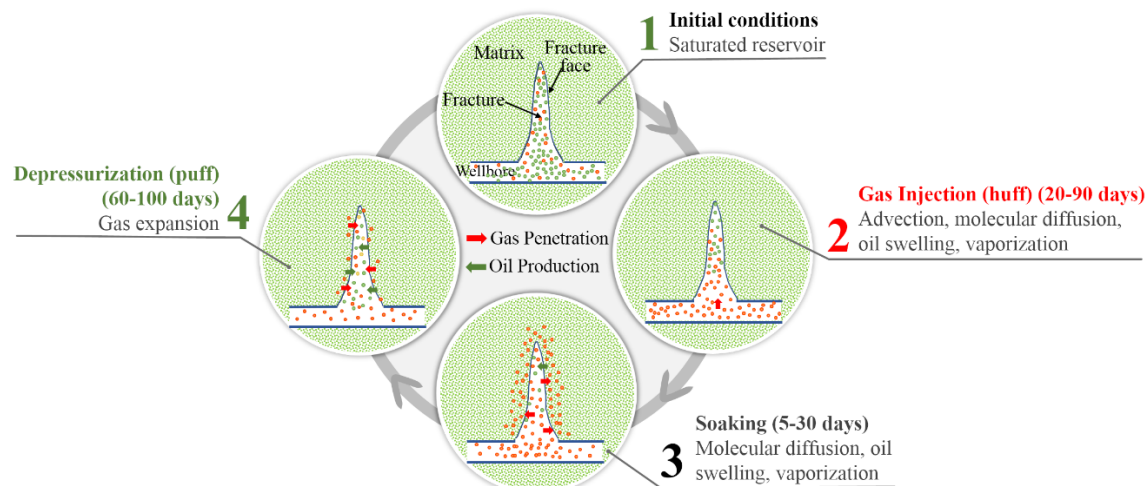


Figure 1–1: Schematic illustration of gas-transport and oil-recovery mechanisms during the gas HnP process.

After HF operation, fracturing water is trapped near the fracture/matrix interface because of capillary discontinuity, forming a high-water-saturation zone and decreasing the oil effective permeability (k_o^{eff}). Surfactants are expected to improve k_o^{eff} by interfacial-tension reduction, wettability alteration, leading to a decrease in water saturation (compared with the S_{wirr}) during flowback. Moreover, well shut-in may help dissipate trapped fracturing water deeper into the matrix during soaking time. Figure 1–2 presents a schematic illustration of the fluid flows during leakoff/flowback and water saturation near the fracture face.

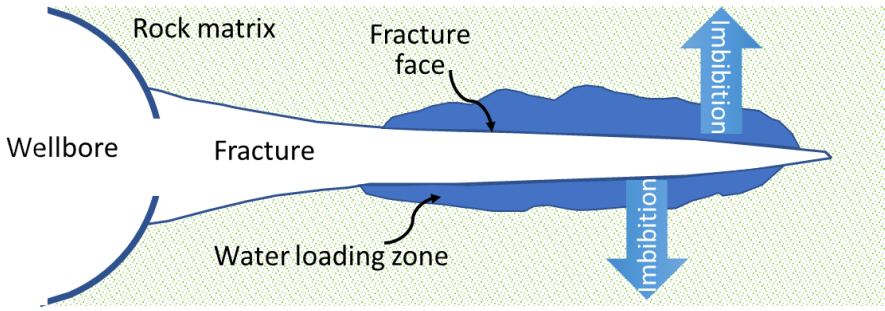


Figure 1–2: Schematic illustration of fluid flow and saturation change near the fracture face after hydraulic fracturing of tight-oil reservoirs.

1.3. Research Objectives

The primary research objective is to qualitatively and quantitatively evaluate gas-transport and recovery mechanisms during a natural-gas HnP cycle under zero S_{wirr} . The effects of water on the recovery mechanism are evaluated separately using leakoff and flowback experiments. The detailed objectives are as follows:

- Performing minimum-miscibility-pressure (MMP) measurements by vanishing interfacial tension technique, constant-composition-expansion test, and visualization test of gas/oil interactions at the interface to understand phase behaviour of the natural-gas/oil systems during a gas HnP process.
- Modeling phase behaviour of natural-gas/oil systems by calibrating Peng-Robinson (Robinson and Peng 1978) equation of states (EOS) against measured constant-composition-expansion and MMP data. The calibrated PR-EOS is used to predict the developed miscibility and thermodynamic conditions in the core-plug during natural-gas HnP experiments.
- Performing natural-gas HnP tests on an ultratight and oil-saturated plug to understand mechanisms controlling (i) gas transport into the plug during injection and soaking phases, and (ii) oil recovery during the whole process

- Quantifying gas-transport mechanisms during the soaking period through dimensionless Péclet number analysis. The model helps to mathematically explain the competition of advective and diffusive forces over the soaking time.
- Investigating k_o^{eff} impairment caused by the leakoff fluids (FF with surfactant and fresh water as a reference case) and remediation methods (surfactants and well shut-in).

1.4.Dissertation Outline

The dissertation is divided into eight chapters. Parts of Chapters 2, 3, 4, 5, 6, and 7 are published as peer-reviewed journal papers. Therefore, there might be some repetition of texts, figures, and tables in these chapters.

Chapter 1 presents the motivations, hypothesis, objectives of the research, and dissertation outline. Chapter 2 provides a general introduction, defines technical terms, and relevant literature reviews of the whole research.

Chapter 3 experimentally evaluates the phase behaviour of the natural-gas/oil systems through MMP measurements by vanishing interfacial tension technique, constant-composition-expansion, and visualization of gas/oil interactions at the interface tests. The phase-behaviour study serves as the basis for understanding thermodynamic conditions in the core-plug during natural-gas HnP tests.

Chapter 4 shows the procedure for PR-EOS calibration based on constant-composition-expansion and MMP data presented in Chapter 3. Thereafter, the calibrated EOS is applied to predict the MMP of different gas/oil systems.

Chapter 5 experimental evaluates gas-transport and recovery mechanisms in a natural-gas HnP cycle under core-plug conditions. The recovery mechanisms are visualized and quantified during gas-injection, soaking, and pressure-depletion phases.

Chapter 6 presents the estimation of diffusion coefficients in bulk-fluid and core-plug conditions using analytical models. The results are used in the modeling of Péclet number to quantify contributions of gas-transport mechanisms (advection vs. diffusion) during the shut-in period of the HnP tests.

Chapter 7 evaluates the extent of k_o^{eff} impairment caused by FF leakoff; and roles of surfactants, shut-in duration, and core-plugs properties on regained k_o^{eff} .

Chapter 8 lists the key conclusions of this work, its contributions to unconventional field practices, and recommendations for future work.

The nomenclature, appendices, and reference list from all chapters are combined and provided after Chapter 8.

Chapter 2 : Background of Enhanced Oil Recovery

Applications in Tight-Oil Formations

This chapter describes the background on unconventional resources, key oil-recovery technologies, field practices, fundamentals of phase behavior, aqueous phase trapping, gas-transport and recovery mechanisms in the gas HnP process.

2.1.Unconventional Resources

Unconventional resources can be grouped into three general categories: (1) unconventional reservoirs such as source rocks, tight sandstones, and carbonates; (2) unconventional fluids such as heavy oil, bitumen, and sour/acid gases; and (3) difficult hydrocarbons such as gas hydrates and oil shales (Leimkuhler and Leveille 2012). Most global unconventional resources development falls within the first and second categories. Figure 2-1 shows the classification of conventional and unconventional petroleum reservoirs. According to this classification, conventional reservoirs lie on top of the triangle having high permeability but moderate to low volume, while unconventional reservoirs have significantly high volume but poor permeability. In terms of pore-throat size, petroleum reservoirs are divided into three main categories: (i) greater than 2 μm in conventional reservoirs, (ii) 0.03 to 2 μm in tight reservoirs, and (iii) 0.005 to 0.1 μm in shales (Nelson 2009). Tight oil is defined as oil trapped in low-permeability shale, sandstone, and carbonate formations that accounted for 59% of total U.S. crude oil production in 2018 (EIA 2019). Recently, advances in multi-stage hydraulic fracturing and horizontal drilling technologies have led to a substantial increase in tight-oil production. Figure 2-2 illustrates a hydraulically-fractured horizontal well drilled in an unconventional reservoir. According to Ma and Holditch (2015) and Nelson (2009), the

rock matrix in tight reservoirs typically has permeability and porosity of less than 0.1 mD and 10%, respectively.

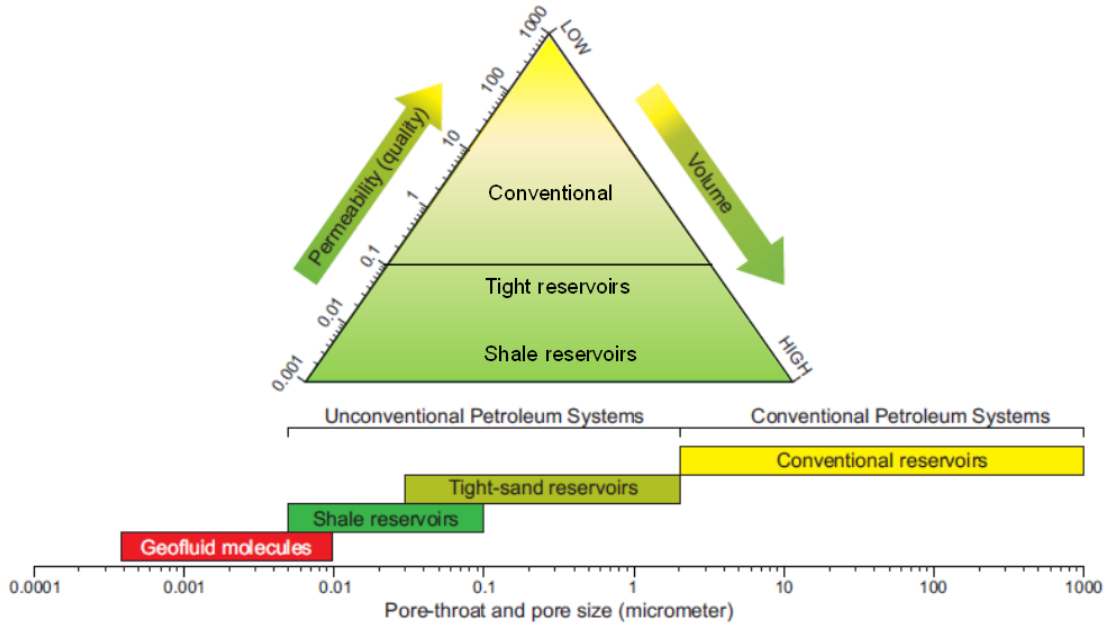


Figure 2–1: Unconventional resources triangle based on reservoir properties (Adapted from Ghori 2013; Ma and Holditch 2015).

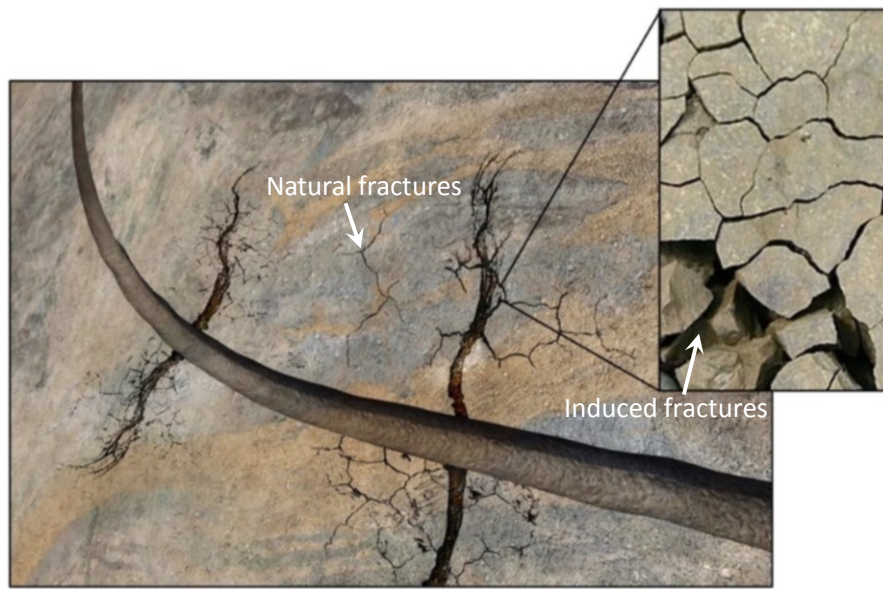
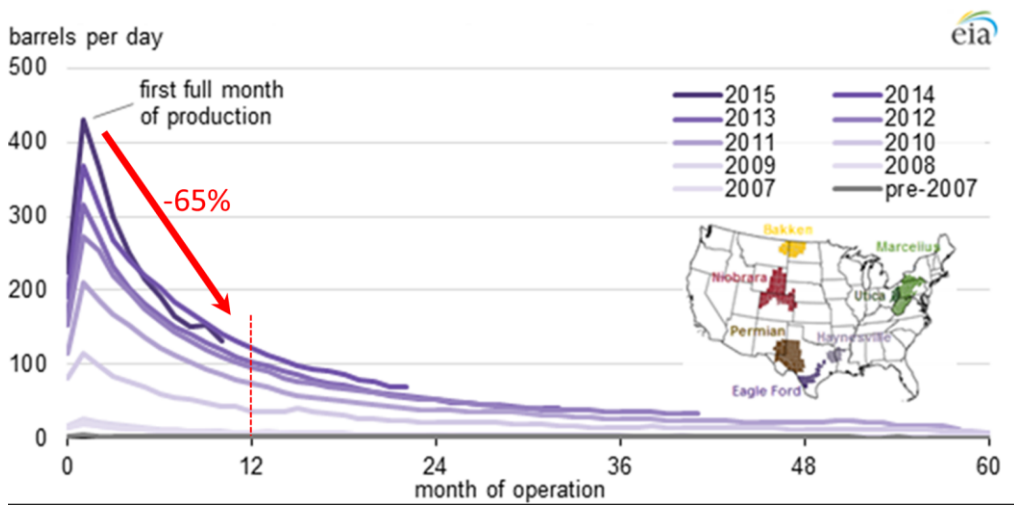
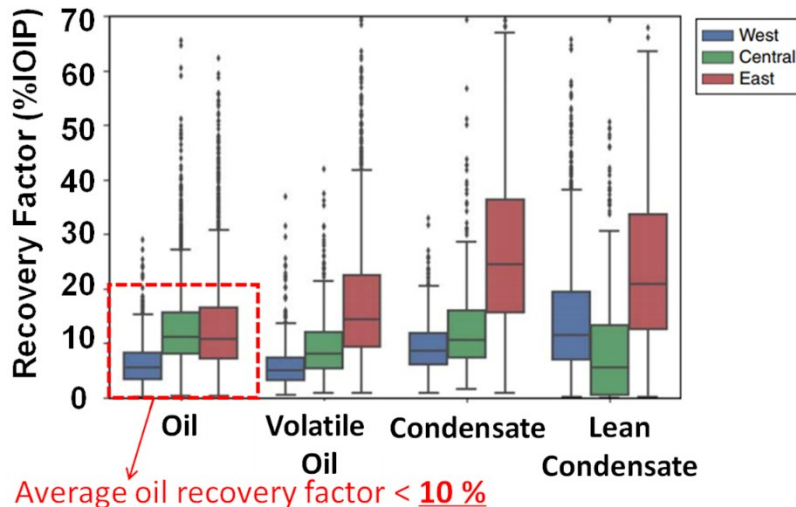


Figure 2–2: Schematic representation of a hydraulically-fractured well drilled in an unconventional reservoir (adapted from Mydland et al. 2020).

Low oil recovery factor after primary production and rapid decline rates are key challenges in developing tight-oil formations. Figure 2-3 shows production performance of oil wells completed in the Eagle Ford shale and statistical figures of oil and condensate recovery factors. Typical production performance of the well completed in Eagle Ford shale starts with high production rates, followed by a steep decline in production in the first year and transitions to a low production period (Figure 2-3a). This performance results in low efficiency of primary production (Figure 2-3b). In conventional reservoir development, the priority is to make a primary recovery successful, thereby downplaying the role of the EOR stage (also known as tertiary recovery). Recently, the industry has adopted a new approach by implementing EOR methods while fracturing unconventional reservoir development. According to Thakur (2019) and Alfarge et al. (2017), gas injection (CO_2 , N_2 , natural gas), low-salinity waterflooding, and chemical methods (surfactants, polymers, alkaline) are the most investigated EOR methods for applicability in the unconventional reservoirs. Except for low-salinity waterflooding, the cyclic gas-injection or HnP using natural gas and surfactant as a fracturing fluid (FF) additives have been tested in the field with promising results.



(a)



(b)

Figure 2–3: Plots of (i) oil and condensate RFs (Gherabati et al., 2017) and (ii) average oil production per well in the Eagle Ford shale (EIA, 2016).

The Western Canada Sedimentary Basin (Figure 2-4) which straddles over three provinces of British Columbia, Alberta, and Saskatchewan, holds substantial conventional and unconventional hydrocarbon resources. The unconventional portion remained undeveloped until the early 2000s when advances in horizontal drilling and multi-stage hydraulic fracturing made it possible to economically develop this enormous

resource. This research uses dead oil and tight-to-ultratight core samples (air permeability in the range of 60 nD to 5.28 mD) collected from Montney and Midale Formations to perform natural-gas HnP and leakoff and flowback experiments.

The Montney Formation has been well known as world-class unconventional petroleum resource with the oil-in-place of 141 billion barrels (Canada Energy Regulator 2013). The unconventional portion of this formation consists of mainly siltstone interbedded with thin shales, variable amounts of sandstone, and has a thickness ranging from 100 to 300m (Reynolds 2015). The gas permeability (by pulse-decay technique) of rock samples collected across the formation varies from 0.1 mD to 2×10^{-5} mD (Ghanizadeh et al. 2015). The Montney conventional sandstone and dolostone reservoirs have been the target of oil and gas exploration since the 1950s.

Further southeast of the basin, the Midale Formation is a part of massive Mississippian oil accumulation with an estimated oil-in-place of 515 MM bbl (McKishnie et al. 2005). Reservoir rock is carbonate deposited in a variety of depositional environments and with a wide range of porosity (2% to 37%) and permeability (<0.01 mD to 500 mD) (Burrowes 2001). One of the prominent features of this formation is a network of sub-vertical fractures, both open and cemented.



Figure 2–4: Location map of the Montney and Midale tight-oil Formations (Canada Energy Regulator 2013).

2.2.Natural-Gas HnP Process in Tight-Oil Formations

2.2.1. Overview of Gas-Injection EOR

The conventional gas-injection approach using well pairs (injector/producer) is not applicable in tight reservoirs because of the low permeability of rock matrix and preferential flow of gas through fractures, bypassing the matrix oil (Carpenter 2018; Thakur 2019). Instead, the gas HnP process has been found as an effective technique to improve oil recovery in such reservoirs (Cronin et al. 2019; Chen et al. 2014). A gas HnP process is applied in a single well and comprises of three distinct phases: (1) gas is injected into the well to a targeted gas volume or injection pressure (huff), (2) the well is shut-in for a period of time to allow gas penetrate deeper into the reservoir, and (3) the well is reopened for production (puff).

Several studies have been conducted to evaluate oil recovery from tight-rock samples (permeability in the range of μD) by gas HnP process using CO_2 (Yassin 2019; Yu et al.

2017; Habibi et al. 2017; Song and Yang 2017) and natural gas (Fu 2019; Lou et al. 2019; Hoffman and Reichhardt 2019; Li et al. 2020). There has been a growing interest in utilizing associated gases for gas-injection EOR and reducing gas flaring (Jin et al. 2017; Hoffman and Evans 2016). It is important to note that the intensity or heat-trapping capacity of methane (the principal component of natural gas) is 25 times higher than CO₂ (Dincer and Rosen 2013). Investment in EOR to boost production such as utilizing produced gas, uneconomic oil wells, and existing gas compression/gathering facilities is more economical than drilling new wells. Field tests of dry- and associated-gas EOR have been implemented with promising results in the Eagle Ford shale (Rassenfoss 2017; Ramirez and Aguilera 2016; Hoffman 2018; Orozco et al. 2020). The enrichment of injected gas, for example by adding C₂, improves the miscibility of the gas/oil system. Compared with C₁, C₂ has a higher solubility in oil, lower MMP (Metcalfe 1982), and is usually available at a less-expensive price than propane and butane (McGuire et al. 2017). However, field pilots using enriched natural gas in Bakken shale ended up with marginal improvements owing to issues related to reservoir containment and complex geology (Rassenfoss 2017; Kurtoglu 2013).

2.2.2. Developed Miscibility Conditions

In a gas HnP process, achieving miscibility conditions is vital to improve oil recovery. The miscibility conditions can be achieved by either first contact or by multiple contacts (Pedersen et al. 2015). The first-contact miscibility occurs when oil and gas immediately form a single phase at any mixing proportions and given pressure and temperature. Multi-contact miscibility requires multiple contacts and mass transfer between the oil and injected gas. If the porous medium is represented as a series of mixing cells, the multi-contact miscibility can be categorized into two processes namely, a vaporizing gas drive and a condensing gas drive (Orr 2007). In a vaporizing gas drive, miscibility is achieved

by the vaporization of intermediate oil components into the gas phase. In a condensing gas drive, miscibility is achieved by condensation of gas components into the oil phase.

Minimum miscibility pressure (MMP) of an oil-gas system can be determined by three methods: experimental, numerical modeling, and analytical techniques (Egwuenu et al. 2004). The experimental methods include slim-tube, rising-bubble, and vanishing interfacial tension (VIT) tests. MMP can be numerically modeled by multiple mixing cell method (Zick 1986; Ahmadi and Johns 2011). The analytical technique has been developed which is based on the key tie line identification to speed up the calculation of MMP during oil displacement by multi-component gas (Jessen et al. 1998; Wang and Orr 1997).

Slim-tube experiments are still an industry standard for MMP estimation because they can describe the complex phase behavior and rock-fluid interactions (Yellig and Metcalfe 1980). However, the experiments are slow, and the level of physical dispersion is significantly less than that under field conditions (Johns et al. 2002). Alternatively, VIT and rising-bubble tests have become popular because they are fast and cost-effective. In the VIT test, the gas/oil interfacial tension (IFT) is measured at reservoir temperature and increasing gas-injection pressures. The gas/oil IFTs and capillary heights measured by pendant-drop shape analysis (Rao 1997) and capillary-rise method (Hawthorne et al. 2016) in the VIT technique correspond to first-contact and multi-contact miscibility, respectively.

Jessen and Orr (2008) argued that experimental MMP methods, such as VIT and rising-bubble experiments, are suspect because they may not describe the complex phase behavior and displacement processes under reservoir conditions. Therefore, computational methods using tuned equation-of-state (EOS) for MMP prediction have been developed to mitigate the drawbacks of these experimental methods (Ahmadi and

Johns 2011). Ayirala and Rao (2011) demonstrated that the change of gas/oil ratio in the VIT technique has a negligible impact on the capillary heights and gas/oil IFTs measured at gas/oil equilibrium conditions. Therefore, they concluded that MMP values measured by the VIT technique are independent of the compositional path. Ashrafizadeh and Ghasrodashti (2011) used a mechanistic Parachor model to match measured MMPs of five gas/oil systems by the VIT technique. Their measured values are within 5% accuracy compared to the MMP values measured by slim-tube experiments. Based on experimental and modeling studies on Bakken and Permian oil samples, Adekunle and Hoffman (2014), Li and Luo (2017) and Liu et al. (2018) reported that CO₂ achieves miscibility with the Bakken oil at lower pressures compared with other hydrocarbon gases. Furthermore, live oil samples containing solution gas achieve a lower MMP compared with dead-oil samples (Adekunle and Hoffman 2014). Yassin et al. (2018) conducted a bulk-phase visualization study of CO₂-oil systems to understand the gas-oil interactions at the interface. They observed strong vaporizing and condensing flows of oil components and supercritical CO₂ at the gas-oil interface during the pressure buildup process.

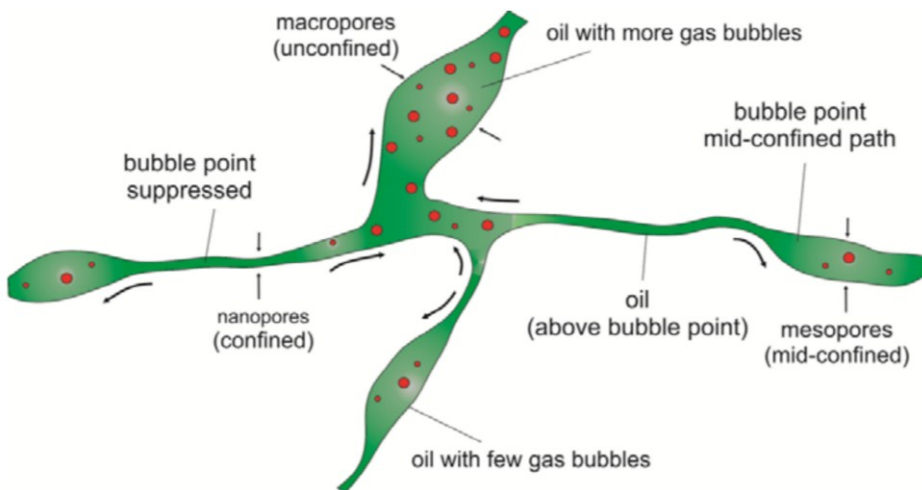


Figure 2–5: Conceptual pore network model showing different phase behaviors in different pore sizes for a gas/oil system with a phase-behavior shift (Alharthy et al. 2013).

Several studies have reported that the phase behavior of a gas/oil system in nanopores of unconventional reservoirs deviates from the conventional ones. Teklu et al. (2014) studied the effects of confined pores on the MMP of CO₂ and a mixture of CO₂ and C₁ with Bakken oil. They noted that the reduction in MMP caused by confinement becomes pronounced when the pore radius is less than 20 nm and is attributed to the critical-temperature and critical-pressure shifts as shown in Figure 2-5. Moreover, high capillary pressures affect equilibrium liquid/vapor-phase compositions, decreasing the MMP of CO₂ with Bakken oil (Nojabaei et al. 2013; Zhang et al. 2017).

2.2.3. Phase-Behavior Modelling

Cubic EOS are equations relating pressure-volume-temperature (PVT) to describe volumetric and phase behavior of pure components and mixtures (Whitson and Brûlé 2000). Phase equilibrium calculations using an EOS need to achieve minimum Gibbs free energy or satisfy chemical equilibrium. This means the chemical potential of each component in the liquid phase equals the chemical potential of each component in the vapor phase in a vapor/liquid system. The Peng-Robinson (Robinson and Peng 1978) equation of state (PR-EOS) is one of the most widely used cubic EOSs in the petroleum industry.

$$p = \frac{RT}{v - b} - \frac{a}{v(v + b) + b(v - b)} \quad (2-1)$$

$$a = 0.45724 \frac{R^2 T_c^2}{p_c} \alpha \quad (2-2)$$

$$\alpha = [1 + m(1 - \sqrt{T_r})]^2 \quad (2-3)$$

$$m = \begin{cases} 0.37464 + 1.54226\omega - 0.26992\omega^2 & \text{for } \omega < 0.49 \\ 0.37960 + 1.4856\omega - 0.1644\omega^2 + 0.01667\omega^3 & \text{for } \omega \geq 0.49 \end{cases} \quad (2-4)$$

$$b = 0.07780 \frac{RT_c}{p_c} \quad (2-5)$$

Predictions of thermodynamic conditions in the gas-injection EOR require accurate characterization of reservoir fluids using an EOS. The common method for tuning the EOS to fit experimental PVT data is to modify the properties of plus fractions [critical temperature (T_c), critical pressure (P_c), and acentric factor (ω)] and binary-interaction-parameter's k_{ij} between injection-gas component and plus fractions (Whitson and Brûlé 2000). Several correlations have been introduced to characterize critical properties (T_c and P_c) and ω . In this study, we use a set of correlations by Lee and Kesler (1975) to estimate the critical properties and ω of the pseudocomponents (PCs).

2.2.4. Gas-Transport Mechanisms during Natural-Gas HnP

2.2.4.1. Gas-Transport by Molecular Diffusion

Molecular diffusion is the transport caused by the random motion of molecules and atoms down a concentration gradient. Fick's 1st law (Fick 1855) stated that the mass flux J_x diffusing through a unit area of cross-section is proportional to the concentration gradient.

$$J_x = -D \frac{\partial C}{\partial x} \quad (2-6)$$

where D and $\frac{\partial C}{\partial x}$ are bulk-phase diffusion coefficient and derivative of the concentration over distance x .

Apply the mass conservation for the incremental volume over the duration dt yields Fick's 2nd law

$$\frac{\partial C}{\partial t} = D \frac{\partial^2 C}{\partial x^2} \quad (2-7)$$

The diffusion process in porous media is significantly hindered by the tortuous nature of the pores, cross-sectional area available for diffusion, and possibly by the pore sizes (Grathwohl 2012). This important gas-transport mechanism will be discussed and applied to quantify effective diffusion coefficients in the natural-gas HnP experiments in Chapter 6.

2.2.4.2. The Dimensionless Péclet Number

There is still debate whether the mass-transport of gas during the soaking period in a HnP process is dominated by advection or diffusion. Peclét number (N_{Pe}) is a ratio of convective to diffusive flows. According to Hobbs and Ord (2015) the N_{Pe} for fluid flows that transport mass in the porous medium is

$$N_{Pe} = \frac{u \times L}{D_{eff}} \quad (2-9)$$

where, u , L , and D_{eff} are Darcy velocity, length of the core plug, and effective diffusion coefficient, respectively.

When $N_{Pe} < 1$ the mass transport is dominated by diffusion (Perkins and Johnston 1963; Hobbs and Ord 2015). Cronin et al. (2019) and Carlsen et al. (2019) suggested that the key mechanisms behind multiple-contact miscibility development in conventional gas-injection processes (e.g. vaporizing and/or condensing drive) are based on the advection-dominated transport within the matrix. Also, they presumed that transport of gas into the matrix during the soaking period of the HnP process in tight reservoirs may be a completely diffusion-dominated ($N_{Pe} \approx 0$) process, and thus, only first-contact miscibility is relevant. Other researchers conducted simulation studies on recovery mechanisms in shale and tight reservoirs and reported that the diffusion mechanism dominates transport of gas into the Barnett shale matrix with permeability values of less than 10 nD (Olorede

2017), and into the Bakken rock matrix with permeability in the range of 1 to 100 μD (Lashgari et al. 2019; Yu et al. 2015).

2.2.5. Oil-Recovery Mechanisms during Natural-Gas HnP

Understanding oil-recovery mechanisms is crucial to optimize gas HnP processes implemented after the primary production of tight reservoirs. The recovery mechanisms involved in a gas HnP process include gas expansion, oil-viscosity reduction, oil swelling, and vaporization of oil components to the gas phase (Carlsen et al. 2019; Alharthy et al. 2018; Zick 1986) and pore-volume compressibility (Davudov and Moghanloo 2018). Hoffman and Rutledge (2019) studied oil-recovery mechanisms in tight rocks using analytical models. The authors reported that oil swelling is the most important mechanism, while oil-viscosity reduction is the least impact mechanism for low gas-oil-ratio reservoirs (500 to 2000 scf/stb). The transport of gas into the rock matrix is essentially controlled by gradients in pressure and chemical potential. Moreover, there may be enough time for gas diffusion if the injection phase takes 20 to 90 days as typically occurred in HnP field pilots (Jacobs 2019; Carlsen et al. 2019).

2.3. Aqueous Phasing Trapping after Hydraulic Fracturing and Remediation Methods

2.3.1. Overview of Fracturing Fluids

The FFs include aqueous (water-based) and non-aqueous (oil-based, energized, and foam). The choice of an appropriate type of FF depends on individual reservoir properties and the design of proppant placement.

The water-based FF is the simplest and cost-effective solution being used in North America. The commonly used water-based FFs are slickwater and crosslinked/linear gels (Ma and Holditch 2015). A slickwater system typically includes additives for reducing friction, preventing corrosion of completion components during the flowback process,

preventing clay swelling (King 2010; Ma and Holditch 2015), and estimating proppant distribution/transport (Salman et al. 2014; Senters et al. 2015; Zhao et al. 2019). Acid has been widely used as an additive in FF for carbonate formations (King 2014). Hydrochloric acid is typically used at 10 to 15 wt% to dissolve filled or cemented calcites (King 2014; Johnson et al. 2016; Lai et al. 2018). When using acid fracturing, corrosion control is needed to ensure long-term wellbore integrity. A crosslinked/linear gel system consists of gelling agents to increase the fluid viscosity and facilitate proppant placement, and oxidative breakers to destroy high molecular-weight polymers and facilitate the fluid flowback (Montgomery 2013; Al-Ali et al. 2016; Li et al. 2019).

2.3.2. Aqueous Phase Trapping

A large amount of FF is typically pumped through the wellbore into the formation to create a network of fractures during HF operation. However, only 5% to 50% of the FF is recovered during flowback and production phases (King 2012; Bertoncello et al. 2014; Ghanbari and Dehghanpour 2016; Liu et al. 2019).

Although HF operations have been used to unlock tight reservoirs, there is a potential for well-productivity impairment resulting from the loss of aqueous component in the FF into the rock matrix (Holditch 1979; Sharma and Agrawal 2013). The water might be trapped near the fracture/matrix interface because of capillary discontinuity, forming a high-water-saturation zone and decreasing the oil relative permeability (Bennion et al. 2006; Shaoul et al. 2011; Longoria et al. 2017; Sheng 2017). Al-Muntasher et al. (2017) and Palisch et al. (2007) reported formation damage during the flowback process by gel residue distributed along the fracture, reducing porosity and conductivity of the proppant pack, and fracture-width/length loss caused by filter-cake formation when a breaker is poorly designed for a gelled system.

2.3.3. Methods to Improve Regained Permeability

Several methods have been studied to mitigate the aqueous phase trapping and enhance the regained permeability after hydraulic fracturing. Among them, a combination of chemical treatment and well shut-in has been shown to be an effective method through experimental studies and field trials.

Experimental studies on leakoff and flowback of FF containing flowback enhancers are well-documented in the literature (Parmar et al. 2014; Yue et al. 2016; Himes et al. 2017; Nelson et al. 2018; Rabie et al. 2019; de Rezende et al. 2019). Most of them were conducted using packed columns containing sand, carbonate, shale, or proppant particles. In field applications, a combination of surfactants and well shut-in have been reported to improve gas production in Marcellus (Yaich et al., 2015) and oil production in Eagle Ford shales (He et al. 2014; He and Xu 2015).

To chemically reduce water saturation near the fracture/matrix interface, flowback enhancers (i.e., surfactants) can be added to the FF to reduce the IFT between the leaked-off FF and oil reducing capillary pressure and phase trapping (Bennion et al. 2000; Liang et al. 2015; Negin et al. 2017). Moreover, surfactants may alter the rock wettability from oil-wet to intermediate-wet, hence improving the imbibition of FF. Several studies have been conducted to evaluate the effects of surfactant type (i.e., cationic, anionic, nonionic, and amphoteric) and concentration on IFT of FF/oil mixtures (Hirasaki et al. 2011; Chen and Mohanty 2013; Mirchi et al. 2015; Mirzaei et al. 2016; Yarveicy et al. 2018). Nonionic surfactants have been shown to outperform ionic surfactants in field applications because they are compatible with other FF additives and are not sensitive to the salinity of brine and charged species (He and Xu 2017). According to Bui et al. (2020), the microemulsion droplet in aqueous phase undergoes the process of droplet movement towards the aqueous-phase/oil interface, droplet adsorption, and the droplet

breakup (Figure 2-6). After breakup, the surfactant molecules (shown in red arrows) stay at the aqueous-phase/oil interface, leading to a decrease in IFT. The solvent molecules or self-assembled structures (shown in orange) penetrate deeper into the oil film, altering the wettability of pore walls.

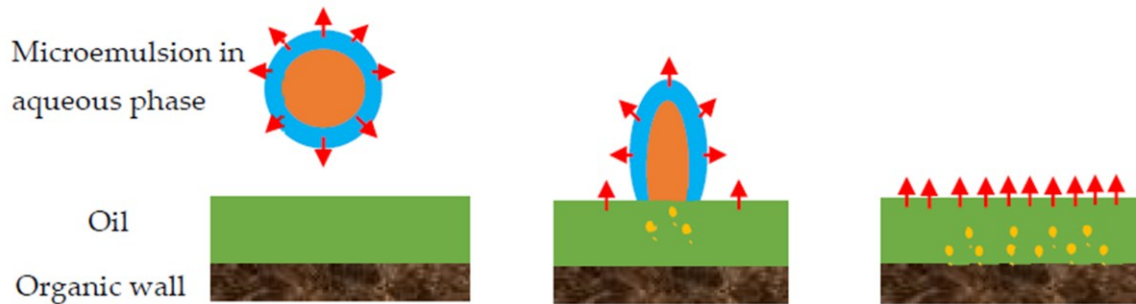


Figure 2–6: Adsorption of a microemulsion droplet to the oil/water interface of an oil-wet wall. The microemulsion droplet is shown in blue, the nonionic surfactant is shown as red arrows, and the solvent or self-assembled structures is in orange (Bui et al. 2020).

Shutting in a well after hydraulic fracturing operations can also improve well productivity by the imbibition of FF deeper into the reservoir (Bennion et al. 1999; Bertoncello et al. 2014; Dutta et al. 2014; Asl et al. 2019; Wijaya and Sheng 2020). In HF operations using crosslinked fluid systems, the shut-in time allows the breaker system to more efficiently break down the polymer network. However, there are uncertainties regarding the positive effect of shut-in periods if clay swelling occurs (Civan 2007; Jacobs 2015) and the conductivity of the proppant pack is reduced by crosslinked gel containing no breakers (Hawkins 1988). In addition, economic considerations should be noted for shutting in a well before placing it on production.

Chapter 3 : Experimental Study on The Phase Behavior of Natural-Gas/Oil Systems

3.1.Introduction

This chapter experimentally evaluates phase behavior of natural-gas/oil systems under reservoir conditions to complement natural-gas HnP experiments presented in a later chapter. We perform constant-composition-expansion (CCE) tests and MMP measurements by VIT technique to study phase behavior of the oil/gas systems. The natural-gas samples are methane (C_1) and mixtures of methane and ethane ($C_1/C_2:70/30$ mol%). Next, we conduct visualization tests (under $P = 137.9$ bar and $T = 50^\circ\text{C}$) to study gas solubility in the oil, oil swelling, and vaporizing/condensing phenomena at the oil/gas interface.

3.2.Materials

We used a dead-oil sample from a well drilled in the Montney Formation in northwestern Alberta, Canada, and conducted the experiments at representative reservoir pressure (P_{set}) and temperature (T_{set}) of 137.90 bar and 50°C, respectively. The C_1 and C_2 samples used in this study have a purity of 99.999%. The fluid properties and oil compositional analysis are presented in Table 3-1 and Figure 3-1, respectively. Detailed information on the compositional analysis of Montney oil from the simulated distillation method can be found in Appendix A.

Table 3–1: Physical properties of the Montney dead oil, and C₁/C₂ (NIST chemistry webbook) at T_{set}

Fluids	Density (kg/m ³)	Viscosity (mPa·s)	Surface Tension
Oil	818.50	2.82	23.95
C ₁	0.59	0.01	-
C ₂	1.13	0.01	-

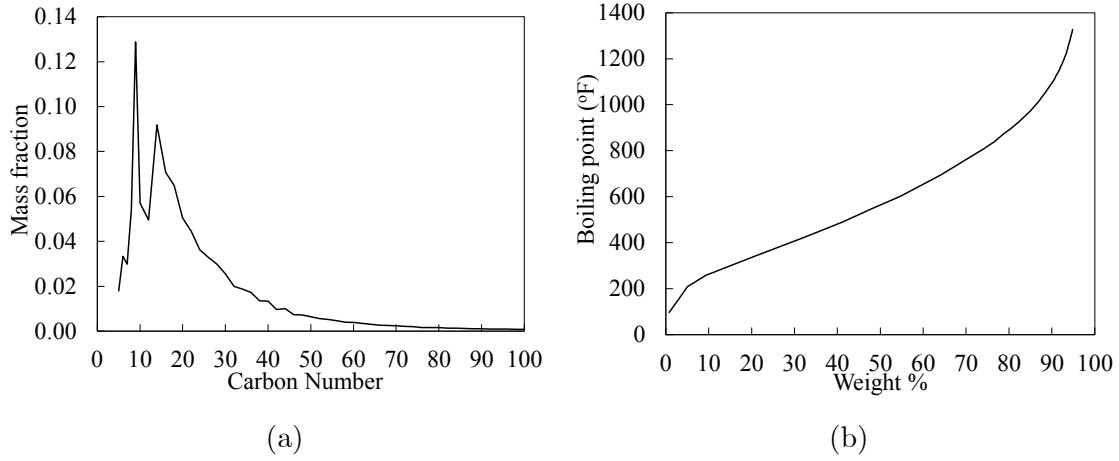


Figure 3–1: Simulated distillation results for the Montney oil sample: (a) compositional analysis, (b) true-boiling-point distribution.

3.3. Method

3.3.1. MMP Measurement

The VIT test consists of measuring IFT between the oil and injected gas at increasing pressures and a given temperature (Hawthorne et al. 2016). Figure 3-2 shows a schematic of the visualization system and an image of the capillary tubes and a custom-built gas mixer used for conducting the VIT tests. The main component of the visualization system is a see-through high-pressure and high-temperature cell. It has a chamber with an internal volume of 587 cm³ which is equipped with two sapphire sight glasses with

diameters of 2.4 cm and 4.8 cm. The pressure and temperature ratings of the visual cell are 275.79 bar and 200°C, respectively. Two sets of accumulators (500 cm³ each with an operating pressure of 689.48 bar) with heating jackets are used to deliver oil and gas into the cell using a continuous pulse-free pump. The pump can deliver a flow rate ranging from 0.0001–29 cm³/min and can supply a maximum pressure of 827.37 bar. Thermocouple, heating jackets, and temperature controllers are used to control the temperature of the visual cell and the two accumulators with an accuracy of $\pm 0.1^\circ\text{C}$. A pressure gauge with an accuracy of ± 0.14 bar is installed at the top of the visual cell for pressure monitoring. Halogen light sources are used to illuminate the two sight glasses and a digital camera equipped with a macro lens (EF USM 100mm f/2.8) is used for continuous capturing of images during the visualization experiments.

The procedure starts with placing three capillary tubes (inner diameters of 0.5, 0.85, and 1.05 mm as shown in Figure 3-2b) in the cell, and injecting gas into the cell at predefined pressure (P) steps. We check the system's leakage by purging the cell/lines several times with the tested gas. The temperature (T) of the cell and accumulators (with oil and gas) are set at T_{set} . The heated oil is injected into the cell until the oil level stops rising inside the capillary tubes. After waiting for approximately 3 minutes for the fluids to equilibrate, we capture images and measure the height of the oil/gas meniscus in each capillary tube from the top of the bulk-oil phase outside the tube. Finally, we plot the height values for the three capillary tubes vs. P and determine P corresponding to zero capillary heights by linear extrapolation. We interpreted this P as the MMP of the three oil/C₁/C₂ systems (with C₁ of 100, 70.1, and 28.7 mol%). We used three capillary tubes to have sufficient data points for extrapolating the trend lines to zero capillary heights.

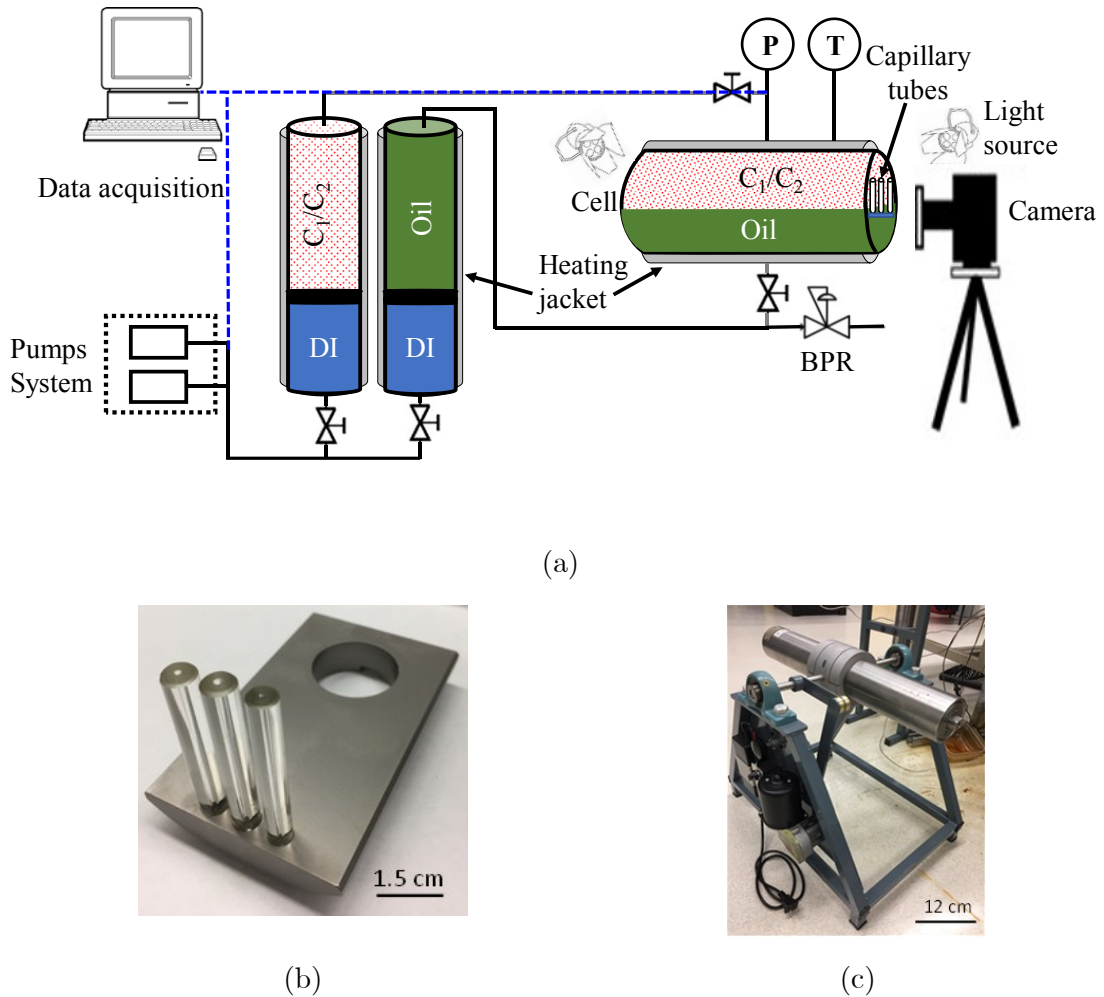


Figure 3–2: Experimental setup for conducting VIT tests: a) the visualization system, b) an image of the capillary tubes, and c) a custom-built gas mixer.

Mixtures of C₁/C₂ are prepared using two accumulators (500 cm³ each) and a custom-built gas mixer (Figure 3-2c). First, specified amounts of C₁ and C₂ are transferred to two accumulators at room temperature ($T = 21^\circ\text{C}$). The mole fractions of C₁ and C₂ (all in the gas state) are calculated according to the accumulator volume (500 cm³), calculated P , and corresponding compressibility factors to achieve the desired mole ratio (C₁/C₂ ratio of 70:30) at 21°C. The C₁ and C₂ properties are obtained using the NIST chemical webbook (NIST 2018). Second, C₁ and C₂ in the two accumulators are squeezed into the

gas mixer that rotates at a speed of 6 rev/min and with an angle of 150° to mix C₁/C₂ mixtures at 21°C for 24 hours. Finally, the gas mixtures are then transferred to a heated accumulator (50°C) and left to equilibrate for 6 hours before starting the VIT tests.

3.3.2. CCE Tests

The CCE tests are performed at reservoir conditions using a pressure-volume-temperature (PVT) cell to measure saturation pressure (P_{sat}) and saturated oil density (ρ_{sat}) and to calculate the swelling factor (SF). Figure 3-3 shows a schematic of the PVT apparatus. The P and T ratings of the PVT cell are 1034.21 bar and 199°C, respectively. The temperature of the PVT cell is controlled by an air bath with an accuracy of 0.1°C. A high-pressure pump controls the pressure of the PVT cell by hydraulic oil. A floating piston is inside the cell and isolates the test fluids from hydraulic oil. The total internal volume of the cell is 112 cm³, with a dead volume of 1.754 cm³. A pressure gauge is used to monitor the cell pressure with an accuracy of 0.72 bar. A cathetometer is in front of the PVT cell to measure the piston height (with an accuracy of 0.016 cm³) for calculating the volume of fluids in the cell.

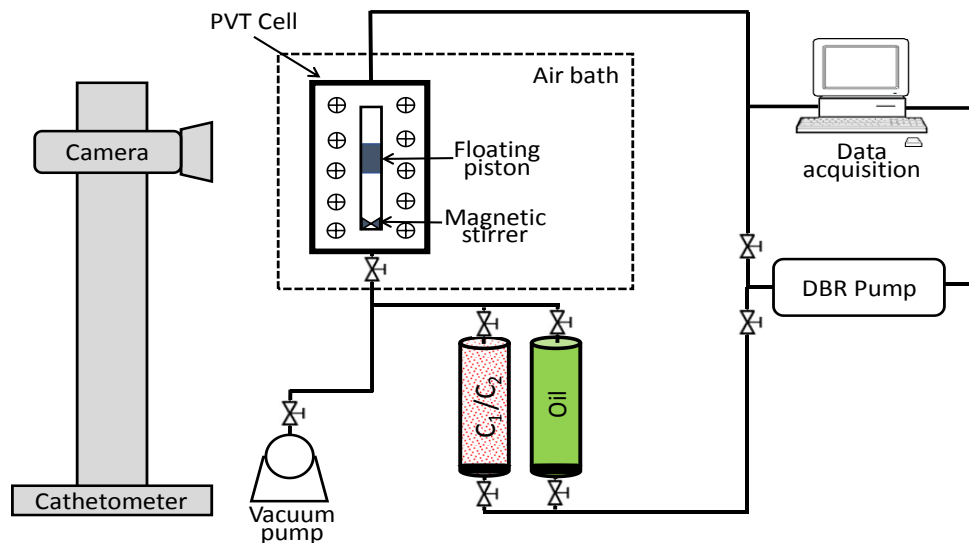


Figure 3-3: Schematic of the PVT apparatus for conducting CCE tests.

Table 3-2 lists the parameters of the CCE tests. For conducting the CCE tests, we specify amounts of injected gas and oil into the PVT cell at room temperature. The oven temperature is set at reservoir temperature and the stirrer is turned on to mix gas and oil for 24 hours. When the temperature reaches the set-point (50°C), we increase PVT-cell pressure until a single-phase is formed. The PVT-cell pressure is reduced stepwise and the mixture volume is recorded accordingly. The saturation point is determined as the pressure at which the slope of the pressure-volume changes. The saturation density is defined as the ratio of fluid mass in the cell to the mixture volume at saturation pressure.

Table 3-2: Experimental conditions of the CCE tests using the PVT cell. The temperature is kept at 50°C in all tests

Feed	Oil/gas (mol%)	Gas (mol%)	Mass of oil and gas (g)		
			Oil	C ₁	C ₂
1	89.7/10.3	C ₁	27.8	0.2	-
2	70.5/29.5	C ₁	14.45	0.38	-
3	50.6/49.4	C ₁	16.86	1.05	-
4	29.9/70.1	C ₁	10.15	1.50	-
5	30.2/69.8	C ₂	9.73	-	2.67
6	28.8/71.2	C ₁ /C ₂ – 30.0/70.0	21.7	1.02	4.47
7	29.0/71.0	C ₁ /C ₂ – 49.6/50.4	31.8	2.46	4.66
8	28.0/72.0	C ₁ /C ₂ – 69.7/30.3	35.6	4.06	3.30

We also measure oil density at different P (6.89 to 275.79 bar) and T (30, 50, and 70°C) values using the PVT cell based on mass balance. Because the mass of the oil in

the PVT cell is conserved, the oil density at different experimental conditions can be calculated by

$$\rho_1 = \frac{\rho_{\text{ref}} V_{\text{ref}}}{V_1} \quad (3-1)$$

where ρ_1 and V_1 are density and volume, respectively, of the oil at given P and T ; ρ_{ref} and V_{ref} are the density and volume, respectively, of the oil at atmospheric pressure (P_{atm}) and the given T . We measure ρ_{ref} and V_{ref} using a densitometer and the PVT cell at P_{atm} and different T values (30, 50, and 70°C). The accuracy of the densitometer is 60.01 kg/m³.

SF is defined as the total volume of oil and dissolved gas at P_{sat} and T divided by the volume of the dead oil (without gas) at the same T and P_{atm} ,

$$SF = \frac{(V_m)_{P_{\text{sat}}, T}}{(V_o)_{P_{\text{atm}}, T}} \times \frac{1}{1 - x} \quad (3-2)$$

where V_m is the molar volume of the mixture at P_{sat} and T_{set} , V_o is the molar volume of the oil at P_{atm} and T_{set} , and x is the mole fraction of the gas in the mixture.

3.3.3. Visualization Tests

Two visualization tests are conducted for oil/C₁ and oil/C₁/C₂ systems at P_{set} and T_{set} using a visualization cell as shown in Figure 3-2a. Before the tests, the cell and connecting lines are cleaned and vacuumed and then checked for leakage by pressurizing the cell with tested gas at 20.68 bar and monitoring the cell pressure for 4 hours. We conduct two tests (Test 1 for oil/C₁ and Test 2 for oil/C₁/C₂ with 30 mol% of C₂) in the following three steps:

- Initial conditions: Approximately 255 cm³ of oil is introduced into the cell through the bottom valve at P_{atm} and T_{set} .
- Pressure buildup: The tested gas is injected into the cell from an inlet valve at the top of the cell to reach P_{set} . Images of the oil/gas interface are captured to observe oil/gas interactions during gas injection. The gas-injection valve is closed at P_{set} to start a soaking period.
- Pressure decline: During the soaking period, the pressure in the cell will decline as a result of gas dissolution into the oil. The soaking period completes when the pressure in the cell reaches the equilibrium pressure (P_{eq}).

The volume of oil in the cell at initial conditions, end of pressure buildup, and pressure-decline periods are determined by using a spreadsheet-based image-analysis technique. It should be noted that the cell is not equipped with a magnetic stirrer and a floating piston to mix oil and injected gas and to reduce the time to reach equilibrium conditions. Therefore, the equilibrium state is achieved by slow interactions between oil and injected gas. Therefore, the term “oil-swelling factor” does not apply to this experimental condition. Instead, we define the volume-expansion factor (VEF) of the oil caused by dissolution of the injected gas:

$$VEF = \frac{(V_o)_{P,T_{\text{set}}}}{(V_i)_{P_{\text{atm}},T_{\text{set}}}} \quad (3-3)$$

where V_o is the oil volume at an elevated pressure P and T_{set} divided by the initial oil volume (V_i) at P_{atm} and T_{set} . The VEFs at the end of the pressure-buildup and soaking periods are referred to as initial VEF (VEF_{ini}) and equilibrium VEF (VEF_{eq}), respectively.

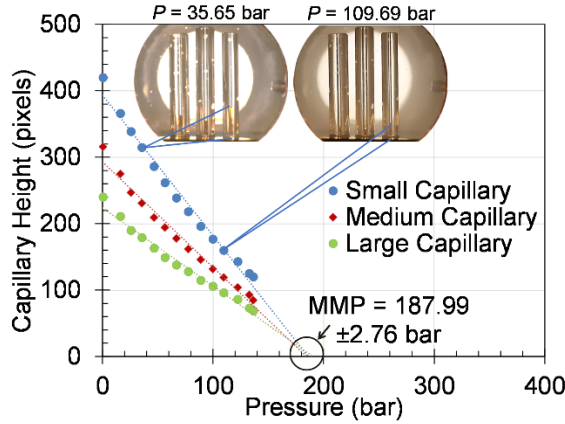
3.4. Results and Discussions

This section reports the results of the MMP measurements, CCE, and bulk-phase visualization tests.

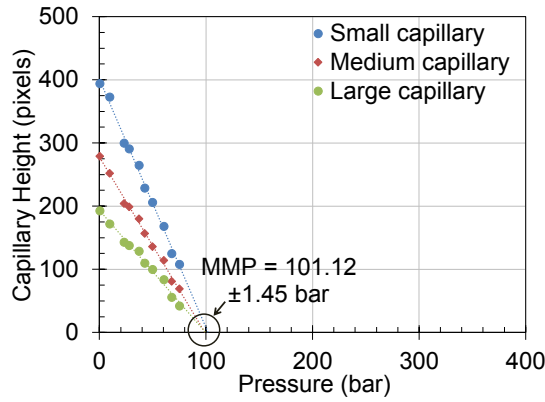
3.4.1. Measured MMPs of Natural-Gas/Oil Systems

We conduct the VIT tests to measure the level of capillary rise at increasing gas pressures and T_{set} . Consequently, the MMP is determined from the measured capillary heights. Figure 3-4 shows the measured capillary heights for capillary tubes with small, medium, and large diameters for three oil/C₁/C₂ systems. The measured MMPs of the three systems with C₁ of 100, 70.3, and 28.7 mol% are 299.92, 187.95, and 100.11 bar, respectively. Figure 3-4a includes two images captured at 35.65 and 109.70 bar that show the reduction of capillary heights with increasing gas pressures. The plot of each capillary tube contains 10 to 16 data points that are adequate to generate reliable trend lines and extrapolate it to the pressures corresponding to zero capillary heights.

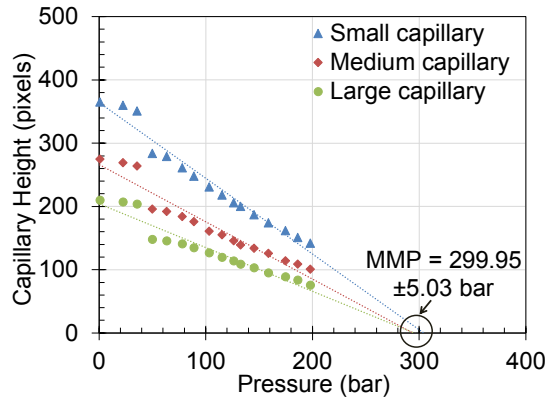
According to Figures 3-4b and 3-4c, MMP of the oil/gas mixtures decrease from 299.92 to 100.11 bar by increasing C₂ from 0 to 71.3 mol%. Metcalfe (1982) reported that the higher concentration of C₁ and C₂ in the rich gas increases and decreases MMPs of oil/gas systems, respectively. In this study, the capillary heights are measured at nearly equilibrium gas/oil conditions at each pressure step. The resulting MMPs satisfy the multicontact-miscibility requirements as reported by Ayirala and Rao (2011) and Hawthorne et al. (2016). Moreover, these measured MMPs will be validated by predicted MMPs using two-phase equilibrium data from the tuned EOS and ternary diagrams in the later sections.



(a)



(b)



(c)

Figure 3–4: The results of VIT tests for estimating MMPs of three oil/C₁/C₂ systems at 50°C, a) C₁/C₂ – 70.3/29.7 mol%, b) C₁/C₂ – 28.7/71.3 mol%, and c) C₁/C₂ – 100/0 mol%.

3.4.2. Results of CCE Tests

3.4.2.1. Oil/C₁ CCE Test

Here, we report the results of CCE tests on four oil/C₁ mixtures at T_{set} (see Table 3-2 for detailed feed compositions). P/V data from the CCE tests on the oil/C₁ systems are shown in Figure 3-5a. The pressure at which we observe a significant reduction in the slope of the P/V curve is interpreted as P_{sat} . P_{sat} and SF (calculated using Eq. 3-2) of the oil/gas mixtures at different C₁ mole fractions are plotted in Figure 3-5b. The

results show that P_{sat} increases with increasing C_1 concentration. For example, P_{sat} increases by more than one order of magnitude when the C_1 concentration increases from 10.3 to 70.1 mol%. The rate of increase in P_{sat} is faster when the C_1 concentration is greater than 50 mol%. We failed to measure P_{sat} at C_1 concentration of 80 mol% because the system pressure gets close to the physical limit of the PVT cell. The SF increases from 1.07 to 1.47 when the C_1 concentration increases from 10.3 to 70.1 mol%.

3.4.2.2. Oil/ C_1/C_2 CCE Test

Here, we report the results of CCE tests on four oil/ C_1/C_2 mixtures (see Table 3-2 for detailed feed compositions). P/V data from CCE tests on the oil/ C_1/C_2 systems are shown in Figure 3-5c. P_{sat} and SF of the oil at different C_2 mole fractions are plotted in Figure 3-5d. P_{sat} increases with a decreasing concentration of C_2 . For example, P_{sat} in Figure 3-5d increases by more than threefold (i.e., from 37.58 to 133.28 bar) when C_2 concentration decreases from 100 to 30.3 mol%. However, SF exhibits a reverse trend with decreasing C_2 concentration. For instance, SF reduces from 1.76 to 1.49 when C_2 concentration decreases from 70 to 30.3 mol% at T_{set} . SF is the maximum (1.76) for the oil/ C_2 system. It should be noted that C_2 is more soluble in oil compared with C_1 at the same P and T . Since C_1 molecules are smaller than C_2 molecules, at the same mole fraction of injected gas in the oil phase, having more C_2 in the system results in more swelling compared to the case with less C_2 .

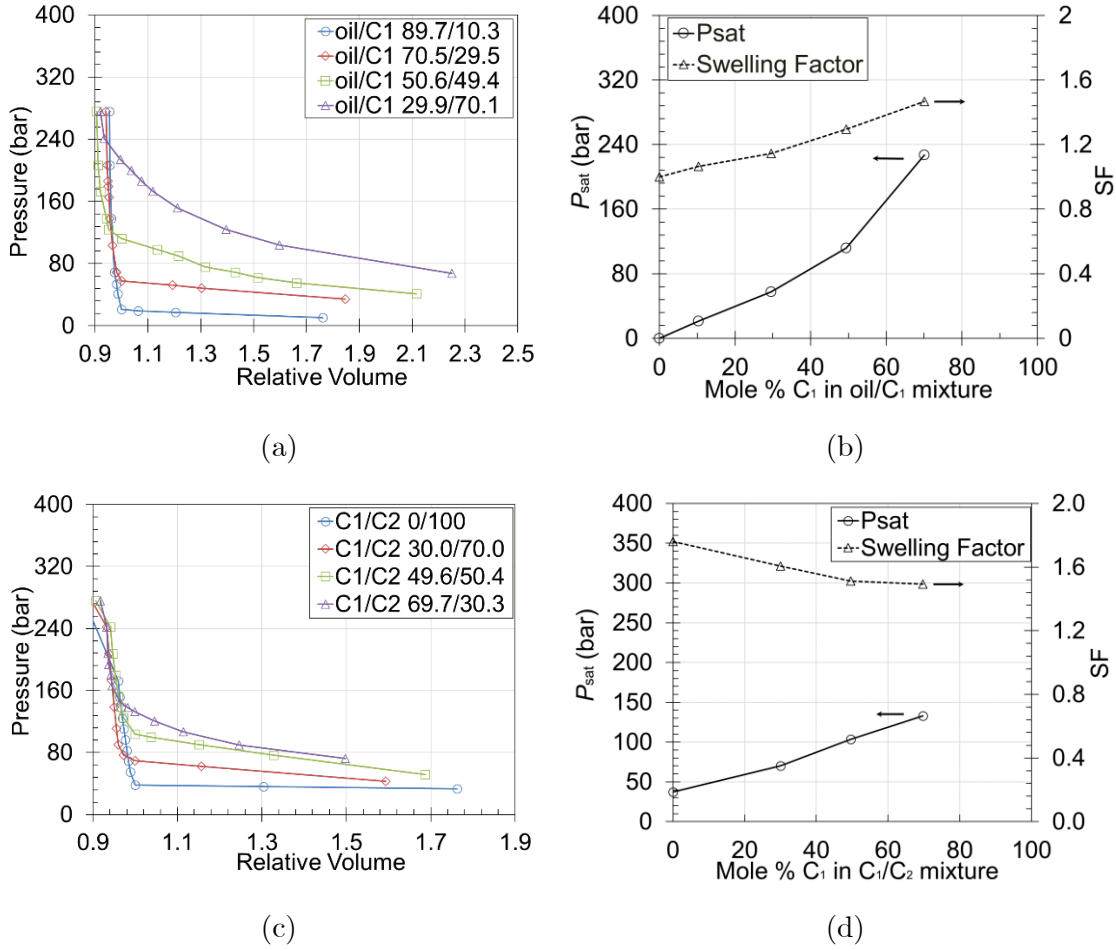


Figure 3-5: The results of CCE tests, P_{sat} and calculated SF at 50°C: (a), (b) for oil/C₁ systems, and (c), (d) for oil/C₁/C₂ systems.

3.4.3. Calculated Oil Density at Different P and T

We correlate the calculated density from the oil-volume measurements using the PVT cell at different P and T using the Tait equation (Dymond and Malhotra 1988). The measured oil densities at different P and T_{set} are used to determine ρ in the CCE tests:

$$\rho(T, P) = \frac{\rho_{\text{ref}}(T, P_{\text{atm}})}{1 - \beta \ln \left(\frac{B + 0.0069P}{B + 0.1} \right)} \quad (3-4)$$

$$\rho_{\text{ref}}(T, P_{\text{atm}}) = 765.6168 + 0.8544T - 0.0021T^2 \quad (3-5)$$

$$\beta = 0.2054 - 5.6598 \times 10^{-4}T \quad (3-6)$$

$$B = 118.5120 - 1.6839 \times 10^5 T^{-1} + 4.4508 \times 10^7 T^{-2} \quad (3-7)$$

where T is temperature (in K), P is pressure (in psig), and ρ is density (in kg/m³). The parameters in Eq. 3-5 are determined by fitting the measured ρ_{ref} . We use Eq. 3-1 to calculate oil density, $\rho(T, P)$. The parameters in Eqs. 3-6 and 3-7 are determined by regressing Eq. 3-4. Figure 3-11 shows the measured and calculated densities using Eqs. 3-4 through 3-7. Detailed oil-density data at different P and T can be found in Appendix A.

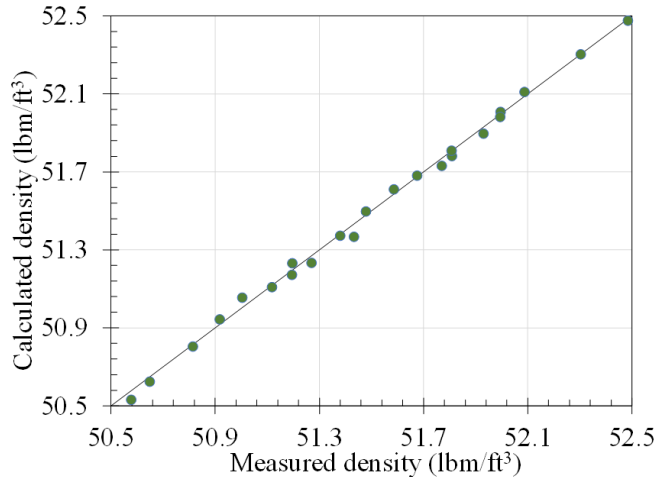


Figure 3-6: Comparison of the measured oil density at different pressures and temperatures with calculated density using Tait equation.

The average absolute relative deviation (AARD) for the calculated oil densities from the experimental data is calculated by

$$AARD = \frac{1}{N} \sum_{j=1}^N \left| \frac{\rho_j^{cal} - \rho_j^{exp}}{\rho_j^{exp}} \right| \quad (3-8)$$

where ρ_j^{cal} and ρ_j^{exp} are the calculated and measured values, respectively, and N is the number of data points. The AARD for the calculated oil density is 0.035%.

3.4.4. Visualization of Gas/Oil Interactions at The Interface

Here, we present results of visualization tests for oil/C₁ and oil/C₁/C₂ (70/30 mol%) systems at T_{set} . Table 3-3 lists the results of two visualization tests. The diffused gas at the end of the soaking period is calculated on the basis of the difference in molar mass of gas in the cell at initial conditions (P_{set}) and at the equilibrium (P_{eq}). We assume that partial pressures created by vaporized oil components at the P_{eq} are negligible. The density values of C₁ (under P_{set} , P_{eq} , and T_{set}) are obtained from the NIST chemical webbook, while densities of C₁/C₂:70/30 mol% (under P_{set} , P_{eq} , and T_{set}) are obtained by flash calculations. Adding 30 mol% of C₂ to the injected gas increases the dissolved gas by 95% (0.440 vs. 0.856 mol). The higher amount of dissolved gas in C₁/C₂ case is attributed to the higher solubility of C₂ in oil compared to C₁. The gas solubility in Table 3-3 is calculated by the amount of gas dissolved in the crude oil at the equilibrium conditions and in a unit of g gas/100 g oil. It can be seen that enriching the injected gas with 30% C₂ leads to a 143% increase in gas solubility.

Table 3-3: Results of the two visualization tests

Test	Injected gas (bar)	P_{set}	Initial conditions		Equilibrium			Gas solubility (g/100g)
			Initial oil	Injected gas (mol)	P_{eq} (bar)	Bulk gas (mol)	Dissolved gas (mol)	
1	C ₁	137.96	1.018	1.757	114.04	1.320	0.437	3.29
2	C ₁ /C ₂ :70/30	137.96	1.011	1.974	106.94	1.109	0.865	8.27

Figure 3-7 shows images of gas/oil interfaces in the cell in two visualization tests. In each test, the captured images correspond to the initial conditions of the test (at P_{atm} ,

T_{set}) (Figure 3-7i), the end of the pressure buildup (at $P_{\text{set}}, T_{\text{set}}$) (Figure 3-7ii), and the equilibrium state (at $P_{\text{eq}}, T_{\text{set}}$) (Figure 3-7iii). In general, it takes approximately 0.27 to 0.29 hours to pressurize the cell from 0 to P_{set} in two tests. We observe oil volumes shrinking (VEF_{ini} of 0.94 in Test 1 and 0.98 in Test 2) during the pressure buildup. P_{eq} values of Tests 1 and 2 are 114.04 and 106.94 bar, respectively. Consequently, equilibrium times in Tests 1 and 2 are 67 and 60 hours, respectively. VEF_{eq} values at the end of the soaking period in Tests 1 and 2 are 1.08 and 1.28, respectively.

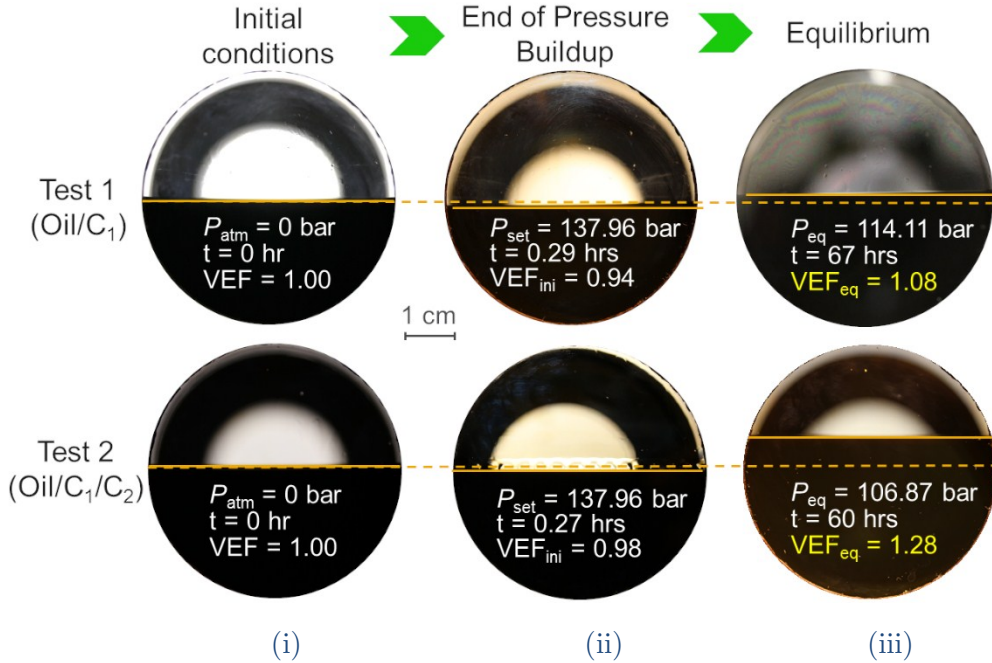


Figure 3-7: Images of oil-gas interfaces at (i) initial conditions at P_{atm} , (ii) end of pressure buildup at P_{set} , and (iii) equilibrium at P_{eq} . The temperature is kept at 50°C during the experiment.

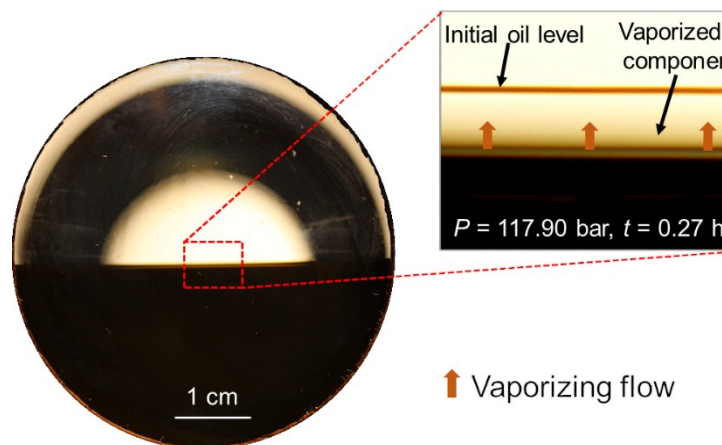
At the equilibrium, Test 2 reaches P_{eq} faster than Test 1, suggesting a higher diffusion rate of C₂ in the oil. By adding 30 mol% C₂, P_{eq} reduces from 114.04 to 106.94 bar, indicating an increase in solubility of the gas phase (i.e., C₁/C₂) compared with the case with pure C₁. The reduction of VEFs at the end of the pressure buildup in both tests

indicates that the oil phase is compressed with increasing injection pressure. Because C₂ is more soluble in oil than C₁ at the same P and T , the VEF_{ini} and VEF_{eq} in Test 2 are higher than those of Test 1. This means that the presence of C₂ in the injection gas enhances oil swelling compared with the C₁ case. Moreover, the gas phase in initial conditions (Figure 3-7i) is transparent. At the end of the pressure buildup (Figure 3-7ii), the gas phases in Tests 1 and 2 turn yellowish. This observation suggests that oil components are transferred from the oil phase to the gas phase, and this is more pronounced in Test 2.

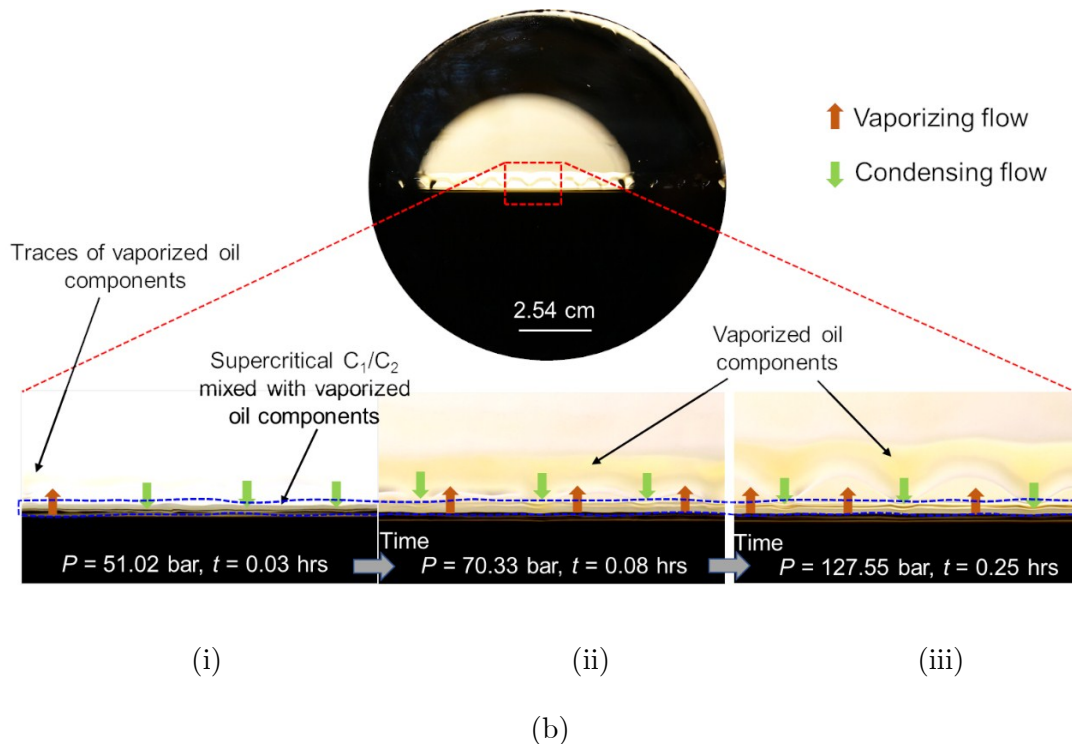
Figure 3-8 shows the interactions at the oil/gas interfaces during the pressure-buildup process in Tests 1 and 2 at 50°C. The horizontal brown line is the initial level of the oil phase that is compressed downward during the pressure buildup. The upward red arrows in Figure 3-8a indicate vaporizing flows of oil components at the oil/C₁ interface. The magnified image of the oil/C₁ interface shows a yellow region on top of the oil phase. The yellow color indicates the presence of oil components transferred from the bulk-oil phase toward the bulk-gas phase and becomes darker in the region close to the oil/gas interface. This is caused by the upward transport of vaporized oil components within the gas phase over time. We did not observe condensing flows during Test 1.

Figure 3-8b shows the vaporizing of oil components and condensing flows of C₁ and C₂ at the oil/C₁/C₂ interface during pressure buildup in Test 2. Figures 3-8b(i) through 3-8b(iii) show the magnified images of the oil/gas interface at three different times. The time frame between Figures 3-8b(i) and 3-8b(iii) is approximately 0.22 hours. At $t = 0.03$ hours [Figure 3-13b(i)], condensing flows (downward green arrows) of C₁ and C₂ occur and traces of vaporized oil components (yellow spots) are observed in the gas phase. We notice a layer on top of the oil phase (in a blue dotted rectangle) that might be a mixture of C₁/C₂ and vaporized oil components. Under these conditions (pressure and

temperature of 51.02 bar and 50°C, respectively), C₁ and C₂ are in supercritical states with corresponding densities of 32.41 and 94.73 kg/m³ (NIST 2018), respectively. The gas-phase becomes yellowish because of the stronger vaporizing flows at t = 0.08 hours [Figure 3-8b(ii)]. This bright-yellow region has a colour gradient similar to what we observed in Test 1 (Figure 3-8a) in terms of color and location. Furthermore, this continuous-concentration gradient becomes stronger with increasing pressure, as shown in Figure 3-8b(iii). The heavier oil components and C₁/C₂ form a thick and dark-yellow layer on top of the oil phase. This might be attributed to the effects of gravity and mass transport caused by the concentration gradient. When the pressure increases to 127.55 bar at t = 0.25 hours, the appearance of several droplets indicates stronger condensing flows of C₁, C₂, and oil components into the oil phase. The vaporizing and condensing flows persist during the soaking process and cease at equilibrium conditions, as shown in Figure 3-7iii.



(a)



(i)

(ii)

(iii)

(b)

Figure 3–8: Images captured at oil-gas interfaces during the pressure buildup process: (a) vaporizing flows in the oil/C₁ test, and (b) vaporizing/condensing flows in the oil/C₁/C₂ test at 50°C.

3.5. Limitations

We present the following limitations:

- The oil swelling and MMP of oil/gas systems are susceptible to the presence of light-oil components. The oil SF is expected to be higher by using live oil because light components enhance the solubility of gas in the oil. On the other hand, P_{sat} and MMP values are lower when using live oil. The light components (C_1 through C_4) in the live oil help reduce the MMP of the gas/oil mixtures.
- The accuracy of MMP measured by the VIT technique and the oil swelling in the visualization tests depend on the quality of images captured throughout the experiments. Because C_2 is in the supercritical state at pressures greater than 48.75 bar and 50°C, the image quality decreases because of the cloudiness of the injected gas.
- The gas mixtures undergo phase changes (from supercritical to gaseous state) when they are transferred from the heated accumulator at high pressure to the heated visualization cell at vacuum pressure. This affects the diffusion of gas to the oil at the early stages of the VIT and bulk-phase visualization tests.

3.6. Summary

We characterized the phase behavior of oil/natural-gas systems by conducting CCE tests between an oil sample from the Montney Formation and injection gases (C_1 and mixture of C_1/C_2 with the molar ratio of 70/30). MMPs of different oil/gas systems were measured using the capillary-rise VIT technique. To complement the CCE and VIT tests, we performed bulk-phase tests to visualize oil/gas interactions at the interface using a visualization cell.

The dominant mechanism for developing miscibility conditions is vaporizing gas drive for the oil/C₁ system and vaporizing/condensing gas drive for the oil/C₁/C₂ systems. The MMP measurements by VIT technique indicate that increasing the C₂ molar fraction in the gas mixtures significantly decreases the MMP of the oil/gas mixtures (from 4,366 psi for oil/C₁ to 1,467 psi for oil/C₁/C₂ with 71.3 mol% C₂). Vaporizing flow of oil components to the gas phase occurs in all visualization tests. The condensation of C₂ into the oil phase in the C₁/C₂ test leads to a higher oil-volume expansion compared with the pure-C₁ case. The presence of C₂ in the injection gas increases the oil swelling factor (i.e., from 1.47 to 1.61) by increasing C₂ molar fraction from 0 to 70 mol%.

The findings presented in this study lead to an improved understanding of the phase behavior and processes leading to miscibility conditions that can be applied to design more effective natural-gas huff 'n' puff operations in tight oil formations.

Chapter 4 : Modelling Phase Behavior of Natural-Gas/Oil Systems

4.1.Introduction

This chapter presents the process of calibrating the PR-EOS against measured CCE and MMP data. The calibrated EOS is used to predict the MMP of the oil/gas systems using ternary diagrams and thermodynamic conditions in the core plug during natural-gas HnP experiments in a later chapter.

4.2.Method

For a gas-injection process, a PR-EOS model needs to be calibrated against the measured CCE and MMP data before being used to predict the MMP of different oil/gas systems (Alavian and Whitson 2010). The main steps to manually calibrate an EOS model include oil characterization, EOS regression, and thermodynamic consistency checks. We plot two-phase equilibrium data from the calibrated EOS models on ternary diagrams to predict the MMPs of the oil/gas systems.

4.2.1.Oil Characterization

The simulated distillation data show that crude oil contains more than 100 different components. It is difficult to measure the thermophysical properties [i.e., critical temperature (T_c), critical pressure (P_c), and acentric factor (ω)] and other EOS parameters for components heavier than C₂₀ (Whitson and Brûlé 2000). The procedure to split plus fractions, lump oil components into pseudocomponents (PCs) and estimate critical properties of the PCs can be found in Appendix A. The oil components are grouped into equal-mass groups with mass-weighted averaging of the properties.

Following this method, a four-PC EOS model is recommended by grouping C₁ through C₁₀ into PC₁, C₁₁ through C₁₆ into PC₂, C₁₇ through C₂₇ into PC₃, and C₂₈ through C₃₀₊ into PC₄. The gas components (i.e., C₁ and C₂) are left ungrouped. To predict the MMP of the oil/gas systems using a ternary diagram, we also group the oil components into one and two PCs. The simplified one- and two-PC EOS models serve as a tool for visualizing and investigating the compositional path on pseudoternary diagrams for oil/C₁ and oil/C₁/C₂ systems.

4.2.2. EOS Regression

The PR-EOS parameters are tuned to match CCE and MMP results for different oil/gas mixtures using the PVTsim software (Calsep A/S 2018). It is essential to obtain a single set of parameters [binary-interaction parameters (BIPs), critical properties, and volume-shift parameters] that can predict the CCE and MMP data of all gas/oil mixtures (in oil/C₁ and oil/C₁/C₂ systems) with acceptable accuracies. The key strategy is using the minimum regression variables (e.g., the BIPs and critical properties of the heaviest PCs) that ensure an optimal solution. The regression variables are adjusted within their estimated uncertainties [i.e., up to 20% of the initially estimated values (Pedersen et al. 2015)]. The following regression variables are used to tune the EOS model:

- BIP. BIPs between C₁/C₂ and the heaviest PCs are tuned to match P_{sat} . The initial values of BIPs between C₁/C₂ and PCs are calculated using the equations available in the literature (Katz and Firoozabadi 1978; Gao et al. 1992).
- Critical properties of PC₃ and PC₄. If tuning BIPs is insufficient to match P_{sat} , T_c , and P_c of the heaviest PCs can be tuned accordingly.
- Volume-shift parameters (CPEN). After matching P_{sat} , ρ_{sat} at T_{set} needs to be matched. The CPEN parameters of C₁, C₂, and PCs, using the PVTsim software

(Calsep A/S 2018), are adjusted to match ρ_{sat} . The initial values of CPEN are calculated using the equations from Pénéroux et al. (1982).

After matching P_{sat} by tuning the BIPs and critical properties of the heaviest PCs, we use the slimtube simulation module in PVTsim (Calsep A/S 2018) to calculate the MMP of the gas/oil system. This iterative process is performed until we reach an acceptable accuracy between P_{sat} and the MMP predictions using the EOS and the measured data.

4.2.3. Thermodynamic Consistency Checks

Because the EOS models are calibrated by changing several regression variables, it is necessary to perform a consistency check to ensure the thermodynamic validity of equilibrium vapor/liquid data and MMP predictions (Whitson and Brûlé 2000; Martinsen et al. 2010). Furthermore, using fewer PCs in EOS models can make two-phase equilibrium calculations more efficient, but this might introduce erroneous predictions of phase behavior because of the reduced dimensionality in composition space (Kaul 1999; Kumar 2016). We perform consistency checks for four-, two-, and one-PC EOS models by comparing phase envelopes and plotting equilibrium K -values at different oil/gas compositions vs. MWs of PCs.

4.2.4. MMP Prediction Using Pseudoternary Diagram

Ternary diagrams are useful tools to visualize the phase behavior of a three-component system in a 2D graph (Lake 1989). We perform two-phase equilibrium calculations at pressures of 101.15 to 301.03 bar and T_{set} by using the calibrated EOS models (i.e., two- and one-PC models) and plot the two-phase equilibrium data on pseudoternary diagrams to determine MMPs of the oil/gas systems. Each tie line stands for a set of equilibrated liquid (L) and vapor (V) composition. The L/V region is formed by connecting the locus of L and V compositions of each tie line. Figure 4-1 illustrates

the displacement process of a vaporizing gas drive and a condensing gas drive. Figure 4-1a presents the oil/C₁-displacement process under a vaporizing gas drive. The vapor phase is enriched with intermediate-hydrocarbon components vaporized from the oil phase (comparing the composition of V₅ with V₁). The process of enriching the vapor phase continues until reaching a critical point at the L/V boundary region. At this point, the vapor phase becomes miscible with the oil phase after several contacts and the length of the equilibrium tie line at miscibility conditions becomes zero (i.e., critical tie line). The oil/C₁/C₂-displacement process under a condensing gas drive is shown in Figure 4-1b. Unlike the vaporizing gas drive, where the vapor phase is enriched by intermediate-oil components, a condensing gas drive relies on the condensation of intermediate-oil components from the gas to the oil. The vapor phase becomes richer because oil components transfer more into the gas phase (comparing the composition of V₅ with V₁). Also, C₂ vaporizes into the gas phase gradually. Furthermore, the liquid phase becomes lighter by condensation of C₂ (comparing the composition of L₅ and L₁).

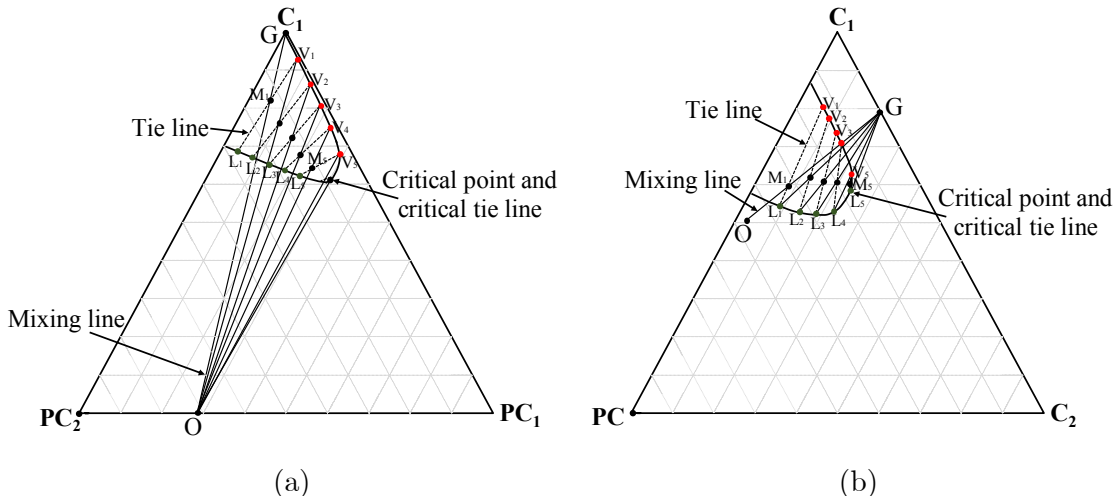


Figure 4-1: Pseudoternary diagrams illustrate a) a vaporizing gas drive and b) a condensing gas drive. O, G, and M represent oil, C₁, C₁/C₂ mixture, respectively.

4.3. Results and Discussions

This section reports the results of EOS model calibration, MMP prediction for the oil/C₁ and oil/C₁/C₂ systems.

P_{sat} , SF, and density data from the CCE tests are used to calibrate one-, two-, and four-PC EOS models and predict the phase behavior/MMP of the oil/gas systems. Regression variables include BIPs between gas/PCs, critical properties of PCs (T_c , P_c), and C_{PEN}. Hydrocarbon/hydrocarbon (HC/HC) BIPs of the PCs are assumed to be zero for the PR-EOS. C_{PEN} parameters are tuned separately to match ρ_{sat} . For consistency, we aim to obtain a single set of parameters for the PR-EOS model that matches the CCE and MMP data of both oil/C₁ and oil/C₁/C₂ systems.

4.3.1. Calibrating EOS Model with Four PCs

4.3.1.1. Oil/C₁ System

Table 4-1 summarizes the related regression parameters for a four-PC EOS model that is calibrated against oil/C₁ CCE data. Table 4-2 presents the optimized BIP values between C₁ and PCs. The HC/HC BIPs are set to zero [default values in PVTsim software (Calsep A/S 2018)]. The values of ρ_{sat} were matched by manually regressing the C_{PEN} of PCs and C₁. Because the ρ_{sat} value calculated by EOS is lower than those from CCE tests, we increase the initial C_{PEN} of the PCs and C₁ stepwise and calculate the corresponding ρ_{sat} until we obtain a reasonable match. The regression was performed prudently with due consideration of the physical trend of EOS parameters with MWs of PCs (e.g., BIPs between C₁ and PCs increase monotonically with increasing MWs of PCs).

Table 4–1: Properties of components in the four-PC EOS model calibrated against oil/C₁ CCE and MMP data

Component	z_i	MW	P_c (bar)	T_c (°C)	ω	V_c (cm ³ /mol)	C_{PEN} (cm ³ /mol)
C ₁	0	16.04	46.00	-82.55	0.008	99.00	-1.41
PC ₁	46.81	106.12	29.32	296.91	0.374	451.19	49.84
PC ₂	29.00	170.91	20.59	404.49	0.595	725.45	102.73
PC ₃	16.11	275.57	12.24	473.01	0.777	1126.81	253.90
PC ₄	8.08	518.47	6.67	537.81	0.983	1767.59	428.58

Table 4–2: Optimized BIP of the four-PC EOS model calibrated against oil/C₁ CCE and MMP data

	C ₁	PC ₁	PC ₂	PC ₃	PC ₄
C ₁					
PC ₁	7.33E-4				
PC ₂	9.33E-4	0			
PC ₃	20E-4	0	0		
PC ₄	35E-4	0	0	0	

Table 4-3 compares P_{sat} , SF, and ρ_{sat} from the CCE tests with the values predicted by the EOS for oil/C₁ systems. The EOS model predicts P_{sat} , SF, and ρ_{sat} of the oil/C₁ systems with AARDs of 8.01, 4.37, and 11.97%, respectively. SF and ρ_{sat} exhibit reverse trends vs. the increasing mole fractions of C₁ in both experimental and predicted data. For instance, the measured SFs increase from 1.07 to 1.47 with increasing C₁ concentration from 10.3 to 70.1%, whereas the measured ρ_{sat} decreases from 804.4 to

766.1 kg/m³. By dissolving more C₁, the volume of oil increases, which leads to higher SF and lower oil density.

Table 4–3: Comparison of the measured data and EOS predictions for the oil/C₁ system

Mol% C ₁ in oil/C ₁ mixture	Experimental Results			Predictions from four-PC EOS Model		
	P_{sat} (bar)	SF (fraction)	ρ_{sat} (kg/m ³)	P_{sat} (bar)	SF (fraction)	ρ_{sat} (kg/m ³)
	10.3	22.06	1.07	804.4	17.86	1.02
29.5	58.54	1.14	790.7	58.19	1.09	899.2
49.4	113.07	1.30	779.5	113.56	1.19	818.3
70.1	227.87	1.47	766.1	197.95	1.47	690.3
AARD (%)				8.01	4.37	11.97

4.3.1.2. Oil/C₁/C₂ Systems

Table 4-4 summarizes the related regression parameters for the four-PC EOS model that is calibrated against oil/C₁/C₂ CCE data. Table 4-5 presents the optimized BIP values between C₁/C₂ and PCs. It should be noted that the parameters in Table 4-5 are identical to those in the four-PC EOS model of oil/C₁, except for the BIP (between C₂ and PCs) and C_{PEN} values of C₂.

Table 4-6 compares P_{sat} , SF, and ρ_{sat} from the CCE tests with the EOS predictions for the oil/C₁/C₂ systems. The EOS model predicts P_{sat} , SF, and ρ_{sat} of the oil/C₁/C₂ systems with AARDs of 4.75, 3.51, and 10.96%, respectively. The measured SFs decrease from 1.76 to 1.49 with decreasing C₂ concentration from 100 to 30.3%, while the measured ρ_{sat} increases from 732.9 to 764.4 kg/m³.

Table 4–4: Properties of components in the four-PC EOS model calibrated against oil/C₁/C₂ CCE and MMP data

Component	z_i	MW	P_c (bar)	T_c (°C)	ω	V_c (cm ³ /mol)	C_{PEN} (cm ³ /mol)
C ₁	0	16.04	46.00	-82.55	0.008	99.00	-1.41
C ₂	0	30.07	48.84	32.25	0.098	148.00	-5.99
PC ₁	46.81	106.12	29.32	296.91	0.374	451.19	49.84
PC ₂	29.00	170.91	20.59	404.49	0.595	725.45	102.73
PC ₃	16.11	275.57	12.24	473.01	0.777	1126.81	253.90
PC ₄	8.08	518.47	6.67	537.81	0.983	1767.59	428.58

Table 4–5: Optimized BIP of the four-PC EOS model calibrated against oil/C₁/C₂ CCE and MMP data

	C ₁	C ₂	PC ₁	PC ₂	PC ₃	PC ₄
C ₁						
C ₂	0					
PC ₁	7.33E-4	0				
PC ₂	9.33E-4	0	0			
PC ₃	20E-4	1E-4	0	0		
PC ₄	35E-4	3E-4	0	0	0	

Table 4–6: Comparison of the measured data and EOS predictions for the oil-C₁/C₂ system

Mol% C ₁ /C ₂ in oil/gas mixture	Mol% C ₂ in C ₁ /C ₂ mixture	Experimental Results			Predictions from four-PC EOS Model		
		P_{sat} (bar)	SF (fraction)	ρ_{sat} (kg/m ³)	P_{sat} (bar)	SF (fraction)	ρ_{sat} (kg/m ³)
69.8	100	38.61	1.76	732.9	37.51	1.62	662.7
71.2	70.0	71.29	1.61	746.9	75.91	1.58	664.0
71.0	50.4	104.46	1.51	755.4	106.52	1.55	666.8
72.0	30.3	134.10	1.49	764.4	144.31	1.52	677.1
AARD (%)					4.75	3.51	10.96

4.3.2.Calibrating EOS Models with Two and One PCs

We use ternary diagrams to graphically study the mechanisms of developing miscibility conditions in different oil/gas systems. On the ternary diagram, pure components (C₁ and C₂) in the injected gas usually occupy one to two apexes, leaving the remaining apexes for the PCs. Therefore, it is not possible to plot the composition of mixtures consisting of C₁/C₂ and four PCs on the ternary diagram. Here, we purposely introduce EOS models with two and one PCs, allowing us to illustrate three-component phase behavior on the ternary diagram. Although these two simplified EOS models are well-calibrated against the relevant CCE data, reducing the dimension of compositional space affects the accuracy of the predicted phase behavior. The models' parameters can be found in Appendix A.

4.3.3.Thermodynamic Consistency Checks

Consistency checks using phase envelopes and equilibrium K -values vs. MWs of the PCs are necessary to ensure that the predicted two-phase equilibrium data from calibrated EOS models are thermodynamically reliable. Figure 4-2 shows phase envelopes of one-, two-, and four-PC EOS models. Figure 4-2a shows the phase envelopes of oil/C₁ systems (from two- and four-PC models) with oil/C₁ molar fractions of 29.9/70.1 mol%. We compare experimental P_{sat} values with predicted values at T_{set} . The two- and four-PC EOS models predict P_{sat} with AARDs of 6.05 and 13.25%, respectively. Figure 4-2b shows the phase envelopes of oil/C₁/C₂ systems (one- and four-PC models) with oil/gas and C₁/C₂ molar fractions of 28.0/72.0 mol% and 69.7/30.3 mol%, respectively. The one- and four-PC EOS models predict P_{sat} with AARDs of 3.03 and 1.69%, respectively. The phase-envelope comparison suggests that predicted P_{sat} values using one-, two-, and four-PC EOS models at T_{set} are reasonable and the two-phase equilibrium calculations using one- and two-PC EOS models can be used for MMP prediction. We encountered technical challenges for matching P_{sat} of the oil/C₁ systems, especially at the gas/oil molar fractions of 70/30 mol%, as reflected in Table 4-3 and Figure 4-2a. The deviation of predicted from measured P_{sat} at this GOR might be caused by the absence of light components in the oil, leading to a higher MMP calculated by slimtube simulation in PVTsim (Calsep A/S 2018). Although the critical points and dewpoint regions of the oil/C₁ and oil/C₁/C₂ systems are clearly outside the operating conditions (isothermal at 50°C), the comparative phase envelopes show a disparity, especially in the case of one vs. four PCs (Figure 4-2b).

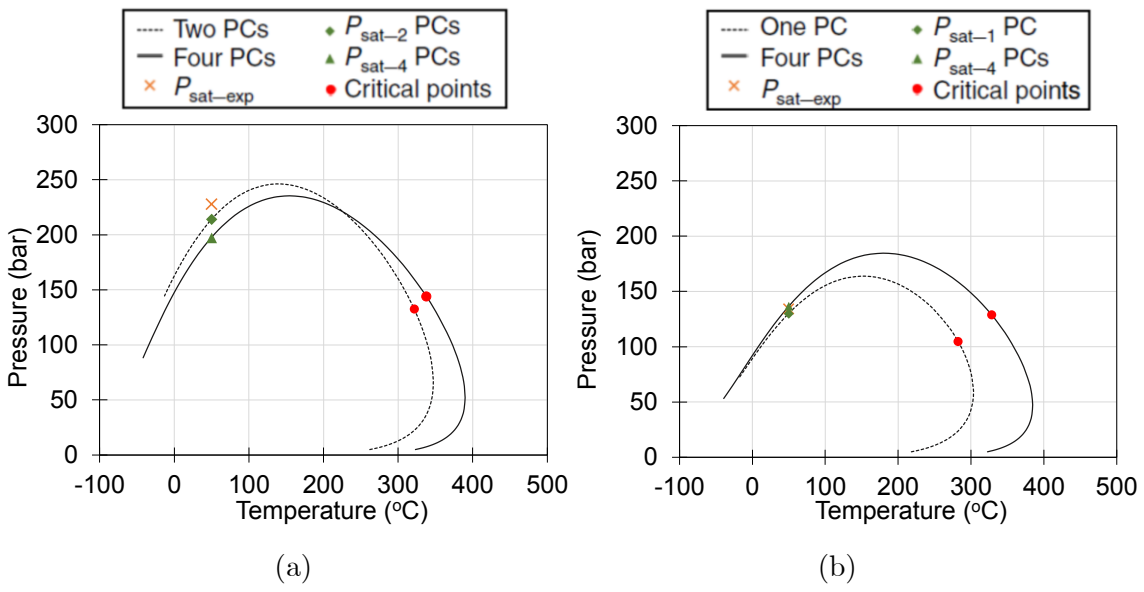


Figure 4–2: Comparison of experimental and predicted P_{sat} using phase envelopes at 50°C:
 a) two- and four-PC EOS models with C_1 mol% of 70.1, and b) one- and four-PC EOS
 model with C_1/C_2 mol% of 69.7/30.3.

Figure 4-3 depicts the trend of K -values vs. MWs for the PCs of the four-PC EOS models at P_{set} and T_{set} . The detailed two-phase equilibrium data for the oil/C1 (Compositions 1 through 4) and oil/C₁/C₂ (Compositions 5 through 8) systems can be found in Appendix A. K -values in Figures 4-3a and 4-3b monotonically decrease with increasing MW of the PCs. The observed trends suggest that the calibrated EOS models are thermodynamically reliable and can be used for phase-behavior predictions. We also performed consistency checks on the trend of K -values for one- and two-PC EOS models, and the results can be found in Appendix A.

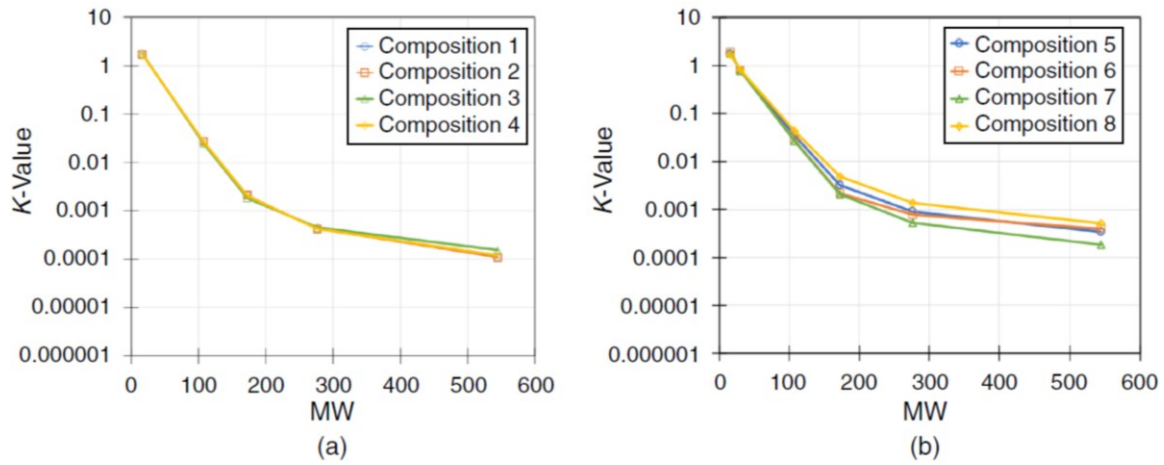


Figure 4-3: Equilibrium K -values versus MWs of the components in the four-PC EOS models for a) oil/C₁ system and b) oil/C₁/C₂ system at 137.90 bar and 50°C.

4.3.4.MMP Prediction using Pseudoternary Diagrams

We estimate the MMP values of the oil/C₁/C₂ systems using two-phase equilibrium data from the calibrated EOS models and pseudoternary diagrams. For consistency, we also perform MMP predictions using the slimtube simulation module in PVTsim software (Calsep A/S 2018) for the four-PC model. Table 4-7 summarizes the measured and predicted MMPs for the oil/C₁/C₂ systems with C₁ of 100, 70.1, and 28.7 mol%. At fixed oil/gas molar fractions and T , increasing C₁ molar fraction increases MMP of the system. For instance, the measured MMP increases approximately threefold (i.e., from 101.15 to 301.03 bar) when C₁ increases from 28.7 to 100 mol% at T_{set} . The purpose of calibrating the one- and two-PC EOS models is only to visualize and understand the changes in the compositional path (phase envelope) relative to changes in pressure and gas composition on a pseudoternary diagram. Although the predicted MMPs using pseudoternary diagrams (two- and one-PC models) are close to the values predicted by the slimtube simulation (four-PC EOS model) and the experiments, we believe that the MMP values predicted by four-PC EOS are more reliable. In fact, MW of the heaviest PC reduced by decreasing the numbers of PCs (518 g/mol for four PCs, 222 g/mol for two PCs, and 186

g/mol for one PC) because of the high fractions of light-oil components in the oil. This reduction in MW might facilitate the matching process for MMP and P_{sat} of one and two PCs compared with those of four PCs. According to the results of Kaul (1999) and Whitson (1983), the accuracy of MMP prediction depends on the MW of intermediates and heavy fractions and the spectra of components represented by the PCs.

Table 4–7: Comparison of the measured and predicted MMPs for the oil/C₁ and oil/C₁/C₂ systems. The slimtube simulation and pseudoternary diagrams are used to calculate MMPs for four-PC and one-, two-PC EOS models, respectively

C ₁ /C ₂ Mol%	Experimental MMP (bar)	MMP predictions from EOS models (bar)		
		four PCs	two PCs	one PC
C ₁ /C ₂ – 100/0	301.03	308.20	307.51	-
C ₁ /C ₂ – 70.3/29.7	188.99	184.50	-	186.02
C ₁ /C ₂ – 28.7/71.3	101.15	99.08	-	102.04

4.3.4.1. Multicontact-Miscibility Achievement by Increasing Gas-Injection Pressure

As demonstrated previously, the key mechanism for developing miscibility conditions for the oil/C₁ system is vaporizing gas drive. Increasing injection pressure leads to shrinkage of the two-phase region until reaching MMP of the oil/gas system. Figure 4-4 illustrates pseudoternary diagrams that are built from the two-phase equilibrium data of the two-PC EOS model at 137.90 and 307.51 bar.

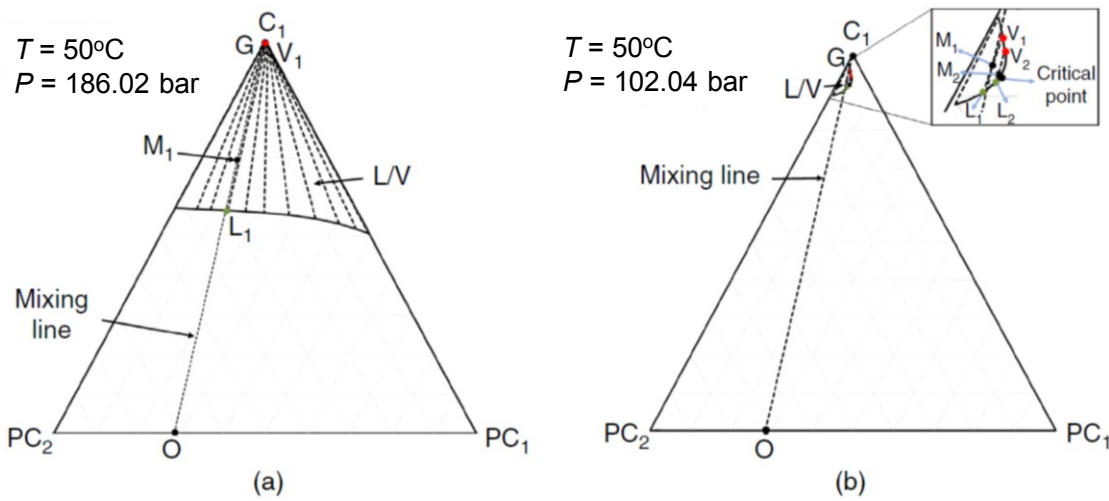


Figure 4-4: Pseudoternary diagrams of the oil/C₁ system at 50°C: a) injection pressure of 137.90 bar, and b) injection pressure of 307.51 bar.

At 137.90 bar, Figure 4-4a shows that after the first contact with the oil, the overall mixture composition is on the mixing line within the L/V region. Any further contacts between the enriched-gas phase and oil do not result in shorter mixture tie lines. This is because the enrichment level is inadequate to move the injection-gas composition, V₁, further toward the PC₁ and PC₂. In this case, the oil/gas displacement does not reach miscible conditions. However, by increasing the injection pressure from 137.90 to 307.51 bar (Figure 4-4b), which is the MMP of this oil/C₁ system, we observe a significant shrinkage of the L/V region. In the L/V region, the gas phase is enriched with intermediate-oil components from the original oil (compare composition of V₂ with that of V₁). The mixture composition moves along a composition path from M₁ toward the boundary of the L/V region and eventually arrives at the critical point (92 mol% C₁, 3 mol% PC₁, and 5 mol% PC₂).

4.3.4.2. Multicontact-Miscibility Achievement by Changing the Injected-Gas Composition

Under field conditions, increasing the gas-injection pressure is not always feasible because of limitations related to gas compressors. Alternatively, we can change gas

composition to arrive at a lower MMP for a given oil/gas system by condensing gas drive, as shown in Figure 4-5. The gas composition can be changed by varying the C₂ molar fraction along the C₁/C₂ side of the diagram. The dominant mechanism for developing miscibility conditions for the oil/C₁/C₂ system is condensing gas drive. Figures 4-5a and 4-5b illustrate pseudoternary diagrams that are built from two-phase equilibrium data of the one-PC EOS model with C₁/C₂ molar fractions of 70.3/29.7 mol% and 28.7/71.3 mol%. The MMPs of the two systems are 186.02 and 102.04 bar, respectively. The critical point in Figure 4-5a has 60.5 mol% C₁, 29.5 mol% C₂, and 10 mol% PC, while it has 28 mol% C₁, 67 mol% C₂, and 5 mol% PC in Figure 4-5b.

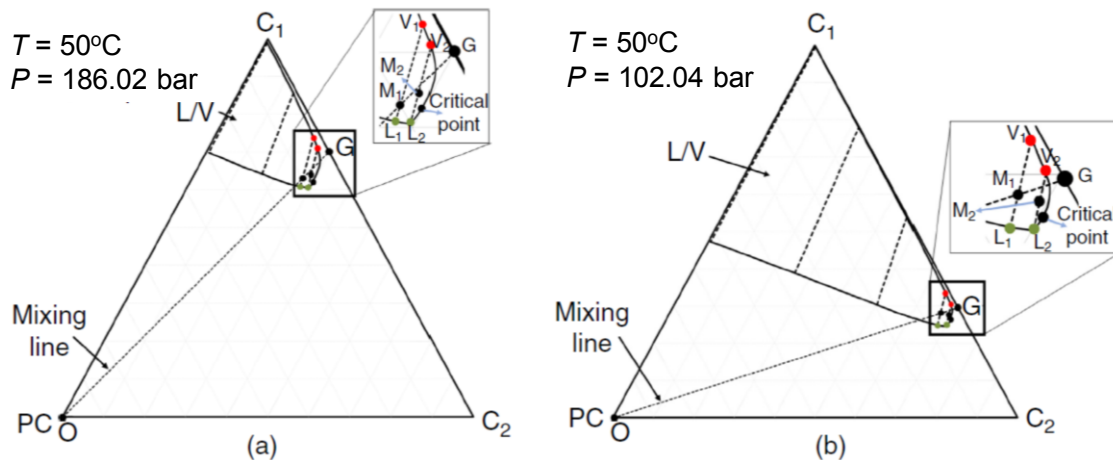


Figure 4-5: Pseudoternary diagrams of oil/C₁/C₂ systems at 50°C: a) C₁/C₂:70.3/29.7 mol%, and b) C₁/C₂:28.7/71.3 mol%.

4.4.Limitations

We present the following limitations:

- Lumping the oil components to PCs in the calibrated EOS affects the accuracy of predicted phase behavior and the MMP of the oil/gas systems
- The effects of nanoconfinement on phase behavior calculations is neglected.

4.5. Summary

In this chapter, we conducted phase-behavior modeling of natural-gas/oil systems to predict the MMP of gas/oil mixtures and predict thermodynamic conditions of gas/oil systems during gas injection.

The results show that the dominant mechanism for developing miscibility conditions is vaporizing gas drive for the oil/C₁ system and vaporizing/condensing gas drive for the oil/C₁/C₂ systems. The miscibility conditions can be achieved by either increasing gas-injection pressure (from a reservoir pressure of 137.90 bar up to approximately 301.03 bar in the oil/C₁ system) or increasing the molar fraction of C₂ in the gas mixtures (from 29.7 to 71.3 mol% to reduce the MMP of oil/gas systems 188.99 to 101.15 bar). The presence of C₂ in the injection gas increases the oil swelling factor (i.e., from 1.47 to 1.61) by increasing C₂ molar fraction from 0 to 70 mol%. Reasonable PR-EOS models were calibrated against CCE and MMP data. The predicted MMPs by plotting two-phase equilibrium data on ternary diagrams have good agreement with the measured ones.

Chapter 5 : Experimental Study of Gas-Transport and Recovery Mechanisms during A Natural-Gas Huff ‘n’ Puff Cycle

5.1.Introduction

This chapter experimentally investigates mass-transport and recovery mechanisms of a natural-gas HnP process under core-plug conditions. We conduct HnP tests using an ultratight Montney core plug and natural gas samples (C_1 and a mixture of C_1/C_2 with the molar ratio of 70/30) under reservoir conditions ($P = 137.9$ bar and $T = 50^\circ\text{C}$). In each test, we soak the plug in the natural gas for 168 hours using a visualization cell. We measure pressure decline during the soaking period, visualize oil production on the plug’s surface, and calculated the oil RF to investigate (i) mass-transport mechanisms (advection vs. diffusion) during injection and soaking phases, and (ii) oil-recovery mechanisms during the whole process. The tests also allowed us to compare the effects of gas composition and the initial difference between injected gas and pore pressures on gas-transport and recovery mechanisms.

5.2.Materials

5.2.1. Core Samples

The plug used in this study is from a well drilled in the Montney tight-oil Formation in northwestern Alberta with the petrophysical properties listed in Table 5-1. Since the objective of the study is to compare the effects of gas composition and ΔP_i on gas-transport and oil-recovery mechanisms, the plug is reused to eliminate the effects of heterogeneity.

After the coring operation, the whole core was cut into one-meter core cylinders. Cylindrical plugs were then cut horizontally from the cores and cleaned using a Dean-Stark solvent extraction system before performing routine core analysis. The porosity and air permeability of the plugs were measured by helium porosimetry and pulse-decay techniques, respectively. The plug used in this study and the offset used for petrophysical characterization were cut from the same cylinder and at the same depth.

Broken pieces collected during cutting the plugs were used for X-ray diffraction (XRD) analyses, assuming that their mineralogy is similar to that of the plug. Table 5-2 lists the mineralogy of the plug obtained from XRD analysis. Quartz (44 wt%) is the dominant mineral, followed by dolomite (14%), plagioclase (9%), potassium feldspars (10%), and pyrite (5%). Clay minerals (illite/smectite and illite/mica) account for 18 wt% of the whole rock weight.

Table 5–1: Petrophysical properties of the plug

Measured depth (m)	Air permeability, k_{air} (nD)	Porosity, helium (%) bulk volume)	Grain density (kg/m ³)	Diamete r (cm)	Length (cm)
2452.33	60	3.5	2.73	3.6	6.3

Table 5–2: Mineralogy of the Montney plug from the XRD analysis

Mineral	wt %
Quartz	44
K-Feldspar	10
Plagioclase	9
Dolomite	14
Pyrite	5
Total Clay	18
Total	100
Clay Mineral	Relative Clay %
Illite-Smectite	66
Illite-Mica	34
Total	100

Figure 5-1 shows Mercury-Injection Capillary Pressure (MICP) data of the plug. The median pore-throat size is 0.016 µm. The pores are classified as mainly mesopores (76% of the total pore space) according to the pore-size classification of the International Union of Pure and Applied Chemistry (Sing et al. 1985). It is well-known that a fraction of the pores (small pores) cannot be detected by the MICP technique because of pore-accessibility issues.

Figure 5-2 shows images obtained by analyzing the polished surface of offset-end pieces using a scanning electron microscope (SEM) equipped with an energy dispersive X-ray spectrometer. The samples were sputter-coated with platinum/palladium before SEM imaging. The SEM images were taken in secondary electron mode and at 10,000X magnification. Inter-crystalline pores (yellow arrows) are located between clays and cements in Figure 5-2b.

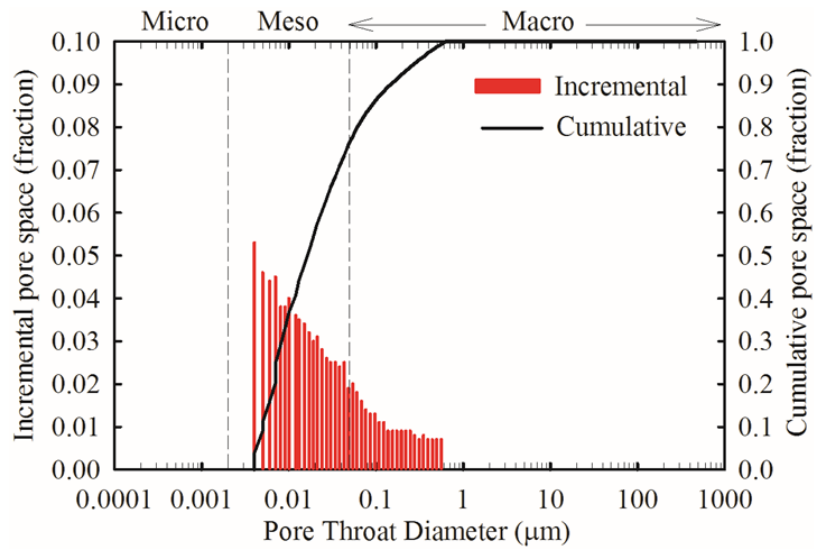


Figure 5–1: Pore-throat size distribution from the MICP data.

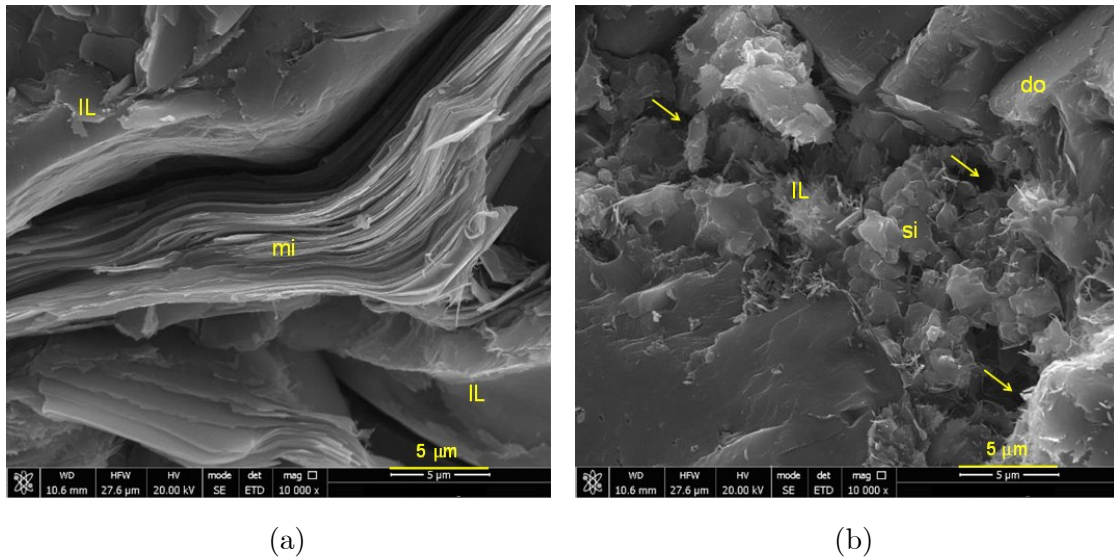


Figure 5–2: SEM images of (a) clay components include illite (IL), and mixed-layers of illite-mica (mi) flakes, (b) dolomite cement (do) is widespread, while silica cement (si) is commonly mixed with illite. Illite mineral is observed as clay ribbons. Inter-crystalline pores (yellow arrows) are located between clays and cements.

5.2.2. Fluid Samples

We used a dead-oil sample from a well drilled in the Montney Formation in northwestern Alberta, Canada, and conducted the experiments at representative

reservoir pressure (P_{set}) and temperature (T_{set}) of 137.90 bar and 50°C, respectively. The C₁ and C₂ samples used in this study have a purity of 99.999%. The fluid properties and oil compositional analysis are presented in Table 3-1 and Figure 3-1 in Chapter 3, respectively.

5.3.Method

5.3.1.Experimental Setup

We performed HnP tests on an oil-saturated plug at P_{set} and T_{set} to investigate mechanisms that control gas transport into and oil production from the plug at different phases of the HnP process. Figure 5-3 illustrates schematically the natural-gas HnP process conducted on the oil-saturated plug. The plug was coated by silicone to allow only one end-face open for gas and oil transports, mimicking the fracture face shown in Figure 5-3. Moreover, the coating is expected to reduce the ratio of surface area in contact with gas to the volume of gas. Here, we estimated oil RF for comparing and ranking different recovery mechanisms. To evaluate the effects of gas composition on gas-transport and oil-recovery mechanisms, C₁ and a mixture of C₁/C₂ with the molar ratio of 70/30 were used as injected gases.

Table 5-3 lists the experimental conditions of two sets of tests (Sets 1 and 2). The pressure values in Table 5-3 and subsequent sections are gauge pressure. The main difference between Sets 1 and 2 is the value of $\Delta P_i = P_{\text{set}} - P_i$, which is defined as the difference between injected gas pressure (at P_{set}) and initial pressure of the oil in the plug (pore pressure or P_i). For Set 1 with $\Delta P_i \approx 138$ bar, gas transport is controlled by both convection and diffusion, representing injecting gas at pressures above the current reservoir pressure. For Set 2 with $\Delta P_i \approx 4$ bar, the convective flow is significantly smaller, representing injecting gas at the current reservoir pressure. The selected P_{set} values are

below MMP of the gas/oil systems (301.03 bar for oil/C₁ and 188.99 bar for oil/C₁/C₂ with 30 mol% C₂).

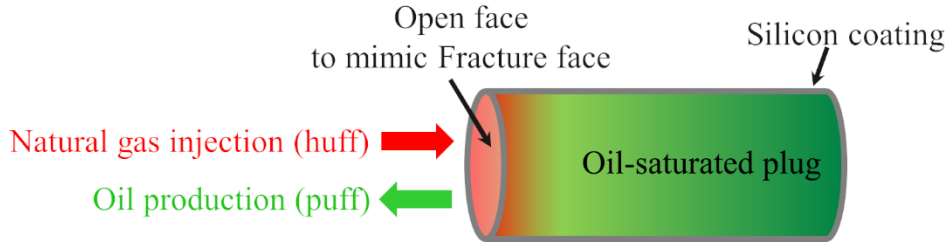


Figure 5–3: Schematic illustration of fluid flow through the open face of the oil-saturated plug during the natural-gas HnP process.

Table 5–3: Initial conditions of the HnP tests. The temperature is kept at 50°C during the tests

Set	Injected gas	P_i (bar)	P_{set} (bar)	$\Delta P_i = P_{set} - P_i$ (bar)
1	C ₁	0	138.58	138.58
	C ₁ /C ₂ :70/30	0	138.52	138.52
2	C ₁	134.45	138.44	3.99
	C ₁ /C ₂ :70/30	134.43	138.37	3.94

The tests were conducted using a high-pressure and high-temperature visualization cell schematically illustrated in Figure 5–4. As illustrated in Figure 5–4, only one end of the plug is open for contact with gas during injection, soaking, and depressurization periods. The internal volume of the cell was reduced from 587 to 390 cm³ (by placing solid blocks) to reduce the volume ratio of injected gas to oil in the plug, and to stabilize the plug during the gas injection. The clearance between the open face and sight glass was kept approximately at 1 to 2 mm. The small clearance was designed to avoid effects of light refraction during image capturing and video recording.

The plug used in this study has a high volume of mesopores (76% of the total pore space) and amount of illite clays (18 wt%), gas adsorption might occur and influence the gas transport during the HnP experiments. In an experiment to measure the adsorption of C₁ on montmorillonite, kaolinite, and illite clays, Liu et al. (2013) reported C₁ was adsorbed only on the external surface of kaolinite and illite; however, adsorption occurred in both surface and interlayer space of montmorillonite. It is important to mention that the plug was reconditioned (i.e., drying under vacuum pressure and 90°C in the cell for two days) after each test. The reconditioning might help release most of the residual oil [oil components trapped inside nanopores after pressure-depletion phase (Bui and Akkutlu 2017)] and gas in the plug before starting the next HnP experiment.

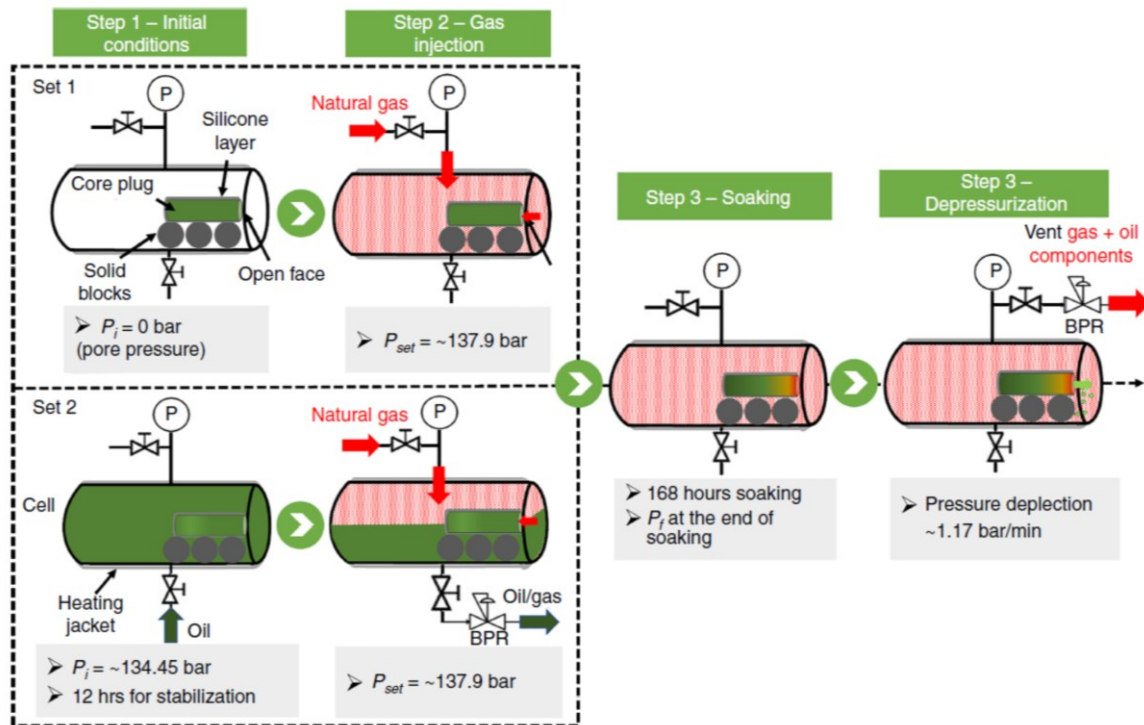


Figure 5-4: Experimental setup and procedure for conducting HnP tests at T_{set} . P and BPR stand for pressure and back-pressure regulator, respectively. The initial pore pressure (P_i) in Set 1 is atmospheric while it is ~134.45 bar in Set 2.

5.3.2. Experimental Procedure

The experimental procedure for the natural-gas HnP process includes four steps: (1) Setting up initial conditions, (2) gas injection (huff), (3) soaking, and (4) depressurization (puff) process as demonstrated in Figure 5-4.

Step 1, saturating and aging the plugs to restore reservoir conditions, includes the following substeps:

1. The plug was not cleaned by any solvents to remove residual oil and connate water. The use of high-boiling point solvents, e.g. toluene in Soxhlet extraction, may cause (i) significant dehydration of clay-bound water, (ii) dissolving organic materials, and (iii) an increase in helium porosity resulting from possible opening of isolated microporosity (McPhee et al. 2015). Instead, the plug was dried in an oven at 90°C until a stable weight was recorded over time. It is worth noting that some residual hydrocarbon and also salts might remain in the plug after the drying process.
2. The oil sample was filtered using a 1 µm filter paper to remove solid impurities.
3. The plug was vacuumed and aged in the oil at $P = 206.84$ bar and $T = 50^\circ\text{C}$ for two days to restore reservoir conditions. The ratio of imbibed oil volume by forced imbibition to helium porosity is approximately 1.24 for the plug (2.79 vs. 2.24 cm³). The observed difference between pore volume (PV) values may be caused primarily by sample heterogeneity. The imbibed oil volume of 2.79 cm³ was used as initial oil volume in the oil-recovery calculations.
4. Except for the open face, other sides of the plug were coated by a layer of silicone with a thickness of about 0.6 mm. Afterward, the plug was weighed again and used for the tests.

5. The silicone coating was repeated after each test to ensure the integrity of the coating layer. The tested gas might permeate through the coating layer owing to pressure difference, affecting mass transport during the experiments. Sadrzadeh et al. (2009) reported that an increase of 5.07 bar in the pressure difference on silicone membranes increases the permeability coefficient of gases (C_3H_8 , CH_4 , and H_2) through the membranes.
6. The temperature of the cell and accumulators are set at T_{set} by using heating jackets.
7. The tests were conducted under two different initial pore-pressure conditions to examine effects of advective and diffusive gas transport into the plug:
 - Set 1: The oil-saturated plug was transferred from the aging accumulator to the heated cell. The cell was then vacuumed and ready for the gas injection phase.
 - Set 2: The cell was filled with oil and pressurized up to $P_i \approx 134.4$ bar. The system was left static for 12 hours to allow for pressure and temperature stabilization.

Step 2, gas injection (huff) process, includes the following substeps:

1. Set 1: After completing the vacuum step, the gas sample was immediately introduced into the cell from the top valve to reach P_{set} to minimize oil production from the plug caused by vacuum conditions. Before gas injection, the pressure inside the plug was expected to be higher than the cell. Therefore, oil production would occur through the open face if the vacuumed conditions persisted. It should be noted that the pressure in the cell was gradually increased to avoid causing induced microfractures in the plug.

- Set 2: A back-pressure regulator (BPR) was installed at the bottom of the cell to control the discharge pressure. The BPR was set at P_i before starting the test. The gas sample was injected into the cell from the top valve at a pressure higher than the BPR's set pressure (by ~4 bar) to gradually displace the oil. The gas injection ended when no more oil was observed from the outlet. All valves were then closed to start the soaking period.

Step 3, soaking process, includes soaking the plug in the gas samples for 168 hours (~7 days). This soaking period is deemed sufficient to investigate (i) the mechanisms responsible for gas transport into the plug, and (ii) the possibility of oil production by total system compressibility, vaporization, oil swelling, and gas-expansion mechanisms. In field practices, Jacobs (2019) reported that a soak-time duration of 5 to 20 days yields the highest oil recovery.

Step 4, depressurization (puff) process, includes venting the gas through the top valve and reducing the cell pressure (at an average depletion rate of ~1.17 bar/min) from the final soaking pressure (P_f) to P_{atm} using the BPR. This pressure depletion rate is selected on the basis of minimizing the change of tensile stress during unloading cycle. According to Moulu (1989), the average depletion-rate reported in the literature is often much greater than in the field. The author also reported that increasing depletion rate led to a faster increase in critical gas saturation (S_{gc}) and higher oil recovery.

To determine the composition of the vented gas, it was collected using three gas cylinders (total volume of 1 100 cm³) with pressures of 68.95, 35.85, and 15.16 bar for gas chromatography (GC) analysis. A predetermined amount of gas from each cylinder was collected and injected into a gas analysis bag for compositional analysis. The resulting composition and concentration (in cm³/m³ unit) of each oil component were reported. The concentration of the oil components had an accuracy of ±0.1 cm³/m³. The

total volume of vaporized oil of each test was obtained by multiplying the total oil-component concentration by the total volume of the three cylinders.

Images and videos of the open face were captured during gas injection, soaking, and depressurization phases. The final oil RF was calculated by the weight-balance method. The reading accuracy of the balance is 0.1 mg. The volume ratio between the gas in the cell and the oil in the plug at P_{set} is significantly high (390 vs. 2.79 cm³), leading to overestimation of oil RF compared with field cases.

5.4. Results and Discussions

This section reports the results of gas-transport mechanisms during the soaking period, visualization and quantification of oil-recovery mechanisms, and recovery mechanism during pressure-depletion phase of the HnP tests.

5.4.1. Gas-Transport Mechanisms during Soaking Period

Here, we present results of soaking the oil-saturated plug in C₁ and a mixture of C₁/C₂ (70/30 mol%) for 168 hours at T_{set} . Table 5-4 lists the results of four HnP tests. The P_i of the plug before starting gas injection in Sets 1 and 2 are approximately 0 and 134 bar, respectively. The leaked-off gas at the end of the soaking period is calculated on the basis of the difference in molar mass of gas in the cell at initial conditions (P_{set}) and at the end of the soaking period (P_f). We assume that partial pressures created by vaporized oil components at the P_f are negligible. For the same gas composition, the leaked-off gas for the tests with $\Delta P_i > 0$ bar is higher than that with the $\Delta P_i \approx 0$ bar. For instance, the amount of leaked-off gas increases by approximately 45% (0.045 vs. 0.031 mol) and 8% (0.104 vs. 0.096 mol) in C₁ and C₁/C₂ tests, respectively. Adding 30 mol% of C₂ to the injected gas increases the leaked-off gas by 131% in Set 1 (0.104 vs. 0.045 mol) and 210% (0.096 vs. 0.031 mol in Set 2).

Table 5–4: Results of the four HnP tests

Set	P_{set} (bar)	Injected gas	Initial conditions		End of soaking period			End of test
			Initial oil (mol)	Injected gas (mol)	P_f (bar)	Bulk gas (mol)	Leaked-off gas (mol)	Produced oil (mol)
1	138.58	C ₁	0.011	2.293	136.03	2.248	0.045	0.004
	138.52	C ₁ /C ₂ :70/	0.011	2.623	133.34	2.519	0.104	0.005
2	138.44	C ₁	0.011	2.291	136.65	2.260	0.031	0.003
	138.37	C ₁ /C ₂ :70/	0.011	2.620	133.62	2.524	0.096	0.004

During the soaking period, pressure in the cell declines owing to gas dissolution into the oil-saturated plug. Figure 5-5a shows pressure-decline profiles during the soaking period of the four HnP tests. The time span of the soaking period is approximately 168 hours. For the same gas composition, the absolute pressure-drop (from P_{set} to P_f) values in Set 1 are higher than those in Set 2. For instance, they are 5.28 and 4.75 bar in Set 1-C₁/C₂ and Set 2-C₁/C₂ test, respectively. The observed difference is attributed to the stronger advective gas transport into the plug in Set 1.

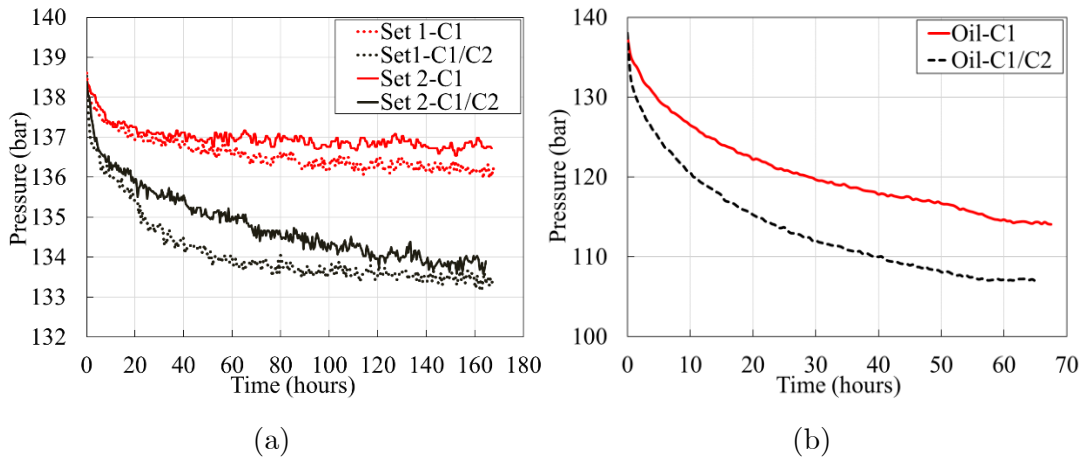


Figure 5–5: Pressure-decline profiles during (a) ~ 168 hours soaking period of HnP tests, and (b) soaking period of oil/C₁ and oil/C₁/C₂ tests at T_{set} .

We compare pressure-decline profiles of the HnP tests with those of the bulk-phase tests in Figure 5-5b to investigate the hindrance of gas dissolution into oil by rock matrix. Equilibrium pressures (P_{eq}) of the bulk-phase oil/C₁ and oil/C₁/C₂ tests are 114.07 and 106.95 bar, respectively. The time to reach P_{eq} and pressure-drop value in the oil/C₁/C₂ are shorter and higher than the oil/C₁ test (67.5 vs. 65 hours and 31.09 vs. 23.53 bar), respectively. Absolute pressure-drop values of HnP tests are approximately one order of magnitude lower than the bulk-phase ones, e.g. 2.55 vs. 23.53 bar in Set 1-C₁ and oil/C₁ tests.

The similarity of pressure-decline profiles between the HnP and bulk-phase tests suggests that they may experience similar gas-transport mechanisms. The bulk-phase pressure-decline trend is similar to the HnP tests with a sharp decrease at the beginning and a gradual decline towards the end of the soaking period. At the early soaking period in bulk-phase tests, pressure decline is affected by the resistance to mass transfer at the gas/oil interface (Rasmussen and Civan 2009; Pacheco-Roman and Hejazi 2015). Moreover, there is a higher concentration gradient of gas near the gas/oil interface, resulting in faster gas transport and high-pressure drop in the early soaking period. When the soaking progresses, molecular diffusion dominates gas transport into the oil. A similar gas-transport process is believed to occur during the soaking period of HnP tests. The pressure drop in Set 1 is higher than in Set 2 owing to the effect of stronger advective flow in a region close to the plug's surface. During HnP process in tight reservoirs, pressure-driven advective gas transport is dominant during gas-injection and early soaking periods (Alharthy et al. 2018), while molecular diffusion is dominant when the soaking period progresses (Yu et al. 2015; Javadpour 2009, Hoteit and Firoozabadi 2009). In a modeling study of production from shale reservoirs, Ozkan et al. (2010) reported that Darcy-dominated flow occurs in the region close to the fracture/matrix interface and the diffusive flow dominates in the matrix with permeabilities in nanodarcy range.

In both HnP and bulk-phase tests, adding C₂ significantly increases the pressure-decline rate. In Figure 5-5b, the lower P_{eq} in oil/C₁/C₂ compared to the oil/C₁ test is attributed to the higher solubility of C₂ in oil compared to C₁ (8.27 vs. 3.29 g/100g). At the equilibrium, the time to reach P_{eq} in oil/C₁/C₂ is shorter than the oil/C₁ system, suggesting a higher diffusion rate of C₂ in the oil. According to Li et al. (2020), the solubility and diffusion coefficient of C₂ in Bakken oil (under 90 bar and 109.8°C) are about 8.5 times (~9 vs. ~77 g/100g) and 2.7 times (~310⁻⁹ vs. 8.210⁻⁹ m²/s) higher than those of C₁. This observation is complemented by bulk-phase visualization tests presented in Chapter 3. In the oil/C₁ test, vaporizing flows (upward red arrows) of oil components to the gas phase occur during the gas-injection phase (Figure 5-13a), while vaporizing and condensing flows coexist during the same period in the oil/C₁/C₂ test (Figure 5-13b). The appearance of the condensing flows (downward green arrows) of C₁, C₂, and vaporized oil components into the oil phase means stronger gas transport into the oil. This leads to more pressure drop and higher gas diffusion rate than pure C₁ cases. Video clips recorded during the gas-injection phase of the bulk-phase tests are provided in the Supplementary Material in Appendix B.

5.4.2. Visualization and Quantification of Oil-Recovery Mechanisms during A Natural-Gas HnP Cycle

Figure 5-6 shows the surface of the oil-saturated plug (denoted by surface) corresponding to the four stages of the four HnP tests. Video clips recorded during the gas-injection and depressurization phases of the HnP tests are provided in the Supplementary Material in Appendix B.

1. Step 1. Images show the surface at initial conditions of Set 1 (at P_{set} , T_{set}) and Set 2 (at P_{atm} , T_{set}). They are all wet by the oil phase. The surface in Set 2 is unclear because the plug is fully immersed in the oil at P_{set} .

2. Step 2. Images show the surface at the end of the gas injection phase (138.58 and 138.52 bar in Set 1-C₁ and -C₁/C₂, 138.44, and 138.37 bar in Set 2-C₁ and -C₁/C₂ tests, respectively). The total time required for the gas-injection process is approximately 0.3 hours in Set 1 and 0.22 hours in Set 2. The surface changes from wet to partially dry in Set 1, while it remains wet by the oil phase throughout the gas-injection phase in Set 2.
3. Step 3. Images demonstrate the surface after approximately 168 hours of soaking in C₁ and a mixture of C₁/C₂. During the soaking period, the surface becomes completely dry in Set 1, while it remains wet in Set 2.
4. Step 4. Images show comingled flows of gas and oil on the surface during the depressurization process. The observed non-uniform oil production in Set 2 may be caused by the interaction of the coating layer with the oil during gas/oil displacement in Step 2.

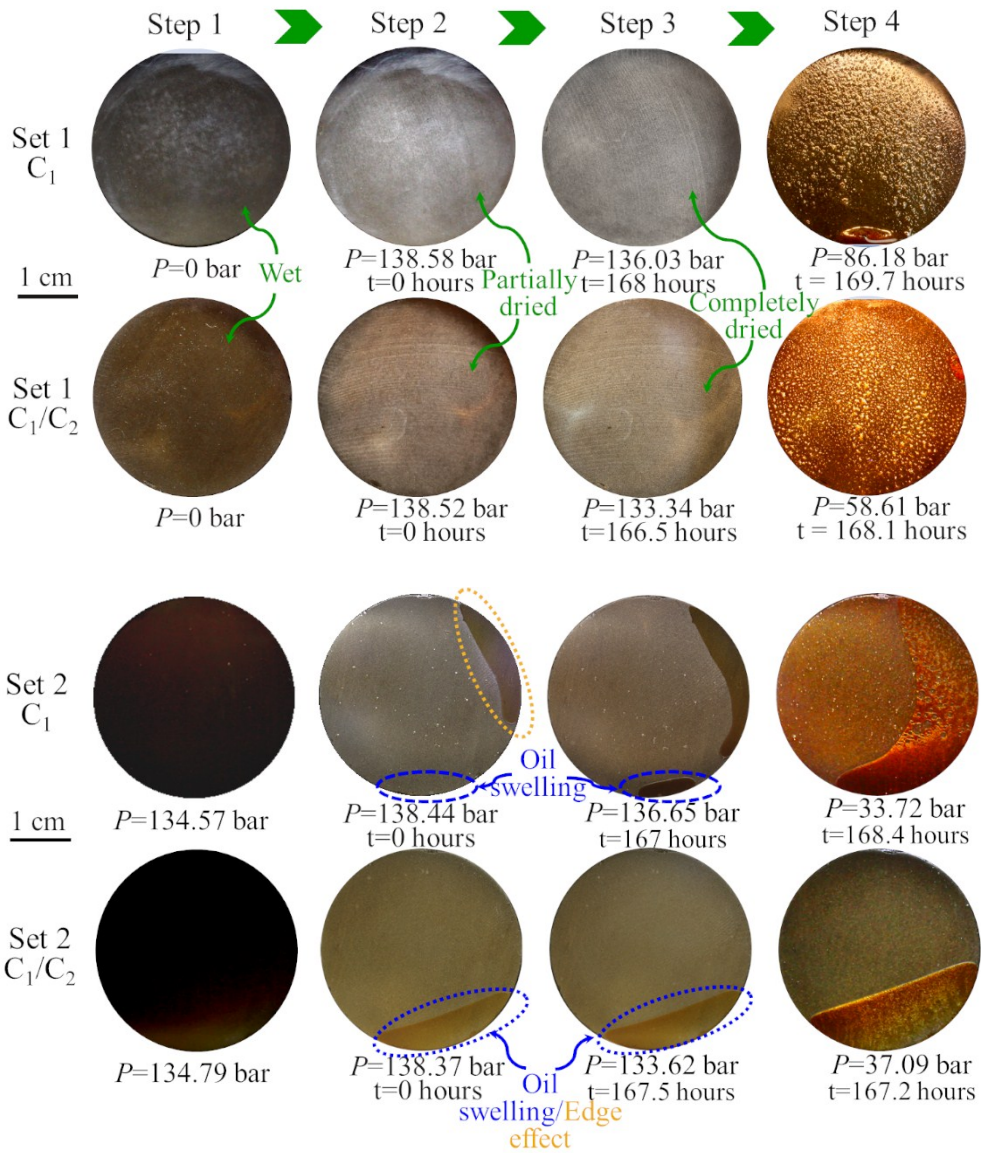


Figure 5–6: Images of the plug surface during initial conditions (Step 1), gas injection (Step 2), soaking (Step 3), and depressurization (Step 4) of all tests at T_{set} .

The experimental results show that four recovery mechanisms, i.e. total system compressibility, vaporization of oil components, oil swelling, and gas expansion, are involved in the HnP process.

5.4.2.1. Total System Compressibility

This recovery mechanism is caused by the presence of ΔP_i and is only expected to occur in Set 1. It can be visualized in Figure 5-6 by the changes of surfaces from wet to partially dry (compare the surface in Steps 1 and 2). The oil production during the injection phase of Set 1 is attributed mainly to the change in initial pore and oil volume caused by total system compressibility. Because the plug is very tight and the gas-injection duration is short, most of the oil inside the pores farther from the surface is still at approximate to P_i . Therefore, we can assume that oil recovery by oil compressibility is negligible. Other recovery mechanisms, such as vaporization and oil swelling, may also occur in the injection phase and will be discussed in the next subsections. We calculate the change of initial oil volume caused by rock and oil compressibility at T_{set} :

$$\frac{\partial V}{V} = c_f \times \partial P \quad (5-1)$$

where $V = 2.79 \text{ cm}^3$ is the initial PV; ∂V is the change in PV (cm^3); c_f is the isothermal coefficient of rock compressibility ($1/\text{bar}$); $\partial P \approx 137.9 \text{ bar}$ is the differential pressure when pressurizing the cell from P_i to P_{set} . The c_f at the porosity of 3.5% is $1.48 \times 10^{-4} \text{ 1/bar}$ (Geoscience BC 2011). The estimated ∂V using Eq. 5-1 is 0.06 cm^3 . Davudov and Moghanloo (2018) and Lan et al. (2017) reported that PV compressibility of gas shale changes as a function of effective stress and its change affects pore connectivity, permeability, and gas recovery.

5.4.2.2. Vaporization of Oil Components

Figure 5-7 compares the mole fraction of oil components (C_5 to C_{12}) vaporized to the gas phase during the HnP experiments, obtained by GC analysis of the collected gas samples. Because the mole fraction of gas in the collected samples is significantly high compared to the vaporized oil components, only mole fractions of vaporized oil

components are normalized and plotted for comparison. In particular, C₈ to C₁₀ components account for more than 70 mol% of the vaporized oil volume. The volumes of vaporized oil in Set 1-C₁, Set 1-C₁/C₂, Set 2-C₁, and Set 2-C₁/C₂ are 0.02, 0.05, 0.01, and 0.03 cm³, respectively. The molar ratio of the vaporized oil to the original oil in the plug is 0.47 to 1.68 mol%.

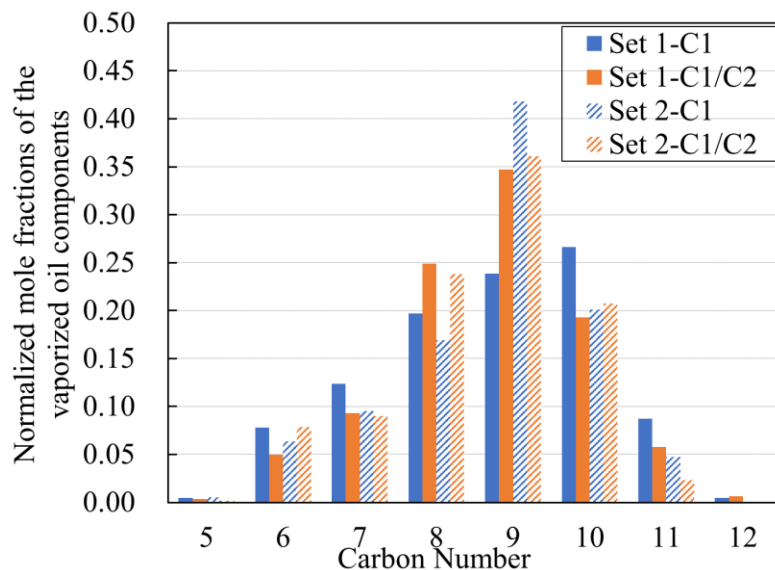


Figure 5–7: Normalized mole fractions of the vaporized oil components from the GC analysis.

The vaporization is quantitatively evaluated using GC analysis of produced gas samples. The change of the surface state from wet to partially/completely dry during injection and soaking periods suggests vaporization of oil components from the surface to bulk-gas phase. In Figure 5-7, the amount of vaporized oil in the C₁/C₂ tests are higher than that in C₁ cases. This can be explained by the higher solubility of C₂ in oil compared to C₁. Moreover, the developed miscibility conditions through vaporizing- and/or condensing-gas drive in the region close to the surface may contribute to incremental oil production by vaporization in Set 1. In Set 2, the vaporization is expected to be marginal owing to the weaker convective gas transport. In such, the amount of vaporized oil in

Set 2 may be caused by the mixing of gas and bulk oil outside the plug during the gas/oil displacement in the injection phase.

5.4.2.3. Oil Swelling

Signs of oil swelling are observed during the injection and soaking periods in Sets 1 and 2. As mentioned in the “Total System Compressibility” section, the wet surface during gas injection in Set 1 may be partially caused by oil swelling. However, the surface remains dry during the soaking period. This suggests that oil recovery by the swelling mechanism may be insignificant. In Set 2, signs of oil swelling appear during the injection and soaking phases. They are highlighted by the blue circles on the images for Steps 2 and 3. Because the clearance between the surface and the sight glass is fairly small, the wet areas highlighted by a yellow circle in Set 2-C₁ may be caused by residual oil resulting from non-uniform gas/oil displacement during the injection phase. This residual oil mainly occurs at the interface of the coating layer and surface owing to the weak bonding between the plug and coating layer. Thus, it is called an edge effect. The wet area at the bottom part of the surface in Set 2-C₁/C₂ may indicate signs of an edge effect. The oil swelling observed during the soaking time in Set 2 is in agreement with the results of gas HnP experiments performed on Bakken rocks by Hawthorne et al. (2013). The authors reported that oil swelling was pronounced during the soaking period compared to the gas injection phase.

The results of bulk-phase tests to visualize interactions at the gas/oil interface (Chapter 3) also support oil swelling caused by gas dissolution into the oil. The volume of the oil in oil/C₁ and oil/C₁/C₂ bulk-phase tests expand 8 and 28% after 67 and 60 hours of soaking, respectively. The higher oil swelling by the mixture of C₁/C₂ is attributed to the higher solubility of gas mixture compared to C₁.

5.4.2.4. Gas Expansion

This production mechanism is mainly controlled by the expansion of leaked-off gas during pressure depletion. Comparing oil production on the surfaces at different phases in the HnP process, it can be concluded that gas expansion is the dominant recovery mechanism. However, it is difficult to quantify oil-production volume by the gas expansion using this experimental setup.

5.4.2.5. Final Oil Recovery

Figure 5-8 compares oil RFs measured by weight-balance method for Sets 1 and 2. For the same gas composition, oil recovery in Set 1 is higher than Set 2. For example, RF of Set 1-C₁ is higher than that of Set 2-C₁ by 21.9% (35.86% vs. 29.41%). For the same ΔP_i conditions, adding 30 mol% C₂ to the gas mixture increases oil recovery by 14.44% (from 35.86% to 40.88%) in Set 1 and 21.93% (29.41% to 35.72%) in Set 2, respectively.

The recovery mechanisms responsible for the oil recovery presented in Figure 5-8 include the total system compressibility, vaporization, oil-swelling, and gas expansion. Table 5-5 lists the oil-recovery volume and percentage of contribution of each recovery mechanism in total oil production. The oil RFs are calculated and compared on the basis of the same initial oil volume in all sets. Basis of calculation for each mechanism includes:

- The oil production by total system compressibility is calculated by Eq. 5-1. Since ΔP_i in Set 2 is zero, no oil production caused by compressibility is reported.
- The oil production by vaporization is obtained from GC analysis.
- Because it is difficult to quantify oil production by solely gas expansion or oil swelling, therefore, they are reported as a combined gas-expansion/oil-swelling mechanism. However, oil recovery by gas expansion is significantly higher than that by oil swelling. The amount of leaked-off gas is one of the important factors

affecting the recovery by the gas-expansion mechanism. The oil produced by this mechanism is calculated by subtracting the total oil production from the total system compressibility and vaporization volumes.

The highest percentage of oil production is by a combined gas-expansion/oil-swelling mechanism, followed by total system compressibility, and vaporization. Combined gas expansion/oil swelling accounts for 90.98 to 98.4% of the total production while vaporization is the least contributor with less than 4% of the total recovery in Sets 1 and 2. For the same gas composition, the total oil production in Set 2 is less than that in Set 1 owing to the absence of oil recovery from total system compressibility and a weaker support from the advective flow.

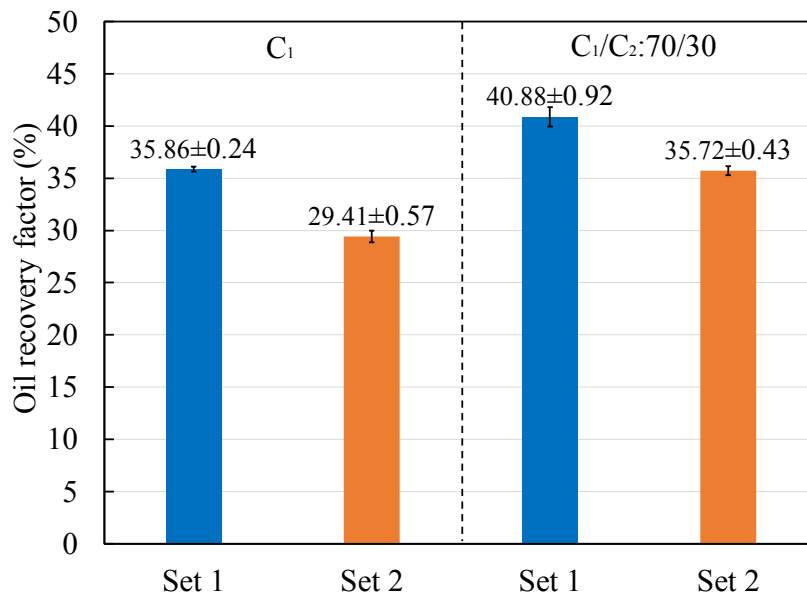


Figure 5–8: Oil RFs from the HnP tests measured by the weight-balance method.

Table 5–5: Oil production by different recovery mechanisms during natural-gas HnP experiments

Set	Injected gas	Total system compressibility		Vaporization		Combined gas expansion/oil swelling		Total oil production (cm ³)
		Volume (cm ³)	% total	Volume (cm ³)	% total	Volume (cm ³)	% total	
1	C ₁	0.06	5.72	0.02	1.63	0.92	92.65	0.99
	C ₁ /C ₂ :70/30	0.06	4.99	0.05	4.03	1.04	90.98	1.14
2	C ₁	0	0	0.01	1.60	0.81	98.40	0.82
	C ₁ /C ₂ :70/30	0	0	0.03	3.00	0.97	97.00	1.00

5.4.3.Oil-Recovery Mechanism during Depressurization Phase

The measured oil recovery (Table 5-6) and images of the surface showing significant oil production during the depressurization phase (Step 4 in Figure 5-6) indicate that gas expansion is the dominant recovery mechanism in the HnP process. The leaked-off gas expands and flows out of the plug, dragging oil along with it, under the induced pressure gradient during the depletion phase.

To determine states of the gas phase in the plug, i.e. free and/or solution gas, during the soaking period, we estimate saturation pressure (P_{sat}) and fractions of free/solution gas in the gas/oil systems using the PR-EOS that was calibrated against the constant-composition-expansion and MMP data. It should be noted that this quantification is to better understand the phase behavior of the gas/oil system before the depressurization and does not reflect the exact thermodynamic conditions in the plug. The density values of C₁ (under P_{set} , P_{f} , and T_{set}) are obtained from the National Institute of Standards and Technology (NIST 2018) chemical webbook. We use the flash calculation and saturation-point prediction modules in PVTsim software (Calsep A/S 2018) to calculate densities of C₁/C₂:70/30 mol% (under P_{set} , P_{f} , and T_{set}) to predict P_{sat} of the gas/oil systems, respectively.

P_{sat} values and fractions of free/solution gas in the leaked-off gas are calculated using the calibrated PR-EOS on the basis of three assumptions: because the gas volume in the cell is relatively high, the concentration of vaporized-oil components is negligible; the changes in oil composition resulting from vaporization are insignificant; and the effects of nanoconfinement on phase behavior calculations is neglected. The mole of produced oil is obtained from the calculated oil RFs. Table 5-6 lists the predicted P_{sat} values for the four gas/oil systems. The molar ratio of gas/oil systems, i.e. leaked-off gas/produced oil, used in the PR-EOS calculations are taken from Table 5-4. The mol% of gas/oil at P_f is estimated by performing flash calculations for the mixtures of leaked-off gas/original oil at respective P_f and T_{set} . Based on the experimental conditions of the HnP tests (P_{set} and $P_f < P_{\text{sat}}$), the leaked-off gas exists in both solution- and free-gas states during the experiments. Two-phase equilibrium data from the flash calculations show a high fraction of free gas (0.61 to 0.74) in the pores at the end of the soaking period.

Figure 5-9a shows pressure-depletion profiles of all the tests and images of gas/oil production during the depressurization phase in Set 1-C₁. It takes approximately 2 hours (with an average pressure-depletion rate of 1.17 bar/min) to depressurize the gas/oil systems in Sets 1 and 2 from P_f to P_{atm} . Images of the surface in Set 1-C₁ test correspond to the onset of the depressurization, observing the early oil droplets on the surface, and significant production of gas and oil. The pressures at which the early oil droplets are observed in Sets 1 and 2 are approximately 124 and 117 bar, respectively. Figure 5-9b shows the comingled flow of oil and gas driven by the gas-expansion mechanism in Set 2-C₁/C₂ test. The magnified image of the surface shows the evolution of gas bubbles at $t = 168.2$ hours and $P = 55.85$ bar. The gas bubbles evolve from the pores and flow upward (red arrows), dragging the oil upward before draining downward by gravity (blue arrow on the unmagnified surface). Gas bubbles coalesce and form bigger ones (yellow arrows) while moving upward.

Table 5–6: P_{sat} estimation by the calibrated PR-EOS and fractions of free/solution gas in the leaked-off gas at the end of the soaking period. The fraction of free gas is calculated by taking the ratio of mol% of gas at P_f and the mol% of leaked-off gas, for instance, it equals to $58.97/80.25 = 0.73$ in Set 1-C₁ test

Set	Injected gas	Mol% of leaked-off gas/original oil	P_{sat} (bar)	Mol% of gas/oil at P_f	Leaked-off gas at the end of soaking (fraction)	
					Free	Solution
1	C ₁	80.25/19.75	281.29	58.97/41.03	0.73	0.27
	C ₁ /C ₂ :70/30	90.30/9.70	228.95	67.02/32.98	0.74	0.26
2	C ₁	73.49/26.51	238.38	44.40/55.60	0.61	0.39
	C ₁ /C ₂ :70/30	89.62/10.38	226.83	64.73/35.27	0.72	0.28

During the depressurization phase, the solution gas evolves and merges with free gas, increasing the overall gas saturation. S_{gc} refers to the minimum gas saturation required for forming a continuous gas phase that can flow independently. When the pressure reduces to the point corresponding to S_{gc} , for example, 124.2 bar in Set 1-C₁ test, gas starts flowing towards the surface. One might notice a time delay of 0.46 hours for a pressure drop of 11.83 bar (from 136.03 to 124.2 bar in Set 1-C₁ test) and for gas/oil production to be observed on the surface. This production delay might be attributed to the process of solution gas evolvement and coalescence of solution/free gas caused by reduced the cell's pressure. The observed oil production on the surface in Step 4 of Fig. 6 suggests that the performance of oil recovery by gas expansion may depend on ΔP_i and the amount of leaked-off gas during injection and soaking periods. It is worth noting that oil expansion also contributes to the oil recovery during depressurization. However, this oil recovery is negligible compared to gas expansion owing to the minimal change in the compressibility of dead oil. In a modeling study of produced-fluid composition redistribution during pressure depletion in tight oil reservoirs, Baek and Akkutlu (2019a and 2019b) reported that dissolved-gas expansion is an important recovery mechanism

and pronounced in large pores (>10 nm). Because the evolved gas is observed at several locations on the surface, the more the surface area in contact with the gas, the faster the oil can be recovered. Jacobs (2019) and Rassenfoss (2017) reviewed field pilot data and suggested that the performance of gas HnP EOR in shales is controlled by the gas/rock contact area and the injection pressure.

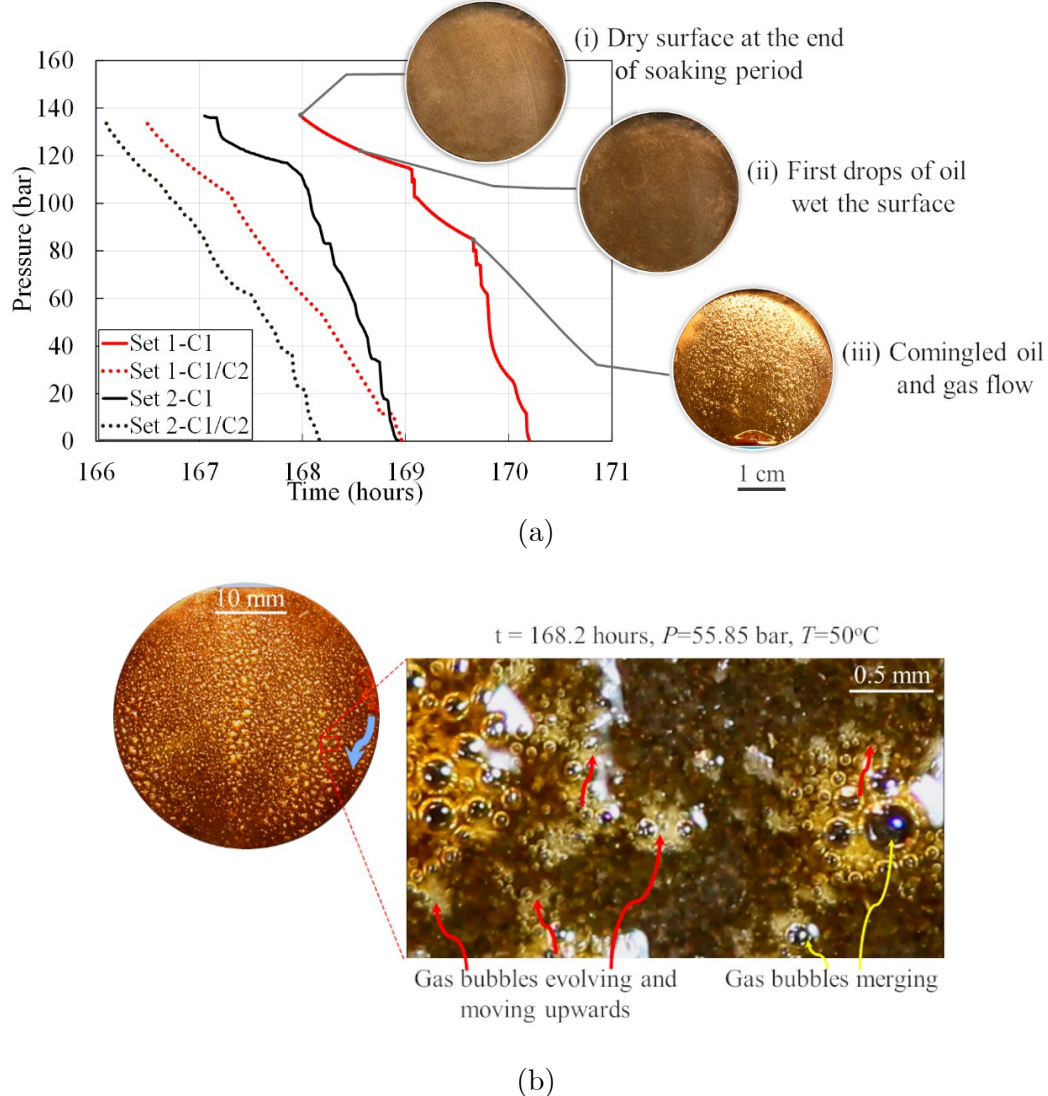


Figure 5-9: (a) pressure-decline profiles and the images of the surface in Set 1-C₁ test, and (b) the evolved gas bubbles, merged (yellow arrows), and moved upwards (red arrows) and the produced oil being draining downward caused by gravity (blue arrow) observed on the surface during the depressurization phase of Set 2-C₁/C₂ test.

5.5. Limitations

We present the following limitations:

- Silicone coating may not fully function under high-pressure and high-temperature conditions during the HnP experiments. Part of the coating layer, especially at the interface of the coating layer and plug's surface, may be soluble in oil at T_{set} in Set 2. This may cause nonuniform gas/oil displacement during the gas-injection and soaking phases, and production during the depressurization.
- The interactions of injected gas and the oil during the injection and soaking phases may strip out some intermediates and heavy ends from the oil. The residual-oil components with higher molecular weight may not be completely removed by the drying process performed after each experiment.
- It is difficult to separately quantify oil recovery by the gas expansion and oil swelling by this experimental setup.
- Because of the nonuniform gas/oil displacement, there are still traces of oil left in the cell after the injection phase in Set 2. This amount of oil may vaporize and affect the GC analysis as well as recovery by the vaporization mechanism.
- The experimental database is limited because only one plug is used in this study. Therefore, future work is needed to solidify the findings related to gas-transport and oil-recovery mechanisms using plugs with a range of porosity and permeability. Additional works to evaluate oil recovery under different pressure-depletion rates and injection pressures, that is, above the MMP of the oil and gas mixture ($C_1/C_2:70/30 \text{ mol\%}$), are useful for field-pilot design.

5.6. Summary

In this chapter, we conducted natural-gas HnP experiments under core-plug conditions to understand the controlling mechanisms of oil recovery. The results indicated that it is technically feasible to apply the natural-gas HnP process on Montney ultratight rocks.

We found that advective-dominated transport is the mechanism responsible for the transport of gas into the plug at the early times of the soaking period. When the soaking progresses, the dominant mechanism is molecular diffusion. The advective flow caused by ΔP_i during gas injection and soaking leads to improved gas transport into the plug. Overall, gas expansion is the dominant mechanism, followed by total system compressibility, oil swelling, and vaporization. During the ‘puff’ period, the expansion and flow of diffused gas drag the oil along its flowpaths, resulting in a significant flow of oil and gas observed on the surface of the plug. The enrichment of injected gas by C₂ (30 mol%) leads to an increase of 131 to 210% in mass transport of gas into the plug as well as oil recovery.

Finally, the findings presented in this chapter provide a reasonable basis for operators to improve understanding of gas-transport and recovery mechanisms involved in the gas HnP process in tight-oil reservoirs and field-pilot designs.

Chapter 6 : Quantification of Gas-Transport Mechanisms during Soaking Period of The Natural-Gas HnP Process

6.1.Introduction

This chapter quantitatively evaluates gas-transport mechanisms during a natural-gas HnP cycle under core-plug conditions. First, we estimate bulk-phase and effective diffusion coefficient (D and D_{eff}) using analytical solutions published in the literature. Second, we model and calculate N_{Pe} to quantify possible mechanisms that can be responsible for gas transport into the plug during the soaking period.

6.2.Method

6.2.1.Diffusion Coefficients in Bulk-Phase and Core-Plug Conditions

The pressure-decay technique has been widely used to quantify diffusion of gas into bulk oil. In this study, the pressure-decline data are obtained from the visualization tests presented in Sections 3.4.4 and 5.4.1 of Chapters 3 and 5, respectively. It should be noted that the experimental conditions of the visualization and HnP tests are identical ($P_{\text{set}} = 137.90$ bar and $T_{\text{set}} = 50^{\circ}\text{C}$). In the pressure-decay technique, the pressure-decline data are divided into early-time and late-time regions. According to Pacheco and Hejazi (2015), the early-time regime begins when the gas molecules start going into bulk oil, while the late-time regime starts after the gas molecules reach the bottom of the cell. The early-time and the tail of late-time data (i.e., pressure in the cell approaches equilibrium pressure) are usually neglected in D calculations (Pacheco and Hejazi 2015, Sheikha et al. 2006, and Zhang et al. 2000). We adopt an analytical solution that uses late-time data to graphically predict D (Zhang et al. 2000). This graphical approach is selected on the basis of having a similar experimental setup and procedure with the

visualization tests for oil/C₁ and oil/C₁/C₂ systems presented in Chapter 3. The final equation used to compute D is

$$\ln[P(t) - P_{\text{eq}}] = -\frac{\pi^2 D}{4z_o^2} t + \ln \left[\frac{8Bz_o x_{1,\text{eq}(P)}}{\pi^2} \right] \quad (6-1)$$

where $P(t)$ and P_{eq} are measured and equilibrium pressure, respectively; D , z_o , t and $x_{1,\text{eq}(P)}$ are diffusion coefficient, the height of the oil column in the cell, experimental time, and gas concentration at gas/oil interface, respectively. B is a constant defined by $\frac{Z_g RT}{h}$; h , Z_g , R , T are the height of the gas column in the cell, compressibility factor, gas constant, and temperature, respectively.

To apply the above graphical method, the first step is to divide the pressure-decline data of two visualization tests into early-time and late-time regions by the k -plane clustering method (Bradley and Mangasarian 2000). Detailed information on k -plane clustering method can be found in Appendix B. By plotting $\ln(P(t) - P_{\text{eq}})$ vs. time following Eq. 6-1, a straight-line fit of the late-time data (excluded the tail part) can be obtained. From the slope of the resulting regressed line, D can be calculated.

$$D = -\frac{4z_o^2 \times k_1}{\pi^2} \quad (6-2)$$

where z_o and k_1 are the height of the oil column in the cell and slopes of the regressed line in Eq. 6-1.

In porous media, the diffusion process is much slower than in bulk fluid owing to the hindrance of the rock matrix. Fried et al. (1971) and Ullman and Aller (1982) suggested the following equation to estimate the effective diffusion coefficient (D_{eff}), taking into account tortuosity (τ) of the formation.

$$D_{\text{eff}} = \frac{D}{\tau^2} \quad (6-3)$$

Shen and Chen (2007), and Grathwohl (2012) studied impacts of tortuosity on the D_{eff} and the authors proposed an empirical equation to relate tortuosity to the porosity (ϕ) and the formation resistivity (F) as

$$\tau^2 = (F \times \phi)^n \quad (6-4)$$

where n is an adjustable empirical parameter.

According to Archie's law (Archie 1942), the formation resistivity is given by $F = \frac{a}{\phi^m}$. Substituting F by Archie's law to Eq. 6-4 and resulting τ to Eq. 6-3 give the D_{eff} by

$$D_{\text{eff}} = \frac{D}{(a \times \phi^{1-m})^n} \quad (6-5)$$

where a and m are tortuosity constant and cementation factor in the porous media, respectively.

The parameters, a , n and m , are lithology-dependent. According to Boudreau (1996), Shen and Chen (2007), Alavian (2011), and Li et al. (2018), we assume that $a = n = 1$ and $m = 2$. Therefore, the D_{eff} can be estimated as

$$D_{\text{eff}} = \phi \times D \quad (6-6)$$

6.2.2. Quantifying Gas-Transport Mechanisms during Soaking Period

To evaluate the relative importance of advection vs. diffusion during the soaking period, we model and calculate the dimensionless N_{Pe} for the soaking periods of HnP

tests. To calculate the N_{Pe} using Eq. 2-9, we need to determine the Darcy velocity and D_{eff} . The D_{eff} is calculated using Eq. 6-6.

The Darcy velocity, u , is defined as the volume of fluid that passes through a unit area of the material in unit time.

$$u = -\frac{k}{\mu} \times \frac{\partial p}{\partial x} \quad (6-7)$$

Also, the continuity equation (Charbeneau 2006; Bear 2013; Birdsell et al. 2018) for 1-D mass transport along the core plug can be written as

$$\frac{\partial p}{\partial t} = \frac{\partial (up)}{\partial x} \quad (6-8)$$

By expanding the second term of Eq. 6.8, we have

$$\frac{\partial p}{\partial t} = u \frac{\partial p}{\partial x} + p \frac{\partial u}{\partial x} \quad (6-9)$$

As an approximation, we assume that u is constant along the plug. This results in $\frac{\partial u}{\partial x} = 0$. Therefore, Eq. 6-9 can be written as

$$\frac{\partial p}{\partial t} = u \frac{\partial p}{\partial x} \quad (6-10)$$

where $\frac{\partial p}{\partial t}$ is calculated for the two pressure-decline regions, i.e., early and late times.

From Eq. 6-10, we have established the relationship between pressure drop over time and along the plug. Rearrange Eq. 6-7, the pressure drop along the plug is given by

$$\frac{\partial p}{\partial x} = \frac{-u \times \mu}{k} \quad (6-11)$$

By substituting $\frac{\partial p}{\partial x}$ in Eq. 6-11 to Eq. 6-10 we have:

$$\frac{\partial p}{\partial t} = u \frac{-u \times \mu}{k} \quad (6-12)$$

$$\text{or } u = \sqrt{-\frac{k}{\mu} \times \frac{\partial p}{\partial t}} \quad (6-13)$$

Finally, by combining Eqs. 2-9, 6-6, and 6-13, we arrive at the following equation for N_{Pe}

$$N_{Pe} = \frac{\sqrt{-\frac{k}{\mu} \times \frac{\partial p}{\partial t}} \times L}{\phi \times D} \quad (6-14)$$

6.3. Results and Discussions

6.3.1. Estimation of D and D_{eff}

This subsection presents results of D and D_{eff} calculations for bulk-phase and HnP tests at T_{set} . The pressure-decline data of two bulk-phase tests ($\ln(P(t) - P_{eq})$ vs. time) are divided into early-time and late-time regions using k -plane clustering method as shown in Figure 6-1. The slopes (k_1) of the two regressed lines (highlighted in yellow) are -0.0317 1/hour and -0.0438 1/hour for oil/C₁ and oil/C₁/C₂ tests, respectively. Table 6-1 lists the results of D values calculated for two visualization tests (oil/C₁ and oil/C₁/C₂ system). It should be noted that only one D value is derived from the diffusion-dominated region (yellow trendline) of the late-time data for each test.

The estimated D using Eq. 6-2 are 5×10^{-9} m²/s and 6.5×10^{-9} m²/s for oil/C₁ and oil/C₁/C₂ tests, respectively. The addition of 30 mol% C₂ to the injected gas leads to a 30% increase in gas diffusivity into the oil phase. Table 6-1 compares D values obtained

in this work with reported D using graphical and numerical approaches. The results of this work are in agreement with published literature (Lou et al. 2020 and Li et al. 2020).

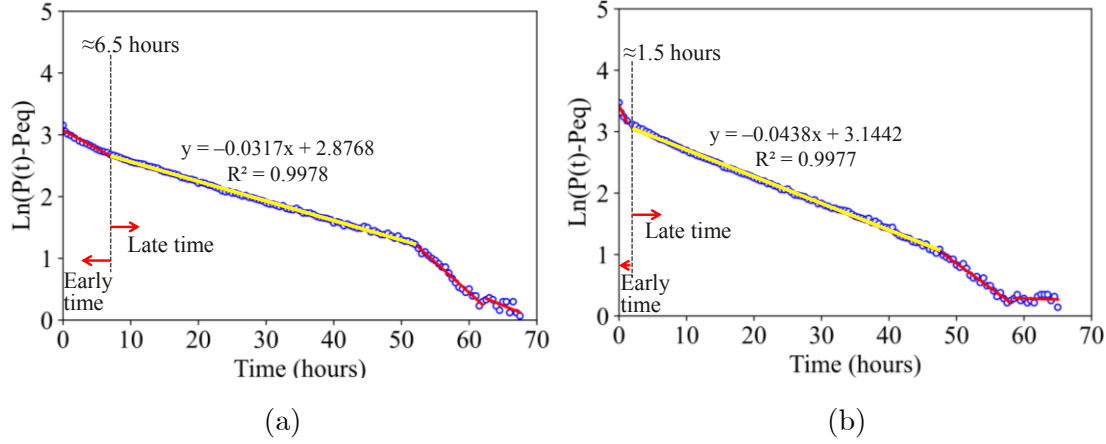


Figure 6-1: Pressure-decline regions classification by k -plane clustering method: (a) Oil/C₁, and (b) Oil/C₁/C₂ (C₁/C₂:70/30 mol%).

Table 6-1: Comparison of calculated diffusion coefficient calculated in this study with the literature

Method	Fluid System	Temperature (°C)	Pressure (bar)	D (m ² /s)	Reference
Graphical approach	C ₁ /Montney oil	50	137.90	5×10 ⁻⁹	This work
Graphical approach	C ₁ /C ₂ :70/30 mol% and Montney oil	50	137.90	6.5×10 ⁻⁹	This work
Graphical approach	C ₁ /Bakken oil	21	137.90	4.35×10 ⁻⁹	Lou et al. (2020)
Numerical model	C ₁ /Bakken oil	21	137.90	3.80×10 ⁻⁹	Lou et al. (2020)
Numerical model	C ₁ /Bakken oil	109.8	90	3×10 ⁻⁹	Li et al. (2020)
Numerical model	C ₂ /Bakken oil	109.8	90	8.2×10 ⁻⁹	Li et al. (2020)

Table 6-2 presents the estimated D_{eff} values using Eq. 6-6 and D_{eff} reported in the literature. The calculated D_{eff} values for HnP tests using C₁ and mixture of C₁/C₂ (70:30 mol%) are $1.75 \times 10^{-10} \text{ m}^2/\text{s}$ and $2.28 \times 10^{-10} \text{ m}^2/\text{s}$, respectively. The D_{eff} values are higher at the higher injection pressure as reported by Perez and Devegowda (2020). Overall, the estimated D_{eff} values in this work are consistent with findings reported in the literature (Lou et al. 2020; Perez and Devegowda 2020).

Table 6–2: Comparison of the D_{eff} calculated in this study with the literature

Rock Sample	Porosity (%) bulk volume)	Fluid System	Pressure (bar) and Temperature (°C)	D_{eff} (m^2/s)	Reference
Montney siltstone	3.5	C ₁ /Montney oil	137.9 and 50 137.9 and 50 Montney oil	1.75×10^{-10} 2.28×10^{-10}	This work
Montney siltstone	3.5	C ₁ /C ₂ :70/30 mol% and Montney oil	137.9 and 50	2.28×10^{-10}	This work
Indiana limestone	15-18	C ₁ /Bakken oil	137.9 and 21	1.50×10^{-10}	Lou et al. (2020)
Bakken shale	8	C ₁ /Bakken oil	137.9 and 21	2.00×10^{-11}	Lou et al. (2020)
Marine shales	-	C ₁ /C ₂ :72/28 mol% and black oil	303 and 82	4.50×10^{-10}	Perez and Devegowda (2020)

6.3.2. Péclet Number Analysis

We model and calculate N_{Pe} of the four HnP tests to evaluate contributions of advection and diffusion during the soaking period. First, we divide the pressure-decline periods of HnP tests into early-time and late-time periods by the k -plane clustering method as shown in Figure 6-2. Second, we calculate values of average pressure drop,

Darcy velocity (using Eq. 6-13), and N_{Pe} (using Eq. 6-14) for the early- and late-time regions.

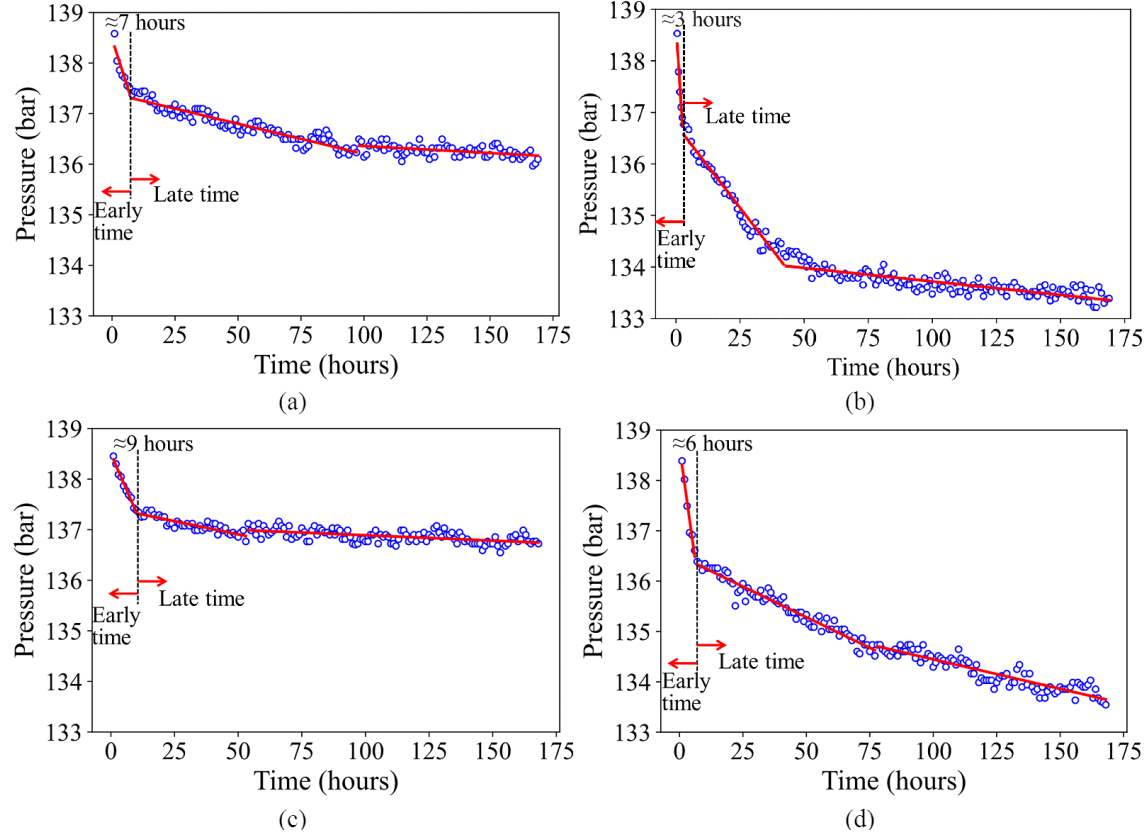


Figure 6–2: Pressure-decline regions classification by k -plane clustering method: (a) Set 1-C₁, (b) Set 1-C₁/C₂, (c) Set 2-C₁, and (d) Set 2-C₁/C₂.

Table 6-3 lists the calculated values of average pressure drop, Darcy velocity, and N_{Pe} for the four HnP tests at early and late times. At the early times, N_{Pe} ranges from 1.82 to 3.03, suggesting that both advective and diffusive transports coexist in the system. Nevertheless, N_{Pe} of Set 1 is 12 to 15% higher (stronger advection) than Set 2. At the late times, N_{Pe} ranges from 0.26 to 0.62, indicating the dominance of molecular diffusion. The N_{Pe} changes significantly in the region close to the boundary of early- and late-time periods as shown in Figure 6-3. The advective flow is gradually weaker with time in the

late-time region. Although the tests in Set 2 are designed with minimal ΔP_i , pressure changes during the gas/oil displacement (in the injection phase) could be the cause of higher than expected advection in the early times.

Table 6-4 summarizes the N_{Pe} values calculated for the diffusion-dominated region in this work and those by Hoteit and Firoozabadi (2009) and Mohebbinia and Wong (2017). Mohebbinia and Wong (2017) showed that the molecular diffusion dominates oil recovery with $N_{Pe} < 0.2$. The authors also reported that there is a transition zone with $N_{Pe} = 0.2$ to 5, where diffusion compete with advection. Moreover, Perez and Devegowda (2020) performed a molecular dynamic simulation to investigate gas-transport mechanisms during the soaking period. The authors reported that the advection dominates at the early time and molecular diffusion is the dominant mechanism when the soaking progress.

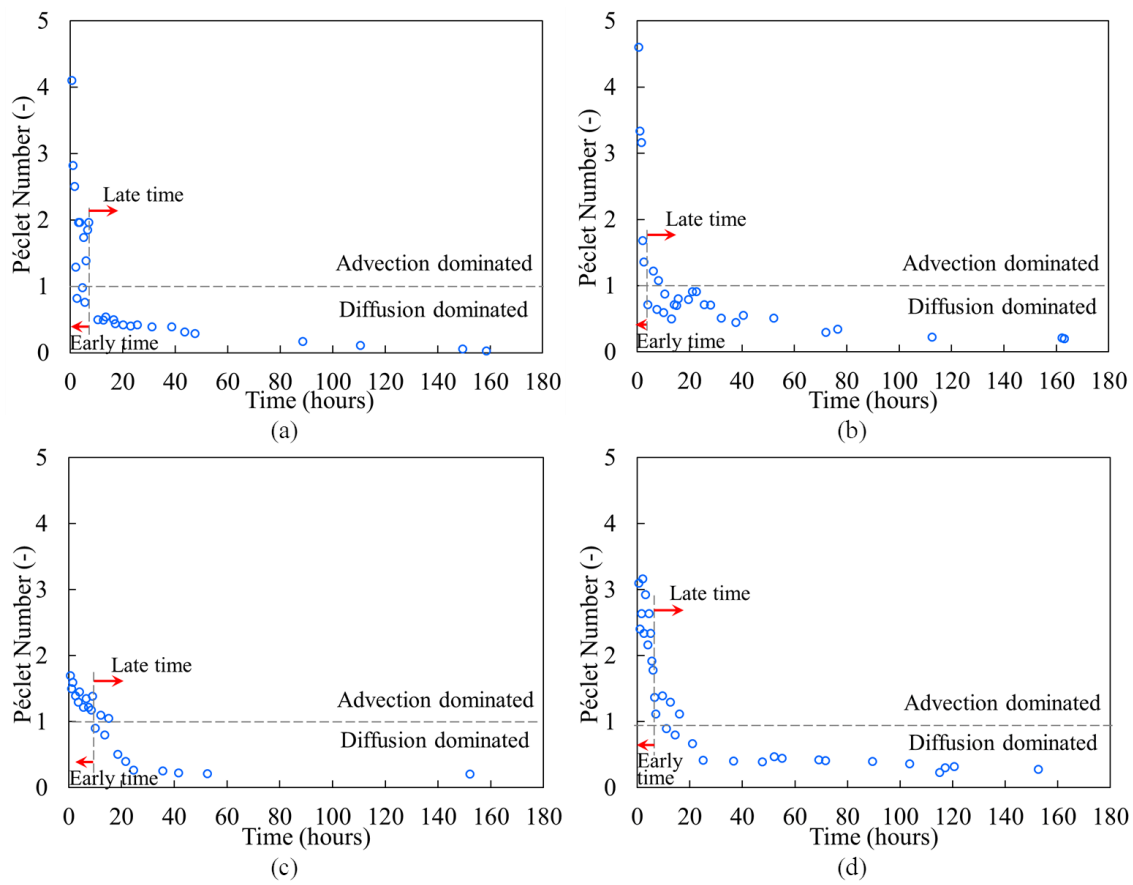


Figure 6–3: N_{Pe} profiles during soaking period: (a) Set 1-C₁, (b) Set 1-C₁/C₂, (c) Set 2-C₁, and (d) Set 2-C₁/C₂.

Table 6-3: N_{Pe} calculations for 1-D transport of natural gas into the oil-saturated plug. The values of porosity, permeability, oil viscosity, and core-plug length are the same for all HnP tests

Parameter Description	Value				
	Set 1-C ₁	Set 1-C ₁ /C ₂	Set 2-C ₁	Set 2-C ₁ /C ₂	
Porosity, ϕ (-)	3.5×10^{-2}	-	-	-	
Permeability, k (m ²)	5.92×10^{-20}	-	-	-	
Oil viscosity, μ (Pa·s)	9×10^{-3}	-	-	-	
Core-plug length, L (m)	6.3×10^{-2}	-	-	-	
Effective diffusion coefficient, D_{eff} (m ² /s)	1.75×10^{-10}	2.28×10^{-10}	1.75×10^{-10}	2.28×10^{-10}	
Péclet Number Calculations					
Early times	Pressure drop, $\frac{\partial p}{\partial t}$ (Pa/s)	-3.89	-18.20	-2.93	-14.45
	Darcy velocity, u (m/s)	5.05×10^{-9}	1.09×10^{-8}	4.39×10^{-9}	9.75×10^{-9}
	Péclet Number, N_{Pe} (-)	1.82	3.03	1.58	2.70
Late times	Pressure drop, $\frac{\partial p}{\partial t}$ (Pa/s)	-0.14	-0.76	-0.08	-0.30
	Darcy velocity, u (m/s)	9.46×10^{-10}	2.24×10^{-9}	7.25×10^{-10}	1.40×10^{-9}
	Péclet Number, N_{Pe} (-)	0.34	0.62	0.26	0.39

Table 6–4: Comparison of the calculated N_{Pe} for diffusion-dominated transport in this work with the literature

Rock Sample	Porosity (%) bulk volume)	Fluid System	Pressure (bar) and Temperature (°C)	N_{Pe}	Reference
Montney Siltstone	3.5	C ₁ /Montney oil	137.9 and 50	0.26- 0.34	This work
North Sea Chalk	44	CO ₂ /black oil	300 and 130	<0.2	Mohebbinia and Wong (2017)
Fractured Media	20	C ₁ /black oil	320 and 93	<0.1	Hoteit and Firoozabadi (2009)

6.4.Limitations

We present the following limitations:

- The estimation of D_{eff} values using Eq. 6-6 is an approximate solution without calibrating pressure-decline and oil recovery data in the HnP tests.
- The use of the average D_{eff} value for the whole shut-in period of each HnP test is an approximate solution for N_{Pe} analysis purposes. In practice, D_{eff} in the early time is higher than late time, owing to the presence of strong advective flow.

6.5.Summary

In this chapter, we quantified gas-transport mechanisms during a natural-gas HnP cycle under bulk-phase and core-plug conditions to understand the controlling mechanisms of oil recovery.

We found that advective-dominated transport is the mechanism responsible for the transport of gas into the plug at early times of the soaking period ($N_{Pe} = 1.58$ to 3.03). When the soaking progresses, N_{Pe} ranges from 0.26 to 0.62 , indicating the dominance of molecular diffusion. The advective flow caused by ΔP_i during gas injection and soaking leads to improved gas transport into the plug. The addition of C₂ (30 mol%) to the injected gas improves gas diffusivity into the oil in both bulk-phase and HnP tests.

Chapter 7 : Evaluation of Aqueous Phase Trapping and Remediation Methods

7.1. Introduction

In this chapter, we investigate the change in k_o^{eff} caused by FF leakoff after HF of a tight-oil reservoir. Here, we use rock and fluid samples from the Midale tight-carbonate reservoir to investigate the effects of leakoff, shut-in, and surfactants on k_o^{eff} after the flowback process under reservoir conditions ($P = 172$ bar and $T = 60^\circ\text{C}$).

We perform a series of coreflooding tests on three plugs with different permeabilities to experimentally simulate FF-leakoff/flowback processes. We soaked the plugs in oil to restore reservoir conditions and measured the baseline values of k_o^{eff} . We measured k_o^{eff} using Darcy's law, and used the measured values of pressure drop across the plugs to investigate the effects of leakoff-fluid properties (FF with surfactants and fresh water), shut-in periods (3 and 14 days), and plugs' properties on regained permeability. We also measure IFT between oil and fresh water/FF (before the leakoff and after the flowback) to understand how IFT reduction affects k_o^{eff} . In addition, we investigate the possible effects of wettability alteration on k_o^{eff} by comparing brine/oil contact angles (CAs) measured on the surface of the plugs before leakoff and after flowback processes.

7.2. Materials

7.2.1. Core Samples

Core samples were collected from the Midale tight carbonate formation in southeastern Saskatchewan. This formation is subdivided into two geological units: an upper dolostone unit named Marly (1 to 11m thick) and a lower limestone unit named Vuggy (10 to 22m thick) (Burrowes 2001). Burrowes (2001) observed a system of natural

fractures, both open and cemented, in the Vuggy Unit. Figure 7-1 shows the depositional sequences and the two geological units of the Midale tight carbonate formation.

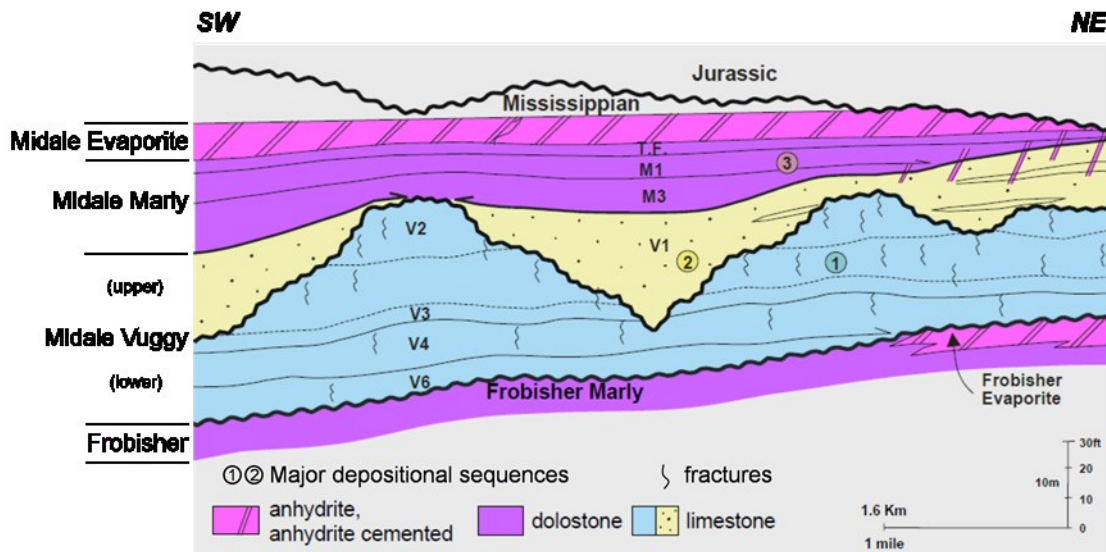


Figure 7-1: Depositional sequences and geological units of the Midale tight carbonate formation (Burrowes, 2001). T.F. represents Three Fingers transitional unit. Circled numbers 1 and 2 show major depositional sequences, while circled number 3 shows a low-permeability zone separating M1 and M3 layers. Layers V2 to V6 in the Lower Vuggy are identified for the purposes of reservoir modeling.

After coring operation, the whole cores were cut into 1-m sleeves, slabbed longitudinally, and stored in wooden boxes at the core facility. No preservation technique was applied to the slabbed cores. Cylindrical plugs were cut from the slabbed cores for routine core analysis. The plugs were oriented parallel to the bedding plane. The plugs went through a cleaning process using a Soxhlet system before being trimmed at two ends to achieve a dimension of approximately 2.5 cm in diameter and 5 cm in length. The end pieces were used for thin-section analyses. Three plugs, shown in Figure 7-2, with a porosity range of 0.05 to 0.26 and an air-permeability range of 0.09 to 5.28 mD

were selected for this study. Table 7-1 lists petrophysical properties of the three plugs. Plug C with the minimum permeability has the maximum S_{wirr} .

The X-ray-diffraction analyses were performed on broken pieces collected during core-plug cutting, assuming that their mineralogy is similar to that of the plugs. The rock samples were grounded and filtered to have fine powders for the X-ray-diffraction tests. Table 7-2 lists the mineralogy of Plugs A and C from the Marly and Vuggy units, respectively. The mineralogy data are only available for Plugs A and C. The results show that calcite (52 to 59 wt%) and dolomite (34 to 39 wt%) are the dominant minerals. Small quantities of detrital clay (trace amounts to 1% of the whole rock weight) are present in the plugs.



Figure 7-2: Images of the plugs (a) A, (b) B, and (c) C.

Table 7–1: Petrophysical properties of the plugs from Marly (A and B) and Vuggy (C) units

Plug	Measured Depth (m)	Air permeability, k_{air} (mD)	Porosity, helium (fraction)	S_{wirr} (fraction)	Grain density (kg/m ³)	Diameter (cm)	Length (cm)
A	1549.60	0.13	0.11	0.37	2.75	2.46	5.08
B	1551.58	5.28	0.26	0.33	2.78	2.46	5.08
C	1553.87	0.09	0.05	0.48	2.75	2.46	5.08

Table 7–2: Mineralogy of plugs A and C obtained from XRD analysis

Mineral	weight %	
	A	C
Quartz	4	3
K-Feldspar	2	1
Calcite	52	59
Dolomite	39	34
Halite	2	1
Siderite	0	Trace
Pyrite	1	1
Total Clay	Trace	1
Total	100	100
Clay Mineral	Relative Clay %	
Illite / Smectite	15	6
Chlorite/Smectite	17	14
Illite / Mica	47	48
Kaolinite	10	17
Chlorite	11	15
Total	100	100

Thin-section analysis is essential to understand the complex pore structure of tight-carbonate rocks. The thin-section samples were taken from both ends of the plugs when trimming the plugs to the exact dimensions for testing. The thin sections were prepared by first filling the samples with blue-dyed epoxy to highlight pore spaces. Each sample was then mounted on a glass slide and cut to an approximate thickness of 30 mm. Finally, mineral staining was performed for rapid and accurate identification of some common carbonate minerals (e.g., calcite, dolomite, and K-feldspar). Figure 7-3 shows thin-section images of the plugs. The porosity type for Plugs A and B are interparticle and intraparticle that is partially occluded by dolomite cement, while the porosity type for Plug C is interparticle, intraparticle, and microfractures. Microfractures partially filled with calcite cement are only visible in Plug C. It should be noted that microfractures on a thin section could be natural or induced during coring operation and handling. According to Lucia (2007) and Derkani et al. (2018), carbonate rocks have interparticle and vuggy pores that are usually oil-wet.

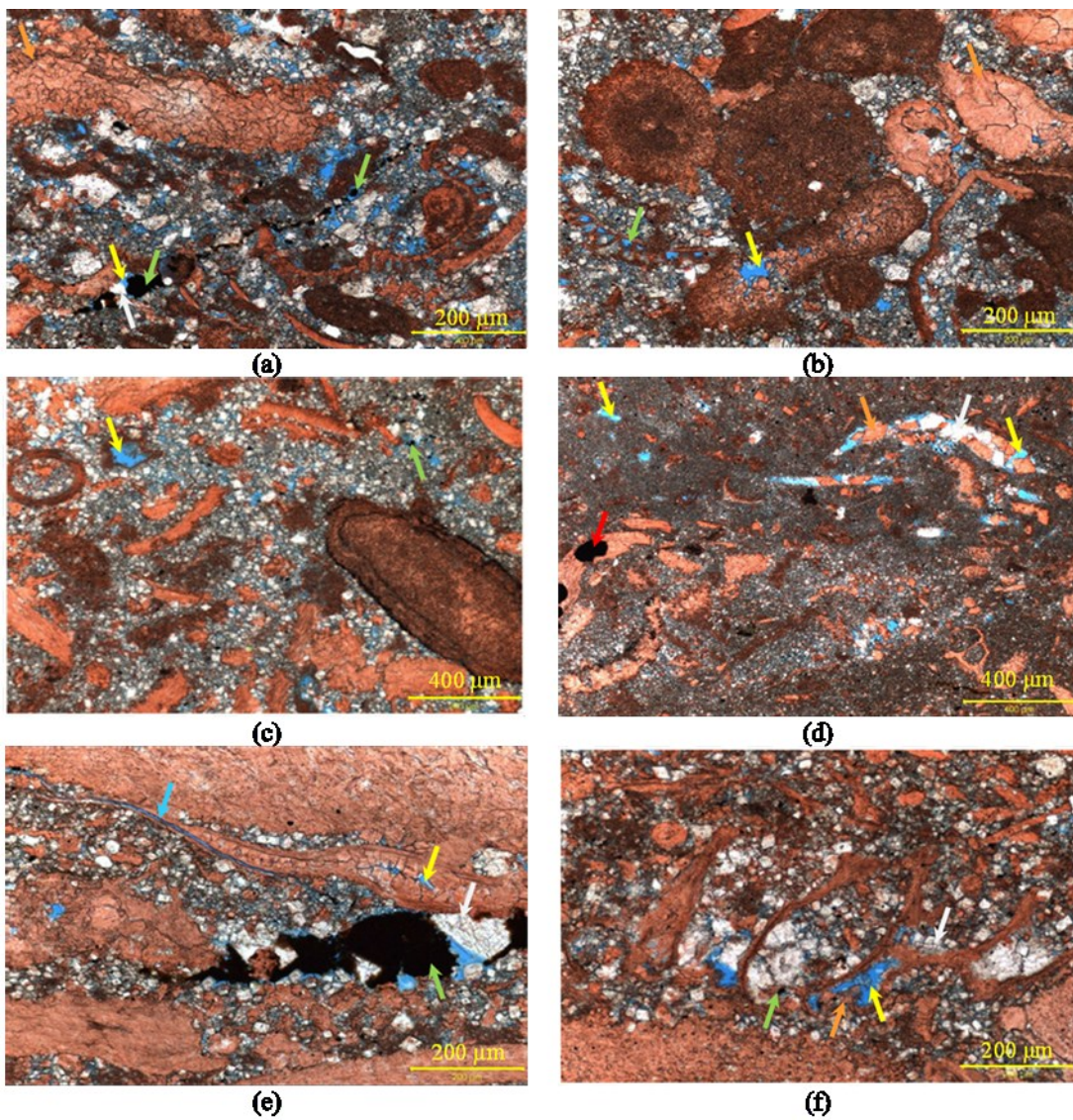


Figure 7-3: Thin-section images taken at 125x magnification: (a), (b) for plug A with interparticle porosity (yellow arrows) partially occluded by residual hydrocarbon (green arrows), intraparticle porosity partially occluded by dolomite cements (white arrows), and calcite cements (orange arrows); (c), (d) for plug B with interparticle and intraparticle porosity that is partially occluded by dolomite cements, and pyrite nodules (red arrow); and (e), (f) for plug C with a micro-fracture (blue arrow) partially filled with calcite cement, interparticle and intraparticle porosity partially occluded by residual hydrocarbon and dolomite cements.

Figure 7-4 shows the pore-throat-size distribution of the plugs obtained by mercury-injection capillary pressure (MICP) analysis. Plugs A and B have mainly one pore system (interparticle) with median pore-throat sizes of 0.36 and 0.99 mm, respectively. According to Nelson (2009), pore-throat sizes of petroleum reservoirs are divided into three main categories: greater than 2 mm in conventional reservoirs, 0.03 to 2 mm in tight reservoirs, and 0.005 to 0.1 mm in shales. Figure 7-4c shows two distinct pore networks for Plug C, consistent with Figure 7-3e showing interparticle pores and microfractures. Micropores (mainly interparticle porosity) and meso and macropores (mainly fractured porosity) account for approximately 55 and 45% of the cumulative pore space, respectively. The measured values of low air permeability (0.09 mD) and high S_{wirr} (0.48) are consistent with the wide pore-throat-size distribution of Plug C. Baker et al. (2015) reported that low permeability and high residual saturations in vuggy reservoirs are attributed to the high ratio of the pore diameter to the pore-throat size and poor connectivity within the pore structure.

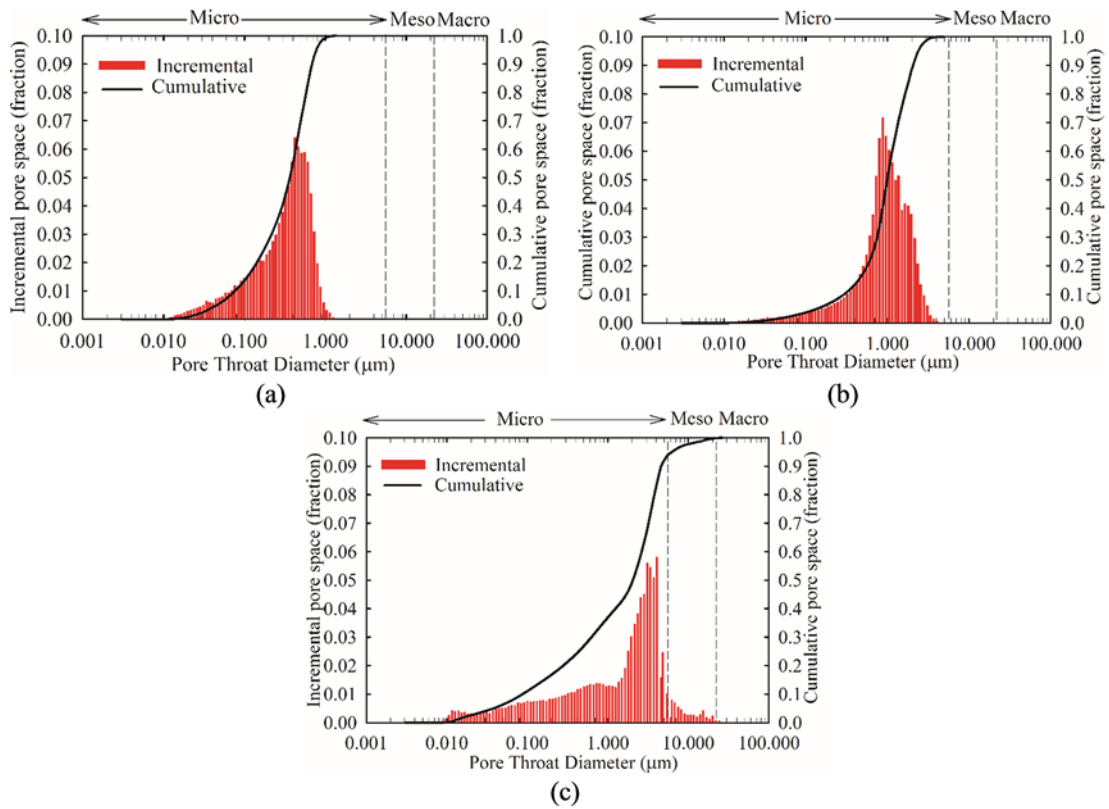


Figure 7-4: Pore-throat-size distributions from MICP data of plugs (a) A, (b) B, and (c).

7.2.2. Fluid Samples

Dead oil and brine samples are from a production well drilled in the Midale tight carbonate reservoir. The brine salinity is 300 000 mg/L. The composition of crosslinked gel FF used in this study is listed in Table 7-3.

Table 7–3: Composition of the cross-linked gel fracturing fluid

No.	Components	Concentration in	Ingredient Name
		Fracturing Fluid (weight %)	
1	Carrier fluid	95.066	Freshwater
2	Proppant	4.339	Crystalline Silica (Quartz)
3	Pre-treat	0.053	Dibenzylidene Polyol Acetal
4	Breaker	0.001	Ammonium Persulphate
5	Clay Control	0.086	Choline Chloride
6	Friction	0.042	High molecular weight anionic
7	Gelling Agent	0.208	Guar, Distillates hydrotreated light,
8	Scale Inhibitor	0.033	Organophosphonate
9	Nonionic Surfactants	0.172	Polyoxyethylenes, d-Limonene, and Alcohol Polyoxyethylene Ether

Table 7-4 lists the physical properties of the crude oil, brine, and FF. The detailed composition of the reservoir brine and physical properties of the nonionic surfactants are presented in Appendix C. The surfactants compatibility tests with the formation brine were conducted by Element Technical Services to avoid formation damage. Surface-tension and density values are measured using a tensiometer and densitometer, respectively. The accuracy of the instrument is $\pm 0.01 \text{ kg/m}^3$ for density and $\pm 0.01 \text{ mN/m}$ for surface tension. The viscosity is measured at the reservoir temperature (60°C). The temperature during the viscosity measurement is maintained by a heating circulator with an accuracy of $\pm 0.03^\circ\text{C}$.

Table 7–4: Physical properties of Midale crude oil, brine, and fracturing fluid

Properties	Crude oil	Brine	FF
Viscosity at 60°C (mPa·s)	2.620±0.026	0.750±0.007	1.540±0.015
Density at 22°C (g/cm ³)	0.83±0.003	1.19±0.001	0.99±0.003
Surface tension (mN/m)	26.73±0.06	67.15±0.18	31.49±0.52

7.3. Method

We conducted a laboratory study to simulate leakoff and flowback processes, and to investigate the effects of shut-in time and properties of the FF and plugs on regained permeability after the flowback process.

7.3.1. Coreflooding Tests

We conducted coreflooding tests on oil-saturated plugs at reservoir temperature (60°C) to simulate two-phase flow during FF-leakoff/flowback processes. Figure 7-5 schematically illustrates the coreflooding apparatus, including a core holder, two floating-piston accumulators, a backpressure regulator, a set of pressure transducers, and a high-pressure dual-syringe pump. The core holder is made of Hastelloy stainless steel and can stand maximum pressure and temperature of 689.48 bar and 150°C, respectively. The capacity of each floating accumulator is 1 000 cm³ and can stand the pressure of 689.48 bar. The backpressure regulator is a dome-loaded type with pressure and temperature ratings of 689.48 bar and 175°C, respectively. The reading accuracy of the pressure transducers is 0.69 bar (for confining and inlet/outlet pressures as shown in Figure 7-5), and 0.45 bar for the backpressure regulator. The accuracy of the measured pump pressure is ±0.5% of full scale (689.48 bar). The volume of effluent is measured by a liquid fractional collector with an accuracy of ±0.1 cm³. The apparatus is equipped with an oven to run the tests at 60°C.

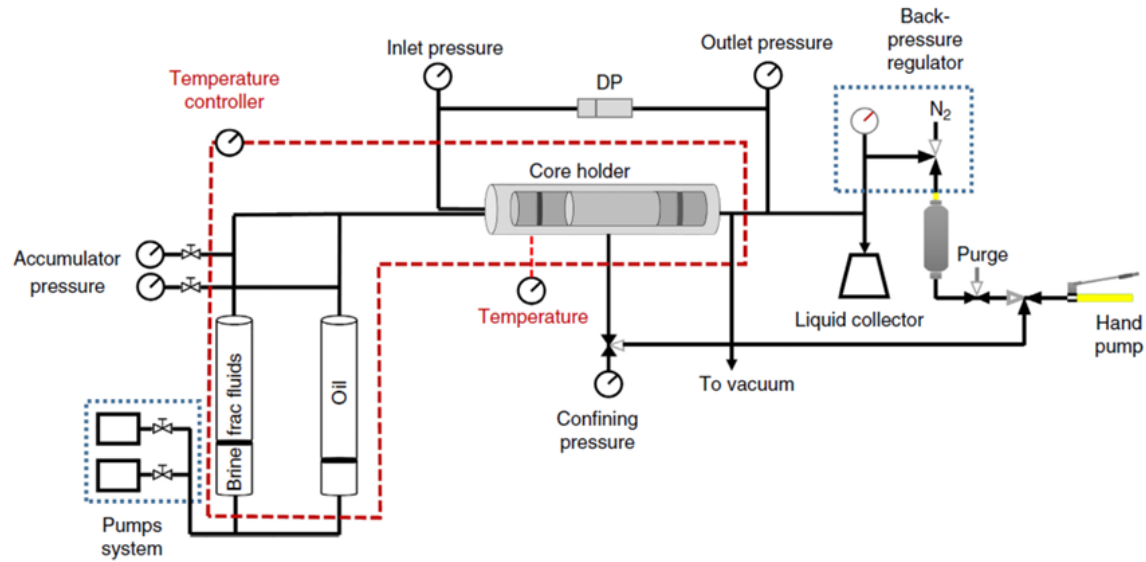


Figure 7–5: Schematic diagram of the core flooding apparatus. DP = differential pressure; N₂ = Nitrogen.

Table 7-5 lists the detailed experimental conditions of the tests using the coreflooding apparatus. First, we conducted Tests 1 and 2 on Plug B to compare the measured k_o^{eff} in the presence and absence of FF additives, and in particular the surfactants (a solution of three nonionic surfactants). The reference case (Test 2, fresh water as FF) was conducted on Plug B because it has the highest porosity and permeability among all the three plugs. The use of fresh water as the FF in this study was for reference purposes only and did not reflect the actual operations in the field. Second, Tests 3 through 8 were conducted to evaluate the effect of shut-in duration (3 and 14 days) on k_o^{eff} . Only FF was used during the leakoff of these six tests. It should be noted that Plugs A and C were not reconditioned (i.e., cleaning and measuring baseline permeability) after each test. Reconditioning was applied to Plug B before running Test 2. The reused plug was

flooded with approximately 7 pore volumes (PV) of oil and at high-enough oil rates to remove residual FF and restore to initial saturation conditions.

Table 7–5: List of experimental conditions of the core flooding tests to simulate leakoff and flowback processes. Except for the freshwater leakoff in Test 2, the remaining leakoff tests were conducted using the FF containing surfactants. One PV of freshwater/FF was injected during the leakoff process of all the tests

Coreflooding test	Plug	Leakoff		Shut-in time (days)	Flowback oil rate (cm ³ /min)
		Fluids	Flow rate (cm ³ /min)		
1	B	FF	0.09	3	0.090
2	B	Freshwater	0.09	3	0.090
3	A	FF	0.09	3	0.025
4	A	FF	0.09	14	0.025
5	B	FF	0.09	3	0.240
6	B	FF	0.09	14	0.240
7	C	FF	0.02	3	0.007
8	C	FF	0.02	14	0.007

The experimental procedure for simulating the leakoff and flowback processes includes four steps—saturating and aging the plugs to restore the reservoir conditions, leakoff process, shut-in time, and flowback process—as demonstrated in Figure 7-6.

Step 1, saturating and aging the plugs to restore reservoir conditions, includes the following substeps:

1. Flood the plugs with toluene and methanol to remove oleo and aqueous phases in the pore space, respectively.
2. Dry the plugs in an oven at 80°C for 3 days to remove the water remained in the pore space and the solvents (toluene and ethanol) used in the previous step, then apply vacuum to displace the trapped air.
3. Filter the oil sample to remove solid impurities. The oil sample was passed through 1 mm filter paper because 40 to 98% of the PV has pore-throat radii of less than 1 μm .
4. Inject 1 to 5 PV of brine at different flow rates (0.025 to 0.9 cm^3/min , depending on the plug permeability) into the cleaned and vacuumed plugs until equilibration of the pressure-drop values.
5. Inject 1 to 3 PV of the oil into the plugs at a low flow rate (0.007 to 0.240 cm^3/min , depending on the porosity and permeability of the plugs) to gradually displace the brine by oil until no further brine is produced.
6. Measure the weight of the plugs before and after the brine- and oil-injection processes using a balance to determine S_{wirr} . The reading accuracy of the balance is 0.1 mg.
7. Measure the volume of produced brine and compare this value with the volume of the brine injected in the first step. The purpose of measuring the produced-brine volume is to double-check the S_{wirr} values calculated by the weight-balance method.
8. Age the plugs in the oil at $P = 172$ bar and $T = 60^\circ\text{C}$ for 14 days to restore the reservoir conditions. Aging carbonate rocks in the oil is an essential step to restore reservoir conditions (Heidari et al. 2014), and minimum aging time of 2 weeks is recommended (Graue et al. 1999).

9. Inject the oil into the plugs at flow rates ranging from 0.007 to 0.240 cm³/min, depending on porosity and permeability of the plugs, to measure a baseline k_o^{eff} .

Step 2, the leakoff process, includes the following substeps:

1. Inject approximately 1 PV of FF/fresh water (or until pressure-drop stabilization) into one end of the oil-saturated plugs (i.e., the same end where brine and oil had been injected during the restoration of reservoir conditions in Step 1) at a constant flow rate (0.02 to 0.09 cm³/min), as shown in Figure 7-6b. Because monitoring the pressure change during the injection process is more practical compared with monitoring the flow rate, we perform the tests at constant flow rates.
2. Collect the produced-oil volume from the outlet of the core holder. The oil-production data are used to calculate the oil recovery after 1 PV injected.

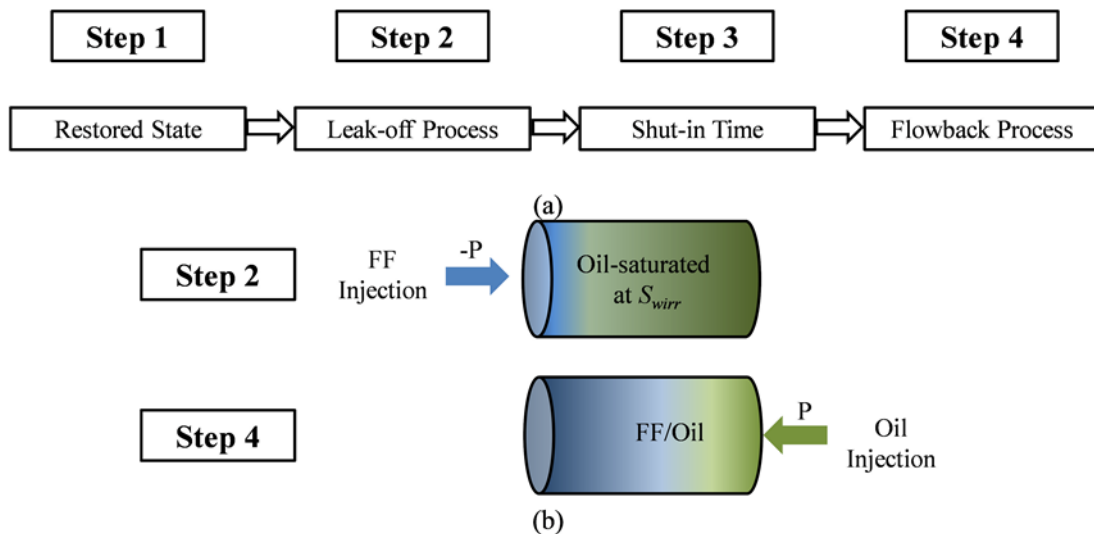


Figure 7-6: The procedure for the coreflooding tests: (a) simulating leakoff and flowback processes and (b) injection conditions in Steps 2 and 4.

Step 3, the shut-in period, includes keeping the inlet/outlet valves of the core holder closed for 3 or 14 days, representing short and long shut-in periods, respectively. These shut-in periods are sufficient to see the effects of FF redistribution in the plugs, and possible reactions among the rock minerals, initial oil and brine in the plugs, and leaked-off FF.

Step 4, the flowback process, includes the following substeps:

1. Inject the oil into the plugs from the other end to displace the invaded FF.

Because of unstable displacement observed during Step 1 in Figure 7-6a, constant pressures were initially applied for Plug C before switching to a constant flow rate ($0.007 \text{ cm}^3/\text{min}$) to simulate the flowback process. For Plugs A and B, constant flow rates (0.025 and $0.240 \text{ cm}^3/\text{min}$) were applied throughout the flowback process.

2. Collect effluent from the outlet of the core holder. The measured effluent volumes were used to calculate water saturation (S_w) after the flowback processes.

The pressure-drop values are selected to be negative ($-P$) for leakoff and positive ($+P$) for flowback processes. We use Darcy's law and the equilibrated pressure-drop values to determine absolute permeability (k_{abs}) by brine injection, baseline k_o^{eff} by oil injection at residual S_w before the leakoff process, and regained k_o^{eff} by oil injection during the flowback process.

7.3.2.IFT Measurements

The IFTs were measured for oil and fresh water/FF before the leakoff and after the flowback processes to explain the observed differences between regained permeability values. The IFT measurement was performed using a spinning-drop tensiometer. The spinning-drop tensiometer can operate at temperatures up to 120°C with an accuracy of

0.1°C. The accuracy of the IFT measurement is 10^{-6} mN/m. The instrument is equipped with a capillary tube and an end plug to hold the surfactants and oil, respectively. The IFT is measured by rotating the capillary tube at increasing speeds until the oil droplet is released. In this study, the instrument was used at the speed and temperature of 10 000 rev/min and 23°C, respectively. We used an integrated software to analyze the shape of the droplet spinning in the capillary tube, calculated IFT values, and reported the mean values. Before the leakoff, IFT measurements were conducted on oil and freshwater/FF samples before and after mixing. The purpose of mixing tests was to evaluate the effects of mixing rate on IFT values. We used a mixer to mix oil and FF samples at three rotational speeds of 1, 10, and 20 rev/min for 3 days. The volume ratio of oil and FF was 1:1. After the flowback, the IFTs were measured for collected oleo and aqueous samples. The IFT measurements were performed after waiting for approximately 2 hours for the fluids to equilibrate (Xu et al. 2008).

7.3.3. Brine/Oil-CA Measurements

Brine/oil CA values were measured to evaluate the wetting affinity of the plugs before the leakoff (Tests 3, 5, and 7) and after flowback (Tests 3 through 8) processes. The CA measurements were conducted three times for each test using an optical tensiometer with an accuracy of 0.1°. The mean values and standard deviations were reported. The plugs were first submerged in the brine, then the oil was dispensed from the bottom of the cell using a J-shaped capillary needle. The oil droplet moved upward and slowly attached to the surface of the plug. An integrated software performed curve-fitting on the droplet profiles to determine the CA.

7.4. Results and Discussions

Table 7-6 lists the results of k_{abs} , k_0^{eff} , and S_{wirr} measured in Step 1 (Figure 7-6a) at 60°C. To restore the reservoir conditions, all the plugs were saturated with brine and reservoir oil. The measured values of k_{abs} and k_0^{eff} follow the trend of porosity and permeability presented in Table 7-1. The ratio of k_{air} to k_{abs} is approximately 2.5 for the three plugs. The observed differences between absolute permeabilities measured by air and brine might be caused by non-Darcy-flow effects (e.g., Knudsen diffusion) of the flow of gas in micropores. The diffusivity of gas in confined spaces such as micropores is enhanced by Knudsen diffusion, a phenomenon where gas molecules collide with pore-wall surfaces more frequently than with each other (Ma and Holditch 2015). Plug B with the maximum permeability has the lowest S_{wirr} . Comparing k_0^{eff} before and after 14 days of aging in oil (under 172.37 bar and 60°C) shows that k_0^{eff} increases by 34, 70, and 34% after the aging process for Plugs A, B, and C, respectively. The changes in k_0^{eff} could be attributable to the redistribution of fluids within the pore structure of the plugs during the aging time. Plug B was reconditioned before running Test 2 and its baseline permeability was in the same range as the one listed in Table 7-6.

Table 7–6: Measured k_{abs} , k_o^{eff} and S_{wirr} of the plugs before and after the aging process

Plug	PV (cm ³)	Brine saturating		Injected brine		Oil saturating		Displaced brine		S_{wirr} (fraction)	After 14-day aging in oil at 60°C		
		q_b (cm ³ /min)	k_{abs} (mD)	q_o (cm ³ /min)	k_o^{eff} (mD)	q_o (cm ³ /min)	k_o^{eff} (mD)	q_o (cm ³ /min)	k_o^{eff} (mD)	k_o^{eff} improvement (%)			
A	1.70	0.060	0.051	2.71	0.025	0.026	1.70	0.37	0.025	0.035	34		
B	4.20	0.700	2.047	6.23	0.240	1.104	4.20	0.33	0.240	1.885	70		
	-	-	-	-	-	-	-	-	0.090	1.571	-		
C	0.60	0.075	0.034	1.16	0.007	0.003	0.60	0.48	0.007	0.004	34		

Figure 7-7 presents the IFT values measured between the oil and fresh water/FF before the leakoff and after the flowback processes. First, the IFT value between the oil and FF is 5.79 mN/m before the leakoff test (Figure 7-7a), which is 4.5 times lower than that between fresh water and oil (26.07 mN/m). Second, additional IFT measurements were purposely conducted under different mixing conditions to explain the reduction of IFT observed after the flowback process in Plug C. The measured IFT values between oil and FF after 3 days of mixing (1.79 to 1.13 mN/m) were approximately three to five times lower than that without mixing (5.79 mN/m). The higher mixing rate increases the contact interfaces between the oil and the FF, thus resulting in better partitioning and dispersion. Gupta (1982) conducted experiments and simulation studies on micellar/polymer flooding in Sloss Field, Nebraska, USA. The author reported that because of partitioning and dispersive-mixing effects, sulfonate partitioned into the oil phase and led to a reduction in IFT between oil and injected fluids, as well as an increase in the mobility of the oil phase. Third, the IFT values for the aqueous/oleo systems measured after the flowback process of Plugs A and B were very similar to those measured without mixing before the leakoff process (Figure 7-7b). However, for Plug C, the IFT value measured after the flowback was in the same range as initial values measured under various mixing conditions.

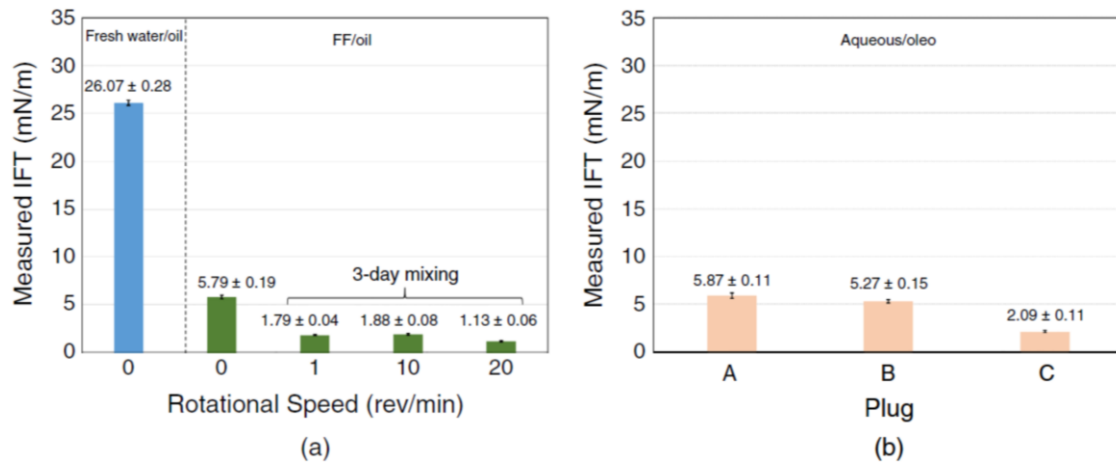


Figure 7-7: IFT values of (a) freshwater/oil and FF/oil systems measured at different mixing levels before the leakoff, and (b) aqueous/oleo systems measured after the flowback processes.

Table 7-7 lists brine/oil-CA values measured for the plugs. First, the brine/oil CAs for these plugs were measured after the aging process. The results indicate that the plugs are strongly oil-wet. This represents the conditions before the leakoff test. Then, the CAs were measured after the flowback process. Comparing the two sets of CA values does not suggest any significant wettability alteration resulting from interactions between the rock and the FF additives.

Table 7-7: Brine/oil CA values measured on the surface of the plugs before leakoff and after flowback processes

Plug	CA before the leakoff (°)	CA after the flowback (°)	
		3-day shut-in	14-day shut-in
A	171±5	151±11	147±14
B	153±8	150±4	146±2
C	172±3	175±3	170±3

7.4.1. Effect of Leakoff Fluids

Figure 7-8 shows the pressure-drop profiles during the leakoff and flowback process for Tests 1 and 2. In Test 2, fresh water is injected as the leakoff fluid into Plug B. In Figure 7-8a, the absolute value of pressure drop across the plug for the freshwater case is higher (by approximately 13.79 bar) than those for FF at 1-PV fluid injection. The breakthrough of FF and fresh water occurs at 0.63 and 0.52 PV injected, respectively. The early breakthrough of fresh water leads to a 30% lower oil recovery compared with that for the FF case (39 vs. 69%).

The observed differences between freshwater- and FF-leakoff tests can be explained using the fractional flow theory. The IFT between oil and FF is nearly five times lower than between the oil and fresh water. In addition, the measured viscosity of FF is approximately 1.5 times higher than that of fresh water. Therefore, during the leakoff process, the displacement of FF is expected to be slower than that of the fresh water because of its higher viscosity. On the other hand, the lower IFT of FF enhances its displacement efficiency. These factors lead to later breakthroughs of FF and higher oil recovery at 1 PV injected. The significantly lower pressure drop of FF during this period can be explained by its lower IFT value, leading to higher two-phase relative permeability values. Previous studies also used the fractional flow theory to explain the performance of chemical floods. Pope (1980) and Luo et al. (2017) applied fractional flow theory to study the low-tension enhanced oil recovery. The authors reported that if the viscosity of the injected chemical solution is increased, the low-tension fractional flow curve is shifted toward a lower residual oil saturation.

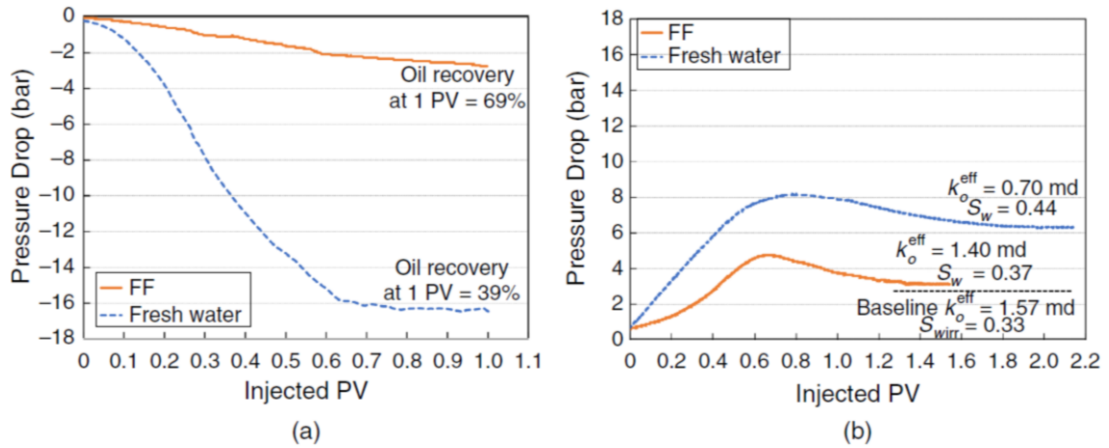


Figure 7-8: Pressure-drop profiles measured (a) during freshwater and FF leakoff, and (b) during flowback process of plug B ($q = 0.09 \text{ cm}^3/\text{min}$ in both processes).

In Figure 7-8b, the maximum pressure drop for Test 2 is 8.27 bar at the breakthrough point, while that for FF is 4.83 bar at the breakthrough point. The oil breakthrough during the flowback process in Tests 1 and 2 occurs at 0.75 and 0.66 PV, respectively. The equilibrium pressure drops (at the plateau conditions after the breakthrough) for Tests 1 and 2 are 3.10 and 6.34 bar, respectively. Consequently, k_o^{eff} calculated for the case of FF with surfactants is two times higher than that for the case of fresh water (1.4 vs. 0.7 mD). The calculated S_w values after the flowback of Tests 1 and 2 are 0.37 and 0.44, respectively.

The regained permeability after the flowback process for the case of FF leakoff is twice of that after freshwater leakoff. This can be explained by lower IFT between oil and FF compared with that between oil and fresh water, leading to higher two-phase relative permeability values during the flowback process. The lower phase trapping during the flowback of FF is supported by lower saturation of the remaining water in the plug for the case of FF compared with the freshwater case. Similarly, Liang et al. (2017) and Longoria et al. (2017) concluded that the reduction of IFT between hydrocarbon and

FF with surfactants after shut-in time changes the water saturation profile, and consequently enhances relative permeability to hydrocarbon.

7.4.2. Effect of Shut-In Times

During the extended shut-in periods after HF operations, the water inside fractures can imbibe into the rock matrix. This phenomenon might affect the regained permeability by changing the saturation state near the fracture face before the flowback process. The extent of this imbibition process depends on initial water saturation (Zhou et al. 2000), clay content and pore structure (Ghanbari et al. 2013; Zhou et al. 2016; Birkle and MaKechnie 2019), osmosis potential (Li et al. 2016), and capillary forces controlled by pore size, wettability, and IFT (Tagavifar et al. 2019).

To investigate the effects of shut-in on regained permeability, we measure k_o^{eff} for two different shut-in periods (i.e., 3 and 14 days) for the three plugs. The leaked-off water can spontaneously imbibe from the high- S_w to the low- S_w part of the pore network of the plugs if they are soaked for a specific period after the leakoff process. This can lead to a more uniform distribution of water across the plugs. We closed the inlet and outlet valves after the leakoff process to allow redistribution of the leaked-off water inside the plug and to allow interactions between fluids and rock during the shut-in periods.

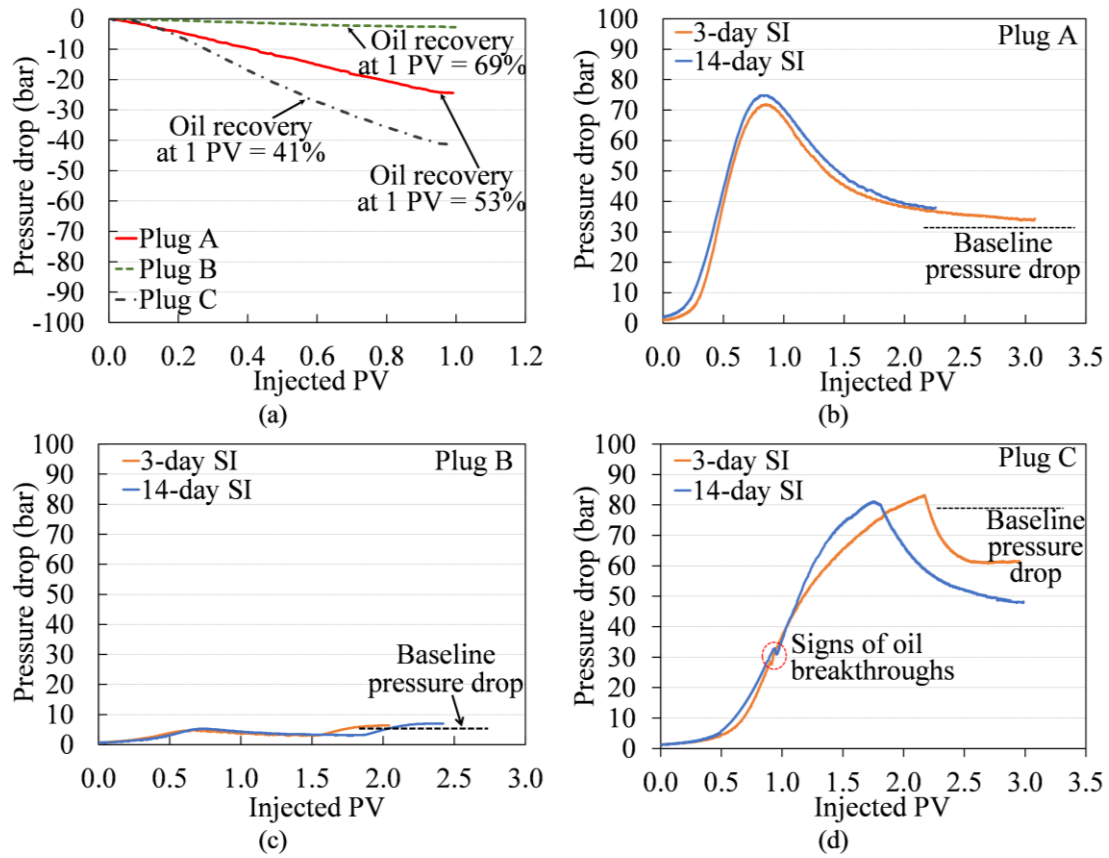


Figure 7-9: Pressure-drop profiles measured during (a) FF leakoff ($q = 0.09 \text{ cm}^3/\text{min}$ for plug A and B, and $q = 0.02 \text{ cm}^3/\text{min}$ for plug C), (b) flowback of plug A ($q = 0.025 \text{ cm}^3/\text{min}$), and (c) flowback of plug B ($q = 0.24 \text{ cm}^3/\text{min}$), and (d) flowback of plug C (constant pressures applied at two steps, i.e. 34 bar and 80 bar, for FF clean-up, then switched to $q = 0.007 \text{ cm}^3/\text{min}$ for k_o^{eff} measurements after 2 injected PV).

Figure 7-9 shows the pressure profiles during the leakoff and flowback processes for the three plugs (Tests 3 through 8). Table 7-8 summarizes the equilibrated values of oil-pressure drop and the corresponding k_o^{eff} before the leakoff process (the baseline) and at the end of the flowback process after 3- and 14-day shut-in periods. In Figure 7-9a, the absolute values of pressure drop during the leakoff process significantly increase with PV injected for Plugs A and C, while the value slightly increases for Plug B. Similar leakoff

tests are conducted in Tests 4, 6, and 8 (14-day shut-in), and the pressure-drop profiles are similar to those for Tests 3, 5, and 7 (3-day shut-in). Only one set of leakoff-test data (Tests 3, 5, and 7) is plotted in Figure 7-9a. The FF breakthrough occurs at 0.74, 0.63, and 0.82 PV injected for Plugs A, B, and C, respectively. The highest and lowest oil-recovery values are observed for Plugs B (69%) and C (41%), respectively.

Figures 7-9b, 7-9c, and 7-9d show the pressure-drop profiles during the flowback of Plugs A, B, and C (Tests 3 through 8). The lowest and highest equilibrium pressure-drop values are for Plugs B and C. Interestingly, the pressure drop for Plug C is even lower than the baseline value before the leakoff process.

Here, we define a regained-permeability index (RPI) to evaluate the change of k_o^{eff} relative to the corresponding baseline (before leakoff),

$$RPI = \frac{k_o^{\text{eff}}[\text{after FF/FW flowback}] - k_o^{\text{eff}}[\text{baseline}]}{k_o^{\text{eff}}[\text{baseline}]} \times 100 \quad (7-1)$$

Negative RPI values mean decreasing regained permeability compared with the baseline (before leakoff), and vice versa.

Table 7–8: Equilibrium pressure drop and k_o^{eff} values before leakoff (baseline) and after flowback processes after 3- and 14-day shut-in periods

Oil injection		Baseline		3-day shut-in			14-day shut-in		
Plug	rate (cm ³ /min)	Pressure drop (bar)	k_o^{eff} (mD)	Pressure drop (bar)	k_o^{eff} (mD)	RPI (%)	Pressure drop (bar)	k_o^{eff} (mD)	RPI (%)
A	0.025	31.85	0.035	34.06	0.033	-5.71	34.82	0.032	-8.57
B	0.240	5.65	1.885	6.34	1.680	-10.88	6.89	1.546	-17.98
C	0.007	79.22	0.004	61.64	0.005	28.52	48.13	0.006	64.61

Table 7–9: Changes in S_w during FF leakoff and flowback processes (Tests 3, 5 and 7)

Plug	PV (cm ³)	Invaded volume (cm ³)	FF flowback			S_{wirr} (fraction)	S_w after leakoff (fraction)	S_w after flowback			
			volume (cm ³)		S_{wirr} (fraction)			S_w after leakoff (fraction)	S_w after flowback (fraction)		
			3-day	14-day				3-day	14-day		
A	1.70	0.91	0.84	0.82	0.37	0.71	0.39	0.40			
B	4.20	2.91	2.70	2.69	0.33	0.79	0.36	0.36			
C	0.60	0.24	0.28	0.33	0.48	0.69	0.45	0.41			

Table 7-9 lists the measured S_w values for the plugs after leakoff and flowback processes. Because the invaded-FF volume and oil recovery in Tests 4, 6, and 8 (14-day shut-in) are similar to those for Tests 3, 5, and 7 (3-day shut-in), only one data set (Tests 3, 5, and 7) is presented. After flowback, S_w values are higher than S_{wirr} for Plugs A and B, while it is lower than S_{wirr} for Plug C (from 0.48 to 0.41–0.45). The water retention in Plugs A and B is evident from the negative RPI values (Table 7-8) and the higher S_w values after leakoff compared with the initial S_{wirr} . The observed reduction in S_w (compared with the initial S_{wirr}) for Plug C can be explained by effective mixing between leaked-off FF and initial brine, reducing trapped S_w during the flowback process.

The plugs used in this study have a low concentration of clays (trace to 1% of the whole rock weight), especially swelling (e.g., smectite) and migrating (e.g., kaolinite and illite) clays. Therefore, we do not expect permeability impairment by clay swelling or fines migration.

We observed differences in the pressure-drop and RPI values for all the plugs after 3- and 14-day shut-in periods as shown in Figure 7-9 and Table 7-8. The pressure-drop profiles for Plugs A and B show that extending the shut-in time from 3 to 14 days does not significantly affect the pressure drop. The equilibrium pressure drops for Plugs A and B after 3- and 14-day shut-in periods are very close. According to Table 7-8, the RPI values after 3-day shut-in time for Plugs A and B indicate a reduction of 5.71 and 10.88%, respectively, in regained permeability compared with the values before leakoff. The regained permeability slightly decreases by increasing shut-in times from 3 to 14 days. The results suggest that the duration of shut-in does not significantly affect the regained permeability in these plugs. Moreover, the increase in S_w compared with S_{wirr} is consistent with the decrease in regained permeability.

Because Plug C is very tight, the effect of increasing shut-in time (from 3 to 14 days) on regained permeability is more pronounced. The positive RPI for Plug C can be explained by lower S_w after flowback compared with S_{wirr} (Table 7-9) caused by IFT reduction. Longer shut-in provides more time for mixing of the invaded FF with the initial brine and oil in the plug, reducing IFT and thereby S_w . This IFT reduction indicates that effective mixing between leaked-off FF and initial brine in Plug C occurred during the leakoff, shut-in, and flowback processes. Moreover, the effective mixing is supported by the wider pore-throat-size distribution of this plug compared with Plugs A and B.

It should be noted that the measured CA values in Table 7-7 suggest that the exposure to the surfactants, even after 14 days of shut-in, might not significantly change the wettability of the plugs. To further compare the extent of capillary and viscous forces during the leakoff process, we calculated the dimensionless capillary number (Peters 2012) as

$$N_{cap} = 3.14 \times 10^{-8} \frac{\sigma \cos \theta \sqrt{k\phi}}{u\mu L} \quad (7-2)$$

where σ , h , k , and θ are IFT between the FF and oil, brine/oil CA after 3- and 14-day shut-in, baseline k_0^{eff} , and porosity of the plug, respectively. u , μ , and L are Darcy velocity of the injected FF, viscosity of the FF, and the length of the plug, respectively. Table 7-10 lists the N_{cap} values calculated for the leakoff processes of Tests 3 through 8. The resulting N_{cap} suggests that viscous and capillary forces coexist in all tests. The viscous force is dominant during the leakoff and flowback processes, while the capillary force is dominant during the shut-in time. Therefore, wettability alteration from an oil-wet to mixed-wet condition might accelerate spontaneous imbibition of FF during the shut-in time. Consequently, one can expect an improvement in regained permeability. Except for

Plug C, where an increase in k_o^{eff} is attributable to the effective mixing, the improvement of k_o^{eff} is not observed in the other plugs. This means that capillary imbibition and wettability alteration during the shut-in period are not significant. Hammond and Unsal (2009) conducted a modeling study on the extent of wettability alteration by spontaneous and forced imbibition of an aqueous-surfactant solution into an initially oil-filled oil-wet capillary tube. The authors reported that under forced-imbibition conditions, the wettability alteration is considered insignificant. It is because the effect of pressure on the velocity of the oil/water meniscus becomes more significant; therefore, there is insufficient time for large amounts of surfactants to transfer from the aqueous phase onto the wall of the capillary.

Table 7–10: Capillary-number calculations for the leakoff processes for Tests 3 to 8

Plug	Porosity (fraction)	Contact angle			$k_o^{\text{eff}}(\text{mD})$	u (m/s)	N_{cap}			
		(°)		IFT (mN/m)			3-day	14-day		
		3-day	14-day							
		shut-in	shut-in				shut-in	shut-in		
A	0.11	151	147	5.87	0.035	3.16×10^{-6}	0.15	0.14		
B	0.26	150	146	5.27	1.885	3.16×10^{-6}	0.15	0.15		
C	0.05	175	170	2.09	0.004	5.26×10^{-7}	0.05	0.05		

7.4.3.Effect of Plug Properties

The measured oil recovery after leakoff (Figure 7-9a) indicates that the highest displacement efficiency occurs for Plug B, followed by Plugs A and C. The lowest oil recovery is observed for Plug C because of the existence of meso and macropores/microfractures supported by the thin-section images and by the wider pore-throat-size distribution of this plug. These microfractures act as preferential conduits for

invaded FF, leading to low displacement efficiency during the leakoff process. Plug B, with the highest porosity and permeability, shows the lowest pressure-drop value (6.34 and 6.89 bar after 3- and 14-day shut-in periods, respectively). However, the increase in the regained permeability compared with the baseline occurs only for Plug C because of its high initial S_{wirr} and high dispersivity resulting from its wide pore-throat-size distribution. In summary, the regained permeability could be lower or higher than the baseline permeability, depending on petrophysical properties including porosity and permeability, pore structure, pore-size distribution, and S_{wirr} .

7.5.Limitations

We present the following limitations:

- The brine/oil CA was measured using the tangent method. The accuracy of the measured values is affected by determining rock/oil/brine-contact points, baselines, and gravitational distortion of the oil droplets.
- The PV of Plug C is small and is in the range of experimental errors. This affects the accuracy of S_w measured by a volumetric method.
- Reconditioning plugs to initial conditions is essential to ensure the repeatability, the accuracy of pressure drop, and regained k_o^{eff} comparison. There could be residual FF in reused plugs that might affect leakoff and flowback performances in subsequent tests.

7.6.Summary

The experimental results show that the combination of surfactants and well shut-in reduces phase trapping and improves k_o^{eff} during the flowback process depending on the permeability, pore structure, and S_{wirr} of the plugs.

We found that the addition of three nonionic surfactants to FF reduces the aqueous phase trapping (by lower saturation of the remaining water in the plug) and increases the regained permeability after the flowback process. Freshwater leakoff in Plug B reduced k_o^{eff} by 55% (from 1.57 mD to 0.7 mD) while FF (with surfactants) reduced k_o^{eff} by only 10%. The observed improvement of k_o^{eff} is primarily because of the reduction of interfacial tension (IFT) by the surfactants (from 26.07 mN/m to 5.79 mN/m). FF leakoff in Plugs A and C reduces k_o^{eff} by 5-10%, and this range only increases slightly by increasing the shut-in time from 3 to 14 days. However, for Plug C, the regained permeability is even higher than the original k_o^{eff} before the leakoff process. A 28.52% and 64.61% increase in k_o^{eff} after 3- and 14-day shut-in periods were observed. This observation is explained by an effective reduction of IFT between the oil and brine in the pore network of the tight plug, leading to a reduction of irreducible water saturation (S_{irr}). Moreover, extending the shut-in time enhances the mixing between invaded FF and oil/brine initially in the plug, leading to more effective reductions in IFT and consequently S_{irr} . We also found that capillary imbibition and wettability alteration during the shut-in period are insignificant.

Chapter 8 : Conclusions and Future Work

8.1. Conclusions

This research aims at qualitatively and quantitatively investigating phase behavior, gas-transport, and oil-recovery mechanisms during a natural-gas (C_1 and mixture of C_1/C_2) with huff ‘n’ puff (HnP); and qualitatively evaluating changes in oil effective permeability (k_o^{eff}) caused by fracturing-fluid (FF)-leakoff/flowback processes after hydraulic fracturing of tight-oil reservoirs and applying remediation methods. Here are the key conclusions from this dissertation.

8.1.1. Phase Behavior of The Natural-Gas/Oil Systems

- The miscibility conditions could be achieved by either increasing gas-injection pressure or increasing the molar fraction of C_2 in the gas mixtures.
- The presence of C_2 in the injection gas increases the oil swelling factor and significantly decreases the MMP of gas/oil mixtures.
- Reasonable Peng-Robinson-EOS models for oil/ C_1 and oil/ C_1/C_2 ($C_1/C_2:70/30$ mol%) systems were calibrated against constant-composition-expansion and MMP data. The predicted MMPs by plotting two-phase equilibrium data on ternary diagrams have good agreement with the measured ones.

8.1.2. Gas-Transport and Oil-Recovery Mechanisms during The Natural-Gas HnP Process

- Advection-dominated transport was found to be the mechanism responsible for the transport of gas into the plug at early times of the soaking period (Péclet number $N_{Pe} = 1.58$ to 3.03). However, molecular diffusion is the dominant mechanism when the soaking progresses ($N_{Pe} = 0.26$ to 0.62).

- From the four studied recovery mechanisms (total system compressibility, vaporization, oil swelling, and gas expansion), gas expansion is the dominant one, followed by total system compressibility, oil swelling, and vaporization.
- Expansion of free and solution gas during the depressurization period results in a significant comingled flow of gas and oil observed on the plug's surface. Therefore, the higher the amount of leaked-off gas during injection and soaking periods, the higher the oil recovery achieved by the gas-expansion mechanism.
- The enrichment of injected gas by C₂ (30 mol% in this study) improves the transport of gas into the core plug, and gas diffusivity, and oil recovery.

8.1.3. Aqueous Phase Trapping and Remediation Methods

- FF (with surfactants) significantly reduces effects of aqueous phase trapping and improves k_o^{eff} during flowback compared with fresh water.
- Shut-in durations have minor effects on k_o^{eff} on high-permeability plugs. However, an increase in k_o^{eff} is observed in the tight plug, and this range significantly increases by increasing shut-in time.
- IFT reduction and effective mixing of FF with initial oil/brine in the core plugs are the controlling mechanisms of k_o^{eff} improvement.

8.2. Significance of The Work to Unconventional Field Practices

8.2.1. Natural-Gas HnP Process

- *Developed Miscibility Conditions.* Knowing the range of MMPs corresponding to different levels of hydrocarbon enrichment helps operators in designing/optimizing the gas-compression system, reservoir-simulation-study sensitivity for the gas-injection EOR scenarios, and a long-term fieldwide development plan with consideration to the source of gas supply and gathering

facility. Since injection pressure is usually constrained by gas-compression system, miscibility conditions can be achieved by increasing the molar fraction of light hydrocarbon components, such as C₂ in this study, in the injected gas to cut the MMP to the desired level.

- *Start Time of The Gas HnP EOR.* The start time of the gas HnP EOR process is often a key question when planning a reservoir-development strategy. Injectivity is typically an issue if injection starts at the early of well life. It is because the formation pressure gradient is still high, resulting in less gas transported into the matrix. Injecting gas into a depleted reservoir would benefit from the total system compressibility and higher leaked-off gas and consequently oil recovery caused by the advective transport. Sanchez-Rivera et al. (2015) and Chen and Gu (2017) performed simulation studies of CO₂ HnP application in Bakken shale. The authors reported that the potential of repressurization (also known as gas expansion) is not fully used if the operation starts early in the well life.
- *Shut-in Time.* From the pressure-decline profiles in Fig. 5a, gas transport into the plug was pronounced in the first four days of the 7-day shut-in period. It means that a reasonable shut-in time to achieve high oil recovery might be less than 7 days. This observation is in agreement with the results of field pilots in which a shorter shut-in time (~5 days) seems to yield better oil recovery than longer ones (Jacobs 2019).
- *Injection and Depletion Strategy.* The results of this study show that improved gas transport into the matrix and an appropriate depletion strategy are two key factors leading to high oil recovery. In the field application, the efficiency of the gas HnP process might be improved by increasing injection pressure and/or enriching the injected gas by intermediate hydrocarbon components. Increasing injection pressure would be recommended as the first and preferable choice. First,

it is practical to inject at high-enough pressures to achieve miscible conditions. Second, a high injection pressure helps to spread out the gas farther from the matrix/fracture interface, thus increasing the surface area in contact with the gas. As mentioned in the “Oil-Recovery Mechanism during Depressurization Phase” section, the surface area created by fracturing operation significantly affects oil recovery by the gas-expansion mechanism. However, it may be difficult to achieve the MMP, for instance, 301.03 bar for oil/C₁, because this pressure may exceed the gas-compressor capacity and may lead to geomechanical complications such as refracturing the formation. With the limitation of injection pressure, the enrichment of injected gas, for example by 30 mol% C₂ in this study, is a viable solution to increase oil recovery. In terms of the depletion strategy, choke-size control is needed to optimize the pressure-depletion rate. A too fast pressure-depletion rate might lead to a rapid loss of energy from the gas expansion, while a too slow one may end up with insufficient gas energy to drag the oil along its flowpaths.

8.2.2. Surfactants and Well Shut-in during Hydraulic Fracturing

Surfactants and well shut-in have the most promising potential to reduce aqueous phase trapping during the flowback process and increase oil recovery. A short shut-in/soaking duration deems sufficient for k_o^{eff} improvement by IFT reduction in high-permeability rocks. Longer soaking times only benefit tight rocks by enhancing the mixing between FF and in-situ fluids, leading to a further reduction of IFT and water saturation.

8.3. Future Work

The experimental and modeling works presented in this study have been conducted under a set of assumptions and limitations. Here are some recommendations for future works:

- The visualization system needs to be upgraded to reduce the dead volume and make the injected gas/oil volume ratio closer to the field application.
- Additional natural-gas HnP tests are recommended using heterogeneous core samples, a live oil, and different pressure-depletion rates/injection pressures, i.e., above the MMP of the oil and gas mixture ($C_1/C_2:70/30$ mol%).
- Characterization of the reservoir oil by a system of multicomponent can improve the accuracy of the MMP/thermodynamic conditions prediction using the calibrated EOS.
- An analytical solution that calibrates pressure-decline and oil recovery data in the HnP tests can improve the estimation of D_{eff} and N_{Pe} values.
- Numerical modeling of the natural-gas HnP process is critical to scale up the results to field-scale for predicting pilot-scale response.
- Leakoff and flowback experiments were conducted using only three carbonate plugs. Because carbonate rocks are highly heterogeneous, more work is needed on samples with a wider range of porosity/permeability to obtain concrete conclusions regarding increasing regained permeability in tight plugs.

Bibliography

- Adekunle, O. and Hoffman, B.T. 2014. Minimum Miscibility Pressure Studies in the Bakken. SPE Improved Oil Recovery Symposium, 12-16 April, Tulsa, Oklahoma, USA. SPE-169077-MS. <https://dx.doi.org/10.2118/169077-MS>.
- Ahmadi, K. and Johns, R.T. 2011. Multiple-Mixing-Cell Method for MMP Calculations. *SPE J.* 16 (4): 733–742. SPE-116823-PA. <http://dx.doi.org/10.2118/116823-MS>.
- Alavian, S.A. 2011. Modeling CO₂ Injection in Fractured Reservoirs Using Single Matrix Block Systems. PhD Dissertation. Department of Petroleum Engineering and Applied Geophysics, Norwegian University of Science and Technology, Norway.
- Alavian, S.A. and Whitson, C.H. 2010. Scale dependence of diffusion in naturally fractured reservoirs for CO₂ injection. SPE-129666-MS. Presented at the SPE Improved Oil Recovery Symposium, Tulsa, Oklahoma, USA, 24–28 April. <https://dx.doi.org/10.2118/129666-MS>.
- Alboudwarej, H., Felix, J., and Badry, R. 2006. Highlighting Heavy Oil. *Oilfield Rev.* 18 (2): 34–53.
- Alfarge, D.; Wei, M.; Bai, B. 2017. IOR Methods in Unconventional Reservoirs of North America: Comprehensive Review. SPE Western Regional Meeting, Bakersfield, California, April. SPE-185640-MS. <https://doi.org/10.2118/185640-MS>.
- Alharthy, N.; Nguyen, T; Teklu, T.W. et al. 2013. Multiphase compositional modeling in small-scale pores of unconventional shale reservoirs. SPE Annual Technical Conference and Exhibition October, New Orleans, Louisiana, USA. SPE-166306-MS. <https://doi.org/10.2118/166306-MS>.

Alharthy, N.; Teklu, T.W; Kazemi, H. et al. 2018. Enhanced Oil Recovery in Liquid-Rich Shale Reservoirs: Laboratory to Field. *SPE Res Eval & Eng*, 21(01). SPE-175034-PA. <https://doi.org/10.2118/175034-PA>.

Al-Muntasher, G. A.; Liang, F.; Hull, K. L. 2017. Nanoparticle-Enhanced Hydraulic Fracturing Fluids: A Review. *SPE Prod & Oper*, 32(02). <https://dx.doi.org/10.2118/185161-PA>.

America: Comprehensive Review. SPE-185640-MS. SPE Western Regional Meeting, 23-27 April, Bakersfield, California. <https://doi.org/10.2118/185640-MS>.

Archie, G.E., 1942. The electrical resistivity log as an aid in determining some reservoir characteristics. *Petroleum Technology* 146(1), 55–62. <https://doi.org/10.2118/942054-G>.

Ashrafizadeh, S.N. and Ghasrodashti, A.A. 2011. An Investigation on the applicability of Parachor model for the prediction of MMP using five equations of state. *Chem. Eng. Res. Des.* 89 (6): 690-696. <https://doi.org/10.1016/j.cherd.2010.10.015>.

Asl, T.S.; Habibi, A.; Ezulike, O. B. et al. 2019. The Role of Microemulsion and Shut-in on Well Performance: From Field Scale to Laboratory Scale. SPE Hydraulic Fracturing Technology Conference and Exhibition, 5-7 February, The Woodlands, Texas, USA. SPE-194363-MS. <https://dx.doi.org/10.2118/194363-MS>.

Athar, K.; Doranegard, M.H.; Eghbali, S. et al. 2019. Measuring diffusion coefficients of gaseous propane in heavy oil at elevated temperatures. *J Therm Anal Calorim* 139, 2633–2645. <https://doi.org/10.1007/s10973-019-08768-7>.

Ayirala, S.C. and Rao, D.N. 2011. Comparative Evaluation of a New MMP Determination Technique. *J. of Can Pet Technol.* 50: 71-81. SPE 99606-PA. <https://doi.org/10.2118/99606-PA>.

Baek, S. and Akkutlu, Y. 2019a. Produced-Fluid Composition Redistribution in Source Rocks for Hydrocarbon-In-Place and Thermodynamic Recovery Calculations. *SPE J.*, 24(03). SPE-195578-PA. <https://doi.org/10.2118/195578-PA>.

Baek, S. and Akkutlu, Y. 2019b. Mean Free Path of Gas Molecules in Organic Nanochannels Using Molecular Simulations. *SPE J.*, 24(06). SPE-198889-PA. <https://doi.org/10.2118/198889-PA>.

Baker, R.O.; Yarranton, H.W.; Jensen, J.L. 2015. Practical Reservoir Engineering and Characterization, Part Two: Reservoir Data Analysis. Gulf Professional Publishing. Elsevier Inc. <https://doi.org/10.1016/C2011-0-05566-7>.

Bear, J. 2013. Dynamics of Fluids in Porous Media. Courier Corporations.

Bennion, D.B.; Thomas, F.B.; Bietz, R.F. et al. 1999. Remediation of Water and Hydrocarbon Phase Trapping Problems in Low Permeability Gas Reservoirs. *J Can Pet Technol*, 38(8), 39-48. <https://dx.doi.org/10.2118/99-08-01>.

Bennion, D.B.; Thomas, F.B.; Ma, T. 2000. Formation Damage Processes Reducing Productivity of Low Permeability Gas Reservoirs. SPE Rocky Mountain Regional/Low Permeability Reservoirs Symposium and Exhibition held in Denver, Colorado. SPE-60325-MS. <https://dx.doi.org/10.2118/60325-MS>.

Bennion, D.B.; Thomas, F.B.; Schulmeister, B. et al. 2006. Water and Oil Base Fluid Retention in Low Permeability Porous Media – an Update. Petroleum Society's 7th Canadian International Petroleum Conference (57th Annual Technical

Meeting), June 13–15, Calgary, Alberta, Canada. 2006-136.
<https://dx.doi.org/10.2118/2006-136>.

Bertонcello, A.; Wallace, J.; Blyton, C. et al. 2014. Imbibition and Water Blockage in Unconventional Reservoirs: Well-Management Implications During Flowback and Early Production. *SPE Res Eval & Eng* 17 (4): 497–506. SPE-167698-PA.
<https://doi.org/10.2118/167698-PA>.

Birdsell, D.T.; Karra, S.; Rajaram, H. 2018. On the Representation of the Porosity-Pressure Relationship in General Subsurface Flow Codes. *Water Resources Research* 54 (2): 1382-1388. <https://doi.org/10.1002/2017WR022001>.

Birkle, P. and MaKechnie, G.K. 2019. Geochemical Interpretation of Flowback Fluids to Assess Fracking Efficiency and Reservoir Compartmentalization. URTEC-198206-MS. SPE/AAPG/SEG Asia Pacific Unconventional Resources Technology Conference, 18-19 November, Brisbane, Australia. <https://doi.org/10.15530/AP-URTEC-2019-198206>.

Boudreau, B.P., 1996. The diffusive tortuosity of fine-grained unlithified sediments. *Geochimica et Cosmochimica Acta* 60(16), 3139–3142.
[https://doi.org/10.1016/0016-7037\(96\)00158-5](https://doi.org/10.1016/0016-7037(96)00158-5).

Bradley, P.S. and Mangasarian, O.L. 2000. *k*-Plane Clustering. *Journal of Global Optimization*, 16: 23–32. <https://doi.org/10.1023/A:1008324625522>.

Bui K. and Akkutlu, Y. 2017. Hydrocarbons Recovery from Model-Kerogen Nanopores. *SPE J*, 22(03). SPE-185162-PA. <https://doi.org/10.2118/185162-PA>.

Bui, K.; Akkutlu, Y.; Silas, J.A. 2020. Mass and Momentum Transfer Considerations for Oil Displacement in Source Rocks Using Microemulsion Solutions. *Fluids*, 5(44). doi:10.3390/fluids5020044.

Burrowes, G. 2001. Investigating CO₂ storage potential of carbonate rocks during tertiary recovery from a billion barrel oil field, Weyburn, Saskatchewan: Part 2 – reservoir geology (IEA Weyburn CO₂ Monitoring and Storage Project); in: Summary of Investigations 2001. Volume 1, Saskatchewan Geological Survey, Sask. Energy Mines, Misc. Rep. 2001-4.1.

Calsep A/S. 2018. PVTsim Nova, Revision 3. Lyngby, Denmark: Calsep A/S.

Canada Energy Regulator. 2013. The Ultimate Potential for Unconventional Petroleum from the Montney Formation of British Columbia and Alberta-Energy Briefing Note, <https://www.cer-rec.gc.ca/nrg/sttstc/ntrlgss/rprt/lmtptntlmntnyfrmtn2013/lmtptntlmntnyfrmtn2013-eng.html> (accessed 1 January 2020).

Carlsen, M; Whitson, C.; Dahouk, M.M. et al. 2019. Compositional Tracking of a Huff-n-Puff Project in the Eagle Ford. SPE/AAPG/SEG Unconventional Resources Technology Conference, 22-24 July, Denver, Colorado, USA. URTEC-2019-539-MS. <https://dx.doi.org/10.15530/urtec-2019-539>.

Carpenter, C. 2018. A Review of Improved-Oil-Recovery Methods in North American Unconventional Reservoirs. *JPT* 70(01). SPE-0118-0042-JPT. <https://doi.org/10.2118/0118-0042-JPT>.

Charbeneau, R.J. 2006. Groundwater Hydraulics and Pollutant Transport. Waveland Press.

- Chen, C. and Gu, M. 2017. Investigation of cyclic CO₂ huff-and-puff recovery in shale oil reservoirs using reservoir simulation and sensitivity analysis. *Fuel*, Volume 188: 102–111. <https://doi.org/10.1016/j.Fuel.2016.10.006>.
- Chen, C.; Balhoff, M.T; Mohanty, K.K. 2014. Effect of Reservoir Heterogeneity on Primary Recovery and CO₂ Huff 'n' Puff Recovery in Shale-Oil Reservoirs. *SPE Res Eval & Eng*, 17(03). SPE-164553-PA. <https://doi.org/10.2118/164553-PA>.
- Chen, P. and Mohanty, K. 2013. Surfactant-mediated spontaneous imbibition in carbonate rocks at harsh reservoir conditions. *SPE J* 18:124–33. SPE-153960-PA. <http://dx.doi.org/10.2118/153960-PA>.
- Civan, F. 2007. Reservoir Formation Damage Fundamentals, Modeling, Assessment, and Mitigation. Second Edition, Gulf Professional Publishing. <https://doi.org/10.1016/B978-0-7506-7738-7.X5000-3>.
- Cronin, M; Meybodi, H.E.; Johns, R.T. 2019. Diffusion-Dominated Proxy Model for Solvent Injection in Ultratight Oil Reservoirs. *SPE J*, 24(02). SPE-190305-PA. <https://doi.org/10.2118/190305-PA>.
- Davudov, D. and Moghanloo, R. G. 2018. Impact of Pore Compressibility and Connectivity Loss on Shale Permeability. *Int J Coal Geol* 187: 98–113. <https://doi.org/10.1016/j.coal.2018.01.008>.
- de Rezende, F. C., Rabelo, R. B., Kinouti, L. et al. 2019. Tailoring Alkoxylation of Flowback Aid Surfactants for Maximum Efficiency. Paper presented at the SPE International Conference on Oilfield Chemistry, Galveston, Texas, USA, 8–9 April. SPE-193623-MS. <https://doi.org/10.2118/193623-MS>.

Derkani, M.H.; Fletcher, A.J.; Abdallah, W. et al. 2018. Low Salinity Waterflooding in Carbonate Reservoirs: Review of Interfacial Mechanisms. *Colloids Interfaces*, 2, 20; <https://doi:10.3390/colloids2020020>.

Dincer, I. and Rosen, M.A. 2013. Exergy (Second Edition) - Energy, Environment and Sustainable Development. Chapter 4. Elsevier. <https://doi.org/10.1016/B978-0-08-097089-9.00004-8>.

Dutta, R.; Lee, C-H.; Odumabo, S. et al. 2014. Experimental investigation of fracturing-fluid migration caused by spontaneous imbibition in fractured low-permeability sands. *SPE Res Eval & Eng*, 17(01). SPE-154939-PA. <https://dx.doi.org/10.2118/154939-PA>.

Dymond, J. H. and Malhotra, R. 1988. The Tait Equation: 100 Years On. *Int. J. Thermophys.* 9 (6): 941–951. <https://doi.org/10.1007/BF01133262>.

Eghbali, S. and Dehghanpour, H. 2018. An Experimental and Modeling Study of Carbon Dioxide/Bitumen and C4/Bitumen Phase Behavior at Elevated Temperatures Using Cold Lake Bitumen. *SPE J.* 23 (06). SPE-187259-PA. <https://doi.org/10.2118/187259-PA>.

Egwuenu, A.M.; Johns, R.T.; Li, Y. 2004. Improved Fluid Characterization for Miscible Gas Floods. *SPE Res Eval & Eng*, 11 (04). SPE-94034-PA. <https://doi.org/10.2118/94034-PA>.

Fick, A. 1855. On liquid diffusion. *Philosophical Magazine*, 294 (X): 30-39.

Fried, J.J. and Combarous, M.A. 1971. Dispersion in Porous Media. *Advance in Hydroscience* 7:169-282. <https://doi.org/10.1016/B978-0-12-021807-3.50008-4>.

Fu, Q.; Cudjoe, S.; Barati, R. et al. 2019. Experimental and Numerical Investigation of the Diffusion-Based Huff-n-Puff Gas Injection into Lower Eagle Ford Shale Samples. SPE/AAPG/SEG Unconventional Resources Technology Conference, 22-24 July, Denver, Colorado, USA. URTEC-2019-402-MS.
<https://dx.doi.org/10.15530/urtec-2019-402>.

Gao, G., Daridon, J.L., Saint-Guirons, H. et al. 1992. A simple correlation to evaluate binary interaction parameters of the Peng-Robinson equation of state: binary light hydrocarbon systems. *Fluid Phase Equilibria*, 74:85-93.
[https://doi.org/10.1016/0378-3812\(92\)85054-C](https://doi.org/10.1016/0378-3812(92)85054-C).

Geoscience BC. 2011. Deep Subsurface Aquifer Characterization in Support of Montney Tight Gas Development: Geological Report.
http://cdn.geosciencebc.com/project_data/GBC_Report2011-11/GBC2011-11_Montney_Aquifer_Characterization_Report.pdf.

Ghanbari, E. and Dehghanpour, H. 2016. The fate of fracturing water: A field and simulation study. *Fuel*, 163, 282–294. <https://doi.org/10.1016/j.fuel.2015.09.040>.

Ghanbari, E.; Abbasi, M.A.; Dehghanpour, H. et al. 2013. Flowback Volumetric and Chemical Analysis for Evaluating Load Recovery and Its Impact on Early-Time Production. SPE-167165-MS. SPE Unconventional Resources Conference Canada, 5-7 November, Calgary, Alberta, Canada. <https://doi.org/10.2118/167165-MS>.

Ghanizadeh, A.; Bhowmik, S.; Haeri-Ardakani, O. et al. 2015. A comparison of shale permeability coefficients derived using multiple non-steady-state measurement techniques: Examples from the Duvernay Formation, Alberta (Canada). *Fuel* 140: 371–387. <http://dx.doi.org/10.1016/j.Fuel.2014.09.073>.

Gherabati, S.A.; Browning, J.; Male, F. et al. 2017. Evaluating Hydrocarbon-in-Place and Recovery Factor in a Hybrid Petroleum System: Case of Bakken and Three Forks in North Dakota. SPE/AAPG/SEG Unconventional Resources Technology Conference, 24-26 July, Austin, Texas, USA. 2671498-MS URTEC. <https://dx.doi.org/10.15530/URTEC-2017-2671498>.

Ghori, K.A.A. 2013. Emerging Unconventional Shale Plays in Western Australia. *APPEA J* 53(1): 313-336. <https://doi.org/10.1071/AJ12027>.

Grathwohl, P. 2012. Diffusion in Natural Porous Media Contaminant Transport, Sorption/Desorption and Dissolution Kinetics. Springer US. Springer Science+Business Media New York.

Graue, A.; Viksund, B. G.; Baldwin, B. A. 1999. Reproducible Wettability Alteration of Low-Permeable Outcrop Chalk. *SPE Res Eval & Eng*, 2(02). SPE-55904-PA. <https://doi.org/10.2118/55904-PA>.

Gupta, S.P. 1982. Dispersive Mixing Effects on the Sloss Field Micellar System. *SPE J*, 22(04). SPE-9782-PA. <https://doi.org/10.2118/9782-PA>.

Habibi, A., Yassin, M.R., Dehghanpour, H. et al. 2017. Experimental investigation of CO₂/oil interactions in tight rocks: A Montney case study. *Fuel* 203: 853–867. <http://dx.doi.org/10.1016/j.Fuel.2017.04.077>.

Hammond, P.S. and Unsal, E. 2009. Spontaneous and Forced Imbibition of Aqueous Wettability Altering Surfactant Solution into an Initially Oil-Wet Capillary. *Langmuir*, 25(21), 12591–12603. <https://doi.org/10.1021/la901781a>.

Hawkins, G.W. 1988. Laboratory Study of Proppant-Pack Permeability Reduction Caused by Fracturing Fluids Concentrated During Closure. Presented at the 1988

SPE Annual Technical Conference and Exhibition, Houston, Texas, 2-5 October.
SPE-18261-MS. <https://dx.doi.org/10.2118/18261-MS>.

Hawthorne, S.B., Miller, D.J., Jin, L. et al. 2016. Rapid and Simple Capillary-Rise/Vanishing Interfacial Tension Method to Determine Crude Oil Minimum Miscibility Pressure: Pure and Mixed CO₂, Methane, and Ethane. *Energy Fuels*, 30, 6365–6372. <http://dx.doi.org/10.1021/acs.energyfuels.6b01151>.

Hawthorne, S.B.; Gorecki, C.D.; Sorensen, J.A. et al. 2013. Hydrocarbon mobilization mechanisms from upper, middle, and lower Bakken reservoir rocks exposed to CO₂. SPE-167200-MS, presented at the SPE Unconventional Resources Conference Canada, 5-7, November, Canada. <https://dx.doi.org/10.2118/167200-MS>.

He, K. and Xu, L. 2017. Unique Mixtures of Anionic/Cationic Surfactants: A New Approach to Enhance Surfactant Performance in Liquids-Rich Shale Reservoirs. SPE International Conference on Oilfield Chemistry, Montgomery, Texas, USA, 2017. SPE-184515-MS. <https://doi.org/10.2118/184515-MS>.

He, K., Xu, L., Gao, Y. et al. 2015. Evaluation of surfactant performance in fracturing fluids for enhanced well productivity in unconventional reservoirs using Rock-on-a-Chip approach. *J. Pet. Sci. Eng.* 135, 531–541. <https://doi.org/10.1016/j.petrol.2015.10.008>.

He, K. and Xu, L., 2015. Addressing Operator Concerns: Will Surfactant's Performance be Compromised Under Harsh Conditions? SPE-174361-MS. EUROPEC 2015, 1-4 June, Madrid, Spain. <https://doi.org/10.2118/174361-MS>.

Heidari, M.A.; Habibi, A.; Ayatollahi, S. et al. 2014. Effect of time and temperature on crude oil aging to do a right surfactant flooding with a new approach. In

Proceedings of the Offshore Technology Conference-Asia, Kuala Lumpur, Malaysia, 25–28 March. OTC-24801-MS. <https://dx.doi.org/10.4043/24801-MS>.

Hertel, S.A.; Rydzy, M.; Anger, B. et al. 2018. Upscaling of Digital Rock Porosities by Correlation With Whole-Core CT-Scan Histograms. *Petrophysics*, 59 (5): 694–702. SPWLA-2018-v59n5a8. <https://dx.doi.org/10.30632/PJV59N5-2018a8>.

Himes, R.; Lansford, M.L.; Duenckel, R. et al. 2017. Improved Method to Evaluate Flowback Additives for Frac Fluids Used in Unconventional Reservoirs. SPE Annual Technical Conference and Exhibition, 9-11 October, San Antonio, Texas, USA. SPE-187200-MS. <https://doi.org/10.2118/187200-MS>.

Hirasaki, G.; Miller, C.A.; Puerto, M. 2011. Recent Advances in Surfactant EOR. *SPE J.*, 16, 04, pp 889-907. <https://dx.doi.org/10.2118/115386-PA>.

Hobbs, B. and Ord, A. 2015. Structural Geology: The Mechanics of Deforming Metamorphic Rocks. Imprint Elsevier. <https://doi.org/10.1016/C2012-0-01215-X>.

Hoffman, B.T. 2018. Huff-N-Puff Gas Injection Pilot Projects in the Eagle Ford. Paper presented at SPE Canada Unconventional Resources Conference, Calgary, Alberta, Canada. 13-14, March. SPE-189816-MS. <https://dx.doi.org/10.2118/189816-MS>.

Hoffman, B.T. and Evans, J.G. 2016. Improved Oil Recovery IOR Pilot Projects in the Bakken Formation. SPE Low Perm Symposium, 5-6 May, Denver, Colorado, USA. SPE-180270-MS. <https://dx.doi.org/10.2118/180270-MS>.

Hoffman, B.T. and Reichhardt, D. 2019. Quantitative Evaluation of Recovery Mechanisms for Huff-n-puff Gas Injection in Unconventional Reservoirs. URTEC-2019-147-MS. Unconventional Resources Technology Conference held in Denver, Colorado, USA. <https://doi.org/10.15530/urtec-2019-147>.

Holditch, S.A. 1979. Factors Affecting Water Blocking and Gas Flow from Hydraulically Fractured Gas Wells. *J Pet Technol* 31 (12): 1515–1524. SPE-7561-PA. <https://doi.org/10.2118/7561-PA>.

Hoteit, H. and Firoozabadi, A. 2009. Numerical Modeling of Diffusion in Fractured Media for Gas-Injection and -Recycling Schemes. *SPE J* 14(02). SPE-103292-PA. <https://doi.org/10.2118/103292-PA>.

Hughes, J.D. 2013. A reality check on the shale revolution. *Nature*, 494, 307–308. <https://doi.org/10.1038/494307a>.

Jacobs, T. 2015. Letting It Soak In: Delaying Flowback Delivers Unique Results. *JPT*, 67(12). SPE-1215-0037-JPT. <https://dx.doi.org/10.2118/1215-0037-JPT>.

Jacobs, T. 2019. Shale EOR Delivers, So Why Won't the Sector Go Big? *JPT* 71(05). SPE-0519-0037-JPT. <https://doi.org/10.2118/0519-0037-JPT>.

Javadpour, F. 2009. Nanopores and Apparent Permeability of Gas Flow in Mudrocks (Shales and Siltstone). *Journal of Canadian Petroleum Technology*, 48(08). PETSOC-09-08-16-DA. <https://doi.org/10.2118/09-08-16-DA>.

Jessen, K.; Michelsen, M.; Stenby, E.H. 1998. Global approach for calculation of minimum miscibility pressure. *Fluid Phase Equilibria*. 153 (2): 251-263. [https://doi.org/10.1016/S0378-3812\(98\)00414-2](https://doi.org/10.1016/S0378-3812(98)00414-2).

Jessen, K.; Orr, F.M. 2008. On Interfacial-Tension Measurements to Estimate Minimum Miscibility Pressures. *SPE Res Eval & Eng*, 11 (5). SPE-110725-PA. <https://doi.org/10.2118/110725-PA>.

Jha, R.K.; Bryant S.L.; Lake, L.W. 2011. Effect of diffusion on dispersion. *SPE J*, 16 (1). SPE 115961-PA. <https://doi.org/10.2118/115961-PA>.

Jin, L., Steve, H., James, S., Lawrence, P. et al. 2017. Utilization of Produced Gas for Improved Oil Recovery and Reduced Emissions from the Bakken Formation. SPE Health, Safety, Security, Environment, & Social Responsibility Conference - North America, 18-20 April, New Orleans, Louisiana, USA. SPE-184414-MS. <https://dx.doi.org/10.2118/184414-MS>.

Johns, R.T., Sah, P., Solano, R. 2002. Effect of dispersion local displacement efficiency for multicomponent enriched-gas floods above the minimum miscibility enrichment. *SPE Res Eval & Eng* 5 (1): 4-10. SPE-75806-PA. <https://doi.org/10.2118/75806-PA>.

Johnson, L.M.; Shepherd, S.D.; Rothrock, G.D. et al. 2016. Core/Shell Systems for Delayed Delivery of Concentrated Mineral Acid. *SPE Prod & Oper*, 31(04). <https://doi.org/10.2118/173734-PA>.

Katz, D.L. and Firoozabadi, A. 1978. Predicting Phase Behavior of Condensate/Crude Oil Systems Using Methane Interaction Coefficients. *J of Pet Technol*, 30, 1649-1655. SPE-6721-PA. <http://dx.doi.org/10.2118/6721-PA>.

Kaul, P.K. 1999. An Analysis of Phase Behavior and Displacement Characteristics of Multicomponent Mixtures. PhD Dissertation, Stanford University, Palo Alto, California, USA.

King, G.E. 2010. Thirty Years of Gas Shale Fracturing: What Have We Learned? SPE-133456-MS. SPE Annual Technical Conference and Exhibition, 19-22 September, Florence, Italy. <https://doi.org/10.2118/133456-MS>.

King, G.E. 2012. Hydraulic Fracturing 101: What Every Representative, Environmentalist, Regulator, Reporter, Investor, University Researcher, Neighbor,

and Engineer Should Know About Hydraulic Fracturing Risk. *SPE JPT* 64 (4). SPE-0412-0034-JPT. <https://doi.org/10.2118/0412-0034-JPT>.

King, G.E. 2014. 60 Years of Multi-Fractured Vertical, Deviated and Horizontal Wells: What Have We Learned? SPE-170952-MS. SPE Annual Technical Conference and Exhibition, 27-29 October, Amsterdam, The Netherlands. <https://doi.org/10.2118/170952-MS>.

King, G.E. 2014. Maximizing Recovery Factors: Improving Recovery Factors in Liquids-Rich Resource Plays Requires New Approaches. The American Oil and Gas Reporter. <https://www.aogr.com/magazine/editors-choice/improving-recovery-factors-in-liquids-rich-resource-plays-requires-new-appr>.

Kumar, A. 2016. Characterization of Reservoir Fluids based on Perturbation from n-Alkanes. PhD Dissertation, University of Alberta, Edmonton, Alberta, Canada. <https://doi.org/10.7939/R3PR7N024>.

Kurtoglu, B., 2013. Integrated reservoir characterization and modeling in support of enhanced oil recovery for Bakken. Ph.D. Dissertation. Department of Petroleum Engineering at the Colorado School of Mines. <http://hdl.handle.net/11124/24>.

Lai, J.; Guo, J.; Zhou, H. et al. 2018. Pore Structure and Mechanical Property Change on the Surface of the Tight Limestone After Acid-Rock Reaction. ARMA 18–1048. 52nd US Rock Mechanics / Geomechanics Symposium held in Seattle, Washington, USA, 17–20 June.

Lake, L.W. 1989. Enhanced Oil Recovery. First Edition. Prentice Hall, Engelwood Cliffs, NJ 07632.

- Lan, Y.; Moghanloo, R.G; Davudov, D. 2017. Pore Compressibility of Shale Formations. SPE J. 22 (6). SPE-185059-PA. <https://doi.org/10.2118/185059-PA>.
- Lashgari, H. R.; Sun, A.; Zhang, T. et al. 2019. Evaluation of Carbon Dioxide Storage and Miscible Gas EOR in Shale Oil Reservoirs. Fuel 241: 1223–1235. <https://doi.org/10.1016/j.fuel.2018.11.076>.
- Lee, B. I. and Kesler, M. G. 1975. A Generalized Thermodynamic Correlation Based on Three-Parameter Corresponding States. *AICHE J.* 21 (3): 510–527. <https://doi.org/10.1002/aic.690210313>.
- Leimkuhler, J. and Leveille, G. 2012. Unconventional Resources. SPE-0112-026-TWA. SPE The Way Ahead 8(1). <https://doi.org/10.2118/0112-026-TWA>.
- Leung, J.Y. and Srinivasan, S. 2011. Analysis of uncertainty introduced by scaleup of reservoir attributes and flow response in heterogeneous reservoirs. SPE J. 16 (3). SPE-145678-PA. <https://doi.org/10.2118/145678-PA>.
- Li, C.; Pu, H.; Zhong, X. et al. 2020. Interfacial interactions between Bakken crude oil and injected gases at reservoir temperature: A molecular dynamics simulation study. *Fuel* 276 118058. <https://doi.org/10.1016/j.Fuel.2020.118058>.
- Li, D. and Lake, L.W. 1995. Scaling fluid flow through heterogeneous permeable media. SPE Advanced Technology Series, 3 (1). SPE-26648-PA. <https://doi.org/10.2118/26648-PA>.
- Li, L. and Sheng, J.J. 2017. Upscale methodology for gas huff-n-puff process in shale oil reservoirs. J. Pet. Sci. Eng. 153: 36–46. <http://dx.doi.org/10.1016/j.petrol.2017.03.028>.

Li, N.; Zheng, Z.; Guo, P. et al. 2019. Successful Treatment and Reuse of Flowback Guar Frac-Fluid in Ordos Basin and Associated Cost Savings to Operators. IPTC-19555-MS. International Petroleum Technology Conference, 26-28 March, Beijing, China. <https://doi.org/10.2523/IPTC-19555-MS>.

Li, S. and Luo, P. 2017. Experimental and simulation determination of minimum miscibility pressure for a Bakken tight oil and different injection gases, *Petroleum*, 3 (1): 79-86. <https://doi.org/10.1016/j.petlm.2016.11.011>.

Li, S.; Qiao, C.; Zhang C.; Li, Z. 2018. Determination of diffusion coefficients of supercritical CO₂ under tight oil reservoir conditions with pressure-decay method. *Journal of CO₂ Utilization* 24: 430–443. <https://doi.org/10.1016/j.jcou.2018.02.002>.

Li, X.; Teklu, T. Q.; Abass, H. et al. 2016. The Impact of Water Salinity/Surfactant on Spontaneous Imbibition through Capillarity and Osmosis for Unconventional IOR. SPE/AAPG/SEG Unconventional Resources Technology Conference, 1-3 August, San Antonio, Texas, USA. URTEC-2461736-MS. <https://dx.doi.org/10.15530/URTEC-2016-2461736>.

Liang, T.; Longoria, R. A.; Lu, J. et al. 2015. The Applicability of Surfactants on Enhancing the Productivity in Tight Formations. Unconventional Resources Technology Conference, 20-22 July, San Antonio, Texas, USA. URTEC-2154284-MS. <https://dx.doi.org/10.15530/URTEC-2015-2154284>.

Liang, T.; Longoria, R. A.; Lu, J. et al. 2017. Enhancing Hydrocarbon Permeability after Hydraulic Fracturing: Laboratory Evaluations of Shut-Ins and Surfactant Additives. *SPE J*, 22, 04. <http://dx.doi.org/10.2118/175101-PA>.

Liu, D.; Yuan, P.; Liu, H. et al. 2013. High-pressure adsorption of methane on montmorillonite, kaolinite and illite. *Applied Clay Science*, 85, 25-30. <http://dx.doi.org/10.1016/j.clay.2013.09.009>.

Liu, Y.; Leung, J.Y.; Chalaturnyk, R.J. et al. 2019. New Insights on Mechanisms Controlling Fracturing-Fluid Distribution and Their Effects on Well Performance in Shale-Gas Reservoirs. SPE-185043-PA. *SPE Prod & Oper* 34 (3). <https://doi.org/10.2118/185043-PA>.

Liu., S; Sahni, V.; Tan, J. et al. 2018. Laboratory Investigation of EOR Techniques for Organic Rich Shales in the Permian Basin. Paper presented at SPE/AAPG/SEG Unconventional Resources Technology Conference, 23-25 July, Houston, Texas, USA. URTEC-2890074-MS. <https://dx.doi.org/10.15530/URTEC-2018-2890074>.

Longoria, R. A.; Liang, T., Huynh, U. T., et al. 2017. Water blocks in tight formations: the role of matrix/fracture interaction in hydrocarbon-permeability reduction and its implications in the use of enhanced oil recovery techniques. *SPE J*, 22,05. <http://dx.doi.org/10.2118/185962-PA>.

Lou, X.; Chakraborty, N.; Karpyn, Z. et al. 2019. Experimental Study of Gas-Liquid Diffusion in Porous Rocks and Bulk Fluids to Investigate the Effect of Rock Matrix Hindrance. *SPE J.* Preprint. <https://doi.org/10.2118/195941-PA>.

Lu, J., Steve, H., James, S., Lawrence, P. et al. 2017. Utilization of Produced Gas for Improved Oil Recovery and Reduced Emissions from the Bakken Formation. SPE Health, Safety, Security, Environment, & Social Responsibility Conference - North America, 18-20 April, New Orleans, Louisiana, USA. SPE-184414-MS. <https://dx.doi.org/10.2118/184414-MS>.

Lucia, F. J. 2007. Carbonate Reservoir Characterization: An Integrated Approach. Second Edition. Springer.

Luo, H.; Delshad, M.; Zhao, B. et al. 2017. A Fractional Flow Theory for Unstable Immiscible Floods. SPE Canada Heavy Oil Technical Conference, 15-16 February, Calgary, Alberta, Canada. SPE-184996-MS. <https://dx.doi.org/10.2118/184996-MS>.

Ma, Y.Z. and Holditch, S.A. 2015. Unconventional Oil and Gas Resources Handbook. First Edition. Gulf Professional Publishing in an imprint of Elsevier.

Martinsen, S.O.; Castiblanco, L.A.; Whitson, C. H. 2010. Advanced Fluid Characterization of Pauto Complex, Colombia. SPE Annual Technical Conference and Exhibition, 19-22 September, Florence, Italy. SPE-135085-MS. <https://dx.doi.org/10.2118/135085-MS>.

McGuire, P. R.; Okuno, R.; Gould, T. L. et al. 2017. Ethane-Based Enhanced Oil Recovery: An Innovative and Profitable Enhanced-Oil-Recovery Opportunity for a Low-Price Environment. *SPE Res Eval & Eng* 20 (1): 42–58. SPE-179565-PA. <https://doi.org/10.2118/179565-PA>.

McKishnie, R.A., Malik, S., Chugh, S. et al. 2005. Streamline Technology for the Evaluation of Full-Field Compositional Processes: Midale-A Case Study. *SPE Res Eval & Eng* 8 (5): 404–417. SPE-89363-PA. <https://doi.org/10.2118/89363-PA>.

McPhee, C.; Reed, J.; Zubizarreta, I. 2015. Core Analysis: A Best Practice Guide. Chapter 4. Volume 64. First Edition. Elsevier.

Metcalfe, R.S. 1982. Effects of Impurities on Minimum Miscibility Pressures and Minimum Enrichment Levels for CO₂ and Rich-Gas Displacements. *SPE J.*, 22, 219–225. SPE-9230-PA. <https://doi.org/10.2118/9230-PA>.

Mirchi, V.; Saraji, S.; Goual, L. et al. 2015. Dynamic interfacial tension and wettability of shale in the presence of surfactants at reservoir conditions. *Fuel*, 148, 127-138. <https://doi.org/10.1016/j.Fuel.2015.01.077>.

Mirzaei, M.; DiCarlo, D. A.; Pope, G. A. 2016. Visualization and analysis of surfactant imbibition into oil-wet fractured cores. *SPE J.*, 21, 01. <http://dx.doi.org/10.2118/166129-PA>.

Mohebbinia, S. and Wong, T. 2017. Molecular Diffusion Calculations in Simulation of Gasfloods in Fractured Reservoirs. SPE-182594-MS. SPE Reservoir Simulation Conference, 20-22 February, Montgomery, Texas, USA. <https://doi.org/10.2118/182594-MS>.

Montgomery, C. 2013. Effective and Sustainable Hydraulic Fracturing. Chapter 2: Fracturing Fluid Components. IntechOpen Publisher. <https://dx.doi.org/10.5772/56422>.

Moulu, R.C. 1989. Solution-gas Drive: Experiments and Simulation. *Journal of Petroleum Science and Engineering*, 2(4): 379-386. [https://doi.org/10.1016/0920-4105\(89\)90011-9](https://doi.org/10.1016/0920-4105(89)90011-9).

Mydland, S.; Yusra, I.; Whitson, C.H. et al. 2020. Gas EOR Processes in Tight Unconventionals. SPE-200396-MS. SPE Improved Oil Recovery Conference, 31 August - 4 September, Tulsa, Oklahoma, USA. <https://doi.org/10.2118/200396-MS>.

National Institute of Standards and Technology (NIST). Thermochemical Properties of Fluid Systems; <http://webbook.nist.gov/chemistry> (accessed April to June 2019).

NEB, AER, BC OGC, BC MNGD. 2013. The Ultimate Potential for Unconventional Petroleum from the Montney Formation of British Columbia and Alberta - Energy Briefing Note. <https://www.cer-rec.gc.ca/nrg/sttstc/ntrlgss/rprt/lmtptntlmntnyfrmtn2013/lmtptntlmntnyfrmtn2013-eng.html> (accessed on 1 January 2020).

Negin, C.; Ali, S.; Xie, Q. 2017. Most common surfactants employed in chemical enhanced oil recovery. *Petroleum* 3, 197-211. <http://dx.doi.org/10.1016/j.petlm.2016.11.007>.

Nelson, C.W.; Hilliard, C.; Kalantar, T.H. et al. 2018. A Novel High Throughput Screening Approach for Flowback Aid Optimization. SPE International Conference and Exhibition on Formation Damage Control, 7-9 February, Lafayette, Louisiana, USA. SPE-189552-MS. <https://doi.org/10.2118/189552-MS>.

Nelson, P. H. 2009. Pore-Throat Sizes in Sandstones, Tight Sandstones, and Shales. *AAPG Bull* 93 (3): 329–340. <https://doi.org/10.1306/10240808059>.

Nojabaei, B.; Johns, R.T.; Chu, L. 2013. Effect of Capillary Pressure on Phase Behavior in Tight Rocks and Shales. *SPE Res Eval & Eng*, 16 (03). <https://doi.org/10.2118/159258-PA>.

Oloredé, O.M.; Akkutlu, I.Y; Efendiev, Y. 2017. Compositional Reservoir-Flow Simulation for Organic-Rich Gas Shale. *SPE J.*, 22(06). SPE-182667-PA. <https://doi.org/10.2118/182667-PA>.

Orozco, D.; Fragoso, A.; Selvan, K. et al. 2020. Eagle Ford Huff-and-Puff Gas Injection Pilot: Comparison of Reservoir Simulation, Material Balance and Real Performance

of the Pilot Well. *SPE Res Eval & Eng*, 23(01). SPE-191575-PA.
<https://doi.org/10.2118/191575-PA>.

Orr, F. M. Jr. 2007. Theory of Gas Injection Processes. Tie-line Publications.

Ozkan, E.; Raghavan, R.S; Apaydin, O.G. 2010. Modeling of fluid transfer from shale matrix to fracture network. SPE Annual Technical Conference and Exhibition, 19-22 September, Florence, Italy. SPE-134830-MS. <https://doi.org/10.2118/134830-MS>.

Pacheco-Roman, F.J. and Hejazi, S.H. 2015. Estimation of Solubility and Diffusivity of Gases in Heavy Oils by Use of Late-Time Pressure-Decay Data: An Analytical/Graphical Approach. *SPE J*, 20 (04): 717-728. SPE-170957-PA.
<https://doi.org/10.2118/170957-PA>.

Palisch, T.; Duenckel, R.; Bazan, L. et al. 2007. Determining Realistic Fracture Conductivity and Understanding Its Impact on Well Performance-Theory and Field Examples. SPE Hydraulic Fracturing Technology Conference, 29-31 January, College Station, Texas, U.S.A. SPE-106301-MS. <https://doi.org/10.2118/106301-MS>.

Parmar, J.S.; Dehghanpour, H.; Kuru, E. 2014. Displacement of water by gas in propped fractures: Combined effects of gravity, surface tension, and wettability. *Journal of Unconventional Oil and Gas Resources*, 5: 10-21.
<https://doi.org/10.1016/j.juogr.2013.11.005>.

Pedersen, K. S.; Christensen, P. L; Shaikh, J. A. 2015. Phase Behavior of Petroleum Reservoir Fluids. Second Edition. CRC Press, Taylor & Francis Group, Boca Raton, FL, USA. <https://doi.org/10.1201/b17887>.

Pedersen, K. S.; Thomassen, P.; and Fredenslund, A. 1985. Thermodynamics of Petroleum Mixtures Containing Heavy Hydrocarbons. 3. Efficient Flash Calculation Procedures Using the SRK Equation of State. *Ind. Eng. Chem. Process Des. Dev.* 24 (4): 948–954. <https://doi.org/10.1021/i200031a009>.

Peneloux, A.; Rauzy, E.; Freze, R. 1982. A Consistent Correlation for Redlich-Kwong-Soave Volumes. *Fluid Phase Equilibria*, 8. 7. [https://doi.org/10.1016/0378-3812\(82\)80002-2](https://doi.org/10.1016/0378-3812(82)80002-2).

Peng, D. Y. and Robinson, D. B. 1978. The Characterization of the Heptanes and Heavier Fractions for the GPA Peng-Robinson Programs. GPA Research Report RR-28, Gas Producers Association, Tulsa.

Perez F. and Devegowda, D. 2020. Molecular Signatures of Solvent Injection in Shale Organic Nanopores. SPE-200307-MS. SPE Improved Oil Recovery Conference, 31 August - 4 September, Tulsa, Oklahoma, USA. <https://doi.org/10.2118/200307-MS>.

Perkins, T.K. and Johnston, O.C. 1963. A Review of Diffusion and Dispersion in Porous Media. *SPE J.* 3 (1). SPE-480-PA. <https://doi.org/10.2118/480-PA>.

Peters, E.J. 2012. Advanced Petrophysics: Volume 2: Dispersion, Interfacial Phenomena/Wettability, Capillarity/Capillary Pressure, Relative Permeability. Chap. 7, 7-62. Live Oak Book Company.

Pope, G. A. 1980. The Application of Fractional Flow Theory to Enhanced Oil Recovery. *SPE J.* 20(3). SPE-7660-PA. <https://dx.doi.org/10.2118/7660-PA>.

Rabie, A.; Zhou, J.; Qu, Qi. 2019. Evaluation of a New Environmentally Friendly Flowback Surfactant and Its Application to Enhance Oil and Gas Productivity.

SPE Middle East Oil and Gas Show and Conference, 18-21 March, Manama, Bahrain. SPE-195045-MS. <https://doi.org/10.2118/195045-MS>.

Ramirez, J.F. and Aguilera, R. 2016. Factors Controlling Fluid Migration and Distribution in the Eagle Ford Shale. *SPE Res Eval & Eng* 19(03). SPE-171626-PA. <https://dx.doi.org/10.2118/171626-PA>.

Rao, D.N. 1997. New Technique of Vanishing Interfacial Tension for Miscibility Determination. *Fluid Phase Equilibria* 139 (1): 311-324. [https://doi.org/10.1016/S0378-3812\(97\)00180-5](https://doi.org/10.1016/S0378-3812(97)00180-5).

Rasmussen, M.L. and Civan, F. 2009. Parameters of Gas Dissolution in Liquids Obtained by Isothermal Pressure Decay. *AICHE J*, 55(1). <https://doi.org/10.1002/aic.11669>.

Rassenfoss, S. 2017. Shale EOR Works, But Will It Make a Difference? *JPT* 69(10). SPE-1017-0034-JPT. <https://doi.org/10.2118/1017-0034-JPT>.

Reynolds, M.; Bachman, R.; Buendia, J. et al. 2015. The Full Montney - A Critical Review of Well Performance by Production Analysis of Over 2,000 Montney Multi-Stage Fractured Horizontal Gas Wells. SPE/CSUR Unconventional Resources Conference, 20-22 October, Calgary, Alberta, Canada. SPE-175948-MS. <https://dx.doi.org/10.2118/175948-MS>.

Rezende, F.C.; Rabelo, R.B.; Kinouti, L. et al. 2019. Tailoring Alkoxylation of Flowback Aid Surfactants for Maximum Efficiency. SPE International Conference on Oilfield Chemistry, 8-9 April, Galveston, Texas, USA. SPE-193623-MS. <https://doi.org/10.2118/193623-MS>.

Riazi, M. R. 2005. Characterization and Properties of Petroleum Fractions, first edition. Philadelphia, Pennsylvania: American Society for Testing and Materials.

- Sadrzadeh, M; Amirilargani, M.; Shahidi, K. 2009. Pure and mixed gas permeation through a composite polydimethylsiloxane membrane. *Polym. Adv. Technol.*, 22: 586–597. <https://doi.org/10.1002/pat.1551>.
- Salman, A.; Kurtoglu, B.; Kazemi, H. 2014. Analysis of Chemical Tracer Flowback in Unconventional Reservoirs. SPE-171656-MS. SPE/CSUR Unconventional Resources Conference – Canada, 30 September–2 October, Calgary, Alberta, Canada. <https://doi.org/10.2118/171656-MS>.
- Sanchez-Rivera, D; Mohanty, K.; Balhoff, M. 2015. Reservoir simulation and optimization of Huff-and-Puff operations in the Bakken Shale. *Fuel*, 147:82-94. <https://doi.org/10.1016/j.Fuel.2014.12.062>.
- Senters, C.W.; Warren, M.N.; Squires, C.L. et al. 2015. Reducing Costs and Optimizing Drilling and Completion Efficiencies in Unconventional Plays Using Completion Diagnostics. SPE-174844-MS. SPE Annual Technical Conference and Exhibition, 28-30 September, Houston, Texas, USA. <https://doi.org/10.2118/174844-MS>.
- Shaoul, J.; Zelm, L.V.; Pater, C.J.D. 2011. Damage Mechanisms in Unconventional-Gas-Well Stimulation - a New Look at an Old Problem. *SPE Prod & Oper*, 26, 388–400. <https://dx.doi.org/10.2118/142479-PA>.
- Sharma, M. and Agrawal, S. 2013. Impact of Liquid Loading in Hydraulic Fractures on Well Productivity. SPE Hydraulic Fracturing Technology Conference, 4-6 February, The Woodlands, Texas, USA. SPE-163837-MS. <https://dx.doi.org/10.2118/163837-MS>.
- Sheikha, H.; Mehrotra, A.K.; Pooladi-Darvish, M. 2006. An inverse solution methodology for estimating the diffusion coefficient of gases in Athabasca bitumen from pressure-

- decay data. *Journal of Petroleum Science and Engineering*, 53(3-4):189–202. <https://doi.org/10.1016/j.petrol.2006.06.003>.
- Shen, L; Chen, Z. 2007. Critical review of the impact of tortuosity on diffusion. *Chem Eng Sci* 62: 3748 – 3755. <https://doi.org/10.1016/j.ces.2007.03.041>.
- Sheng, J. J. 2017. Critical Review of Field EOR Projects in Shale and Tight Reservoirs. *Journal of Petroleum Science and Engineering*, Volume 159: 654-665. <https://doi.org/10.1016/j.petrol.2017.09.022>.
- Sing, K.S.W.; Everett, D.H.; Haul, R.A.W. et al. 1985. IUPAC commission on colloid and surface chemistry including catalysis. *Pure and Applied Chemistry* 57(4), 603–619. <http://dx.doi.org/10.1351/pac198557040603>.
- Song, C. and Yang, D. 2017. Experimental and numerical evaluation of CO₂ huff-n-puff processes in Bakken formation. *Fuel* 190: 145–162. <https://doi.org/10.1016/j.Fuel.2016.11.041>.
- Tagavifar, M.; Balhoff, M.; Mohanty, K. et al. 2019. Dynamics of Low-Interfacial-Tension Imbibition in Oil-Wet Carbonates. *SPE J.* 24(03). SPE-194194-PA. <https://dx.doi.org/10.2118/194194-PA>.
- Teklu, T.W.; Alharthy, N.; Kazemi, H. et al. 2014. Phase Behavior and Minimum Miscibility Pressure in Nanopores. *SPE Res Eval & Eng*, 17 (03). <https://doi.org/10.2118/168865-PA>.
- Thakur, G. 2019. Enhanced Recovery Technologies for Unconventional Oil Reservoirs. *JPT* 71(09). SPE-0919-0066-JPT. <https://doi.org/10.2118/0919-0066-JPT>.

Twu, C. H. 1983. Prediction of Thermodynamic Properties of Normal Paraffins Using Only Normal Boiling Point. *Fluid Phase Equilibr.* 11 (1): 65–81. [https://doi.org/10.1016/0378-3812\(83\)85006-7](https://doi.org/10.1016/0378-3812(83)85006-7).

U.S. Energy Information Administration (EIA). 2016. Trends in U.S. Oil and Natural Gas Upstream Costs. March 2016. <https://www.eia.gov/analysis/studies/drilling/pdf/upstream.pdf>.

U.S. Energy Information Administration (EIA). 2019. Annual Energy Outlook 2019 With Projections to 2050. January 2019. <https://www.eia.gov/outlooks/aeo/pdf/aeo2019.pdf>.

Ullman, W.J., Aller, R.C., 1982. Diffusion Coefficients in Near Shore Marine Sediments. Limnology Oceanography 27: 552–556. <https://doi.org/10.4319/lo.1982.27.3.0552>.

Wan, T. 2015. Investigation of EOR Performance in Shale Oil Reservoirs by Cyclic Gas Wang, Y. and Orr, FM. Jr. 1997. Analytical calculation of minimum miscibility pressure. *Fluid Phase Equilibria* 139 (1-2): 101-124. [https://doi.org/10.1016/S0378-3812\(97\)00179-9](https://doi.org/10.1016/S0378-3812(97)00179-9).

Whitson, C.H. 1983. Characterizing Hydrocarbon Plus Fractions. *SPE J.* 23(04). <https://doi.org/10.2118/12233-PA>.

Whitson, C.H. and Brulé, M.R. 2000. Phase Behavior. Monograph Series, Society of Petroleum Engineer, Richardson, Texas.

Wijaya, N.; Sheng, J. J. 2020. Shut-In Effect in Removing Water Blockage in Shale-Oil Reservoirs with Stress-Dependent Permeability Considered. *SPE Res Eval & Eng*, 23(01). SPE-195696-PA. <https://dx.doi.org/10.2118/195696-PA>.

Wood, D.J.; Lake, L.W.; Johns, R. T. et al. 2008. A Screening Model for CO₂ Flooding and Storage in Gulf Coast Reservoirs Based on Dimensionless Groups. *SPE Res Eval & Eng* 11 (3). SPE-100021-PA. <https://doi.org/10.2118/100021-PA>.

Xu, W.; Ayirala, S.C.; Rao, D.N. 2008. Measurement of Surfactant-Induced Interfacial Interactions at Reservoir Conditions. *SPE Res & Eval*, 11(01). SPE-96021-PA. <https://doi.org/10.2118/96021-PA>.

Xu, L. and Fu, Q. 2012. Ensuring Better Well Stimulation in Unconventional Oil and Gas Formations by Optimizing Surfactant Additives. SPE-154242-MS. SPE Western Regional Meeting, 21-23 March, Bakersfield, California, USA. <https://doi.org/10.2118/154242-MS>.

Yaich, E.; Williams, S.; Bowser, A. et al. 2015. A Case Study: The Impact of Soaking on Well Performance in the Marcellus. URTEC-2154766-MS. Unconventional Resources Technology Conference, 20-22 July, San Antonio, Texas, USA. <https://doi.org/10.15530/URTEC-2015-2154766>.

Yarveicy, H.; Habibi, A.; Pegov, S. et al. 2018. Enhancing Oil Recovery by Adding Surfactants in Fracturing Water: A Montney Case Study. SPE Canada Unconventional Resources Conference, 13-14 March, Calgary, Alberta, Canada. SPE-189829-MS. <https://dx.doi.org/10.2118/189829-MS>.

Yassin, M.; Habibi, A.; Eghbali, S. et al. 2018. An Experimental Study of Non-Equilibrium CO₂-Oil Interactions. *SPE J.*, 23(05). SPE-187093-PA. <https://doi.org/10.2118/187093-PA>.

Yellig, W.F., and Metcalfe, R.S. 1980. Determination and Prediction of CO₂ Minimum Miscibility Pressures. *J. Pet. Tech*, 32 (01): 160–168. SPE-7477-PA. <https://doi.org/10.2118/7477-PA>.

Yu, W.; Lashgari, H.R.; Wu, K. et al. 2015. CO₂ injection for enhanced oil recovery in Bakken tight oil reservoirs. *Fuel*, 159:354–363.
<http://dx.doi.org/10.1016/j.Fuel.2015.06.092>.

Yu, Y.; Li, L.; Sheng, J.J. 2017. A comparative experimental study of gas injection in shale plugs by flooding and huff-n-puff processes. *Journal of Natural Gas Science and Engineering* 38: 195-202. <http://dx.doi.org/10.1016/j.jngse.2016.12.040>.

Yue, Z.; Peng, Y.; He, K. et al. 2016. Multifunctional Fracturing Additives as Flowback Aids. SPE Annual Technical Conference and Exhibition, 26-28 September, Dubai, UAE. SPE-181383-MS. <https://doi.org/10.2118/181383-MS>.

Zhang, K.; Nojabaei, B.; Ahmadi, K. et al. 2018. Minimum Miscibility Pressure Calculation for Oil Shale and Tight Reservoirs with Large Gas-Oil Capillary Pressure. URTEC-2901892-MS. SPE/AAPG/SEG Unconventional Resources Technology Conference, 23-25 July, Houston, Texas, USA.
<https://dx.doi.org/10.15530/URTEC-2018-2901892>.

Zhang, Y.; Lashgari, H.R; Di, Y. et al. 2017. Capillary pressure effect on phase behavior of CO₂/hydrocarbons in unconventional reservoirs. *Fuel* 197, 575–582.
<http://dx.doi.org/10.1016/j.Fuel.2017.02.021>.

Zhang, Y.P; Hyndman, C.L.; Maini, B.B. 2000. Measurement of gas diffusivity in heavy oils. *J. Pet. Sci. Eng.* 25: 37–47. [https://doi.org/10.1016/S0920-4105\(99\)00031-5](https://doi.org/10.1016/S0920-4105(99)00031-5).

Zhao, B.; Panthi, K.; Mohanty, K.K. 2019. Tracer Eluting Proppants for Shale Fracturing. URTEC-2019-478-MS. SPE/AAPG/SEG Unconventional Resources Technology Conference, 22-24 July, Denver, Colorado, USA.
<https://doi.org/10.15530/urtec-2019-478>.

Zhou, X.; N. R. Morrow; S. Ma. 2000. Interrelationship of Wettability, Initial Water Saturation, Aging Time, and Oil Recovery by Spontaneous Imbibition and Waterflooding. *SPE J.* 5(2): 199-207. SPE-62507-PA.
<https://dx.doi.org/10.2118/62507-PA>.

Zhou, Z.; Hoffman, T.; Bearinger, D. et al. 2016. Experimental and Numerical Study on Spontaneous Imbibition of Fracturing Fluids in the Horn River Shale Gas Formation. *SPE Drill & Compl.* 31(03). SPE-171600-PA.
<https://doi.org/10.2118/171600-PA>.

Zick, A. A. 1986. A Combined Condensing/Vaporizing Mechanism in the Displacement of Oil by Enriched Gas. Paper presented at the SPE Annual Technical Conference and Exhibition, New Orleans, Louisiana, USA, 5–8 October. SPE-15493-MS.
<https://doi.org/10.2118/15493-MS>.

Appendices

Appendix A. Oil Compositional Analysis, Measured Density Data, One- and Two-PC PR-EOS Calibration, and Two-Phase Equilibrium Data of Different PR-EOS Models

A1. Montney Oil Composition and Measured Oil Density at Different Pressures and Temperatures

Please see Tables A-1 and A-2.

Table A-1: Compositional analysis of Montney oil from the simulated distillation method

Carbon Number	T_b (°C)	wt%	Carbon Number	T_b (°C)	wt%
5	36	1.79	50	575	0.64
6	69	3.34	52	584	0.57
7	98	2.99	54	592	0.53
8	126	5.42	56	600	0.47
9	174	12.88	58	608	0.4
10	196	5.71	60	615	0.39
12	216	4.96	62	622	0.35
14	254	9.18	64	629	0.31
16	287	7.07	66	635	0.27
18	316	6.49	68	641	0.26
20	344	5.05	70	647	0.24
22	369	4.45	72	653	0.22
24	391	3.63	74	658	0.2
26	412	3.29	76	664	0.17
28	431	2.99	78	670	0.17
30	449	2.56	80	675	0.16

32	466	2	82	681	0.14
34	481	1.88	84	686	0.14
36	496	1.73	86	691	0.12
38	509	1.36	88	695	0.11
40	522	1.34	90	700	0.11
42	534	0.96	92	704	0.1
44	545	1.01	94	708	0.1
46	556	0.74	96	712	0.1
48	566	0.73	98	716	0.09
			100+	...	0.09

Table A-2: Measured density of oil at different pressures and temperatures

T (°C)	P (bar)	Density (kg/m ³)
30.7	276	840.71
30.6	207	837.81
30.5	138	834.35
30.6	103	832.88
30.7	69	831.82
30.6	35	829.90
30.6	21	829.26
30.5	7	827.75
30.8	1	827.50
50.2	276	832.86
50.1	207	829.87
50.0	138	826.32
49.9	104	824.61
49.9	69	823.02
50.0	35	821.24
50.1	21	820.05
50.1	7	818.82
50.1	1	818.50
70.3	276	823.87
70.3	207	820.06
70.4	138	817.00

70.5	104	815.61
70.4	69	813.95
70.5	34	811.30
70.5	21	810.17
70.6	7	809.04
70.2	1	806.50

A2. Correlations Used for the PR-EOS Calibration (Eghbali and Dehghanpour 2018)

The specific gravity (SG) of pseudocomponents (PCs) (Riazi 2005) is calculated using

$$SG_i = 1.07 - e^{(3.56073 - 2.93886 MW_i^{0.1})} \quad (A-1)$$

The SG of the plus fraction (Alboudwarej et al. 2006) is calculated using

$$SG_{C+} = 670 MW_{C+}^{0.0629} \quad (A-2)$$

The boiling temperature (K) of PCs (Riazi 2005) is calculated using

$$T_{b,i} = 1090 - e^{(6.9955 - 0.11193 CN_i^{2/3})} \quad (A-3)$$

The boiling temperature (K) of the plus fraction (Pedersen et al. 1985) is calculated using

$$T_{b,C+} = 97.58 \times MW_{C+}^{0.3323} \times SG_{C+}^{0.04609} \quad (A-4)$$

The critical temperature (Lee and Kesler 1975) is calculated using

$$T_{c,i} = 341.7 + 811 SG_i + (0.4244 + 0.1174 SG_i) T_{b,i} + \frac{(0.4669 - 3.2623 SG_i) \times 10^5}{T_{b,i}} \quad (A-5)$$

The critical pressure (Lee and Kesler 1975) is calculated using

$$P_{c,i} = \exp \left[8.3634 - \frac{0.0566}{SG_i} - \left(0.24244 + \frac{2.2898}{SG_i} + \frac{0.11857}{SG_i^2} \right) \times 10^{-3} \times T_{b,i} \right. \\ \left. + \left(1.4685 + \frac{3.648}{SG_i} + \frac{0.47227}{SG_i^2} \right) \times 10^{-7} \times T_{b,i}^2 - (0.42019 \right. \\ \left. + \frac{1.6977}{SG_i^2}) \times 10^{-10} \times T_{b,i}^3 \right] \quad (\text{A-6})$$

The acentric factor (Lee and Kesler 1975) is calculated using

$$\omega_i = \begin{cases} \frac{\ln(P_{br,i}) - 5.92714 + \frac{6.09648}{T_{br,i}} + 1.28862 \ln(T_{br,i}) - 0.169347 \times T_{br,i}^6}{15.2518 - \frac{15.6875}{T_{br,i}} - 13.4721 \ln(T_{br,i}) + 0.4357 \times T_{br,i}^6} & \text{for } T_{br,i} \leq 0.8 \\ -7.904 + 0.1352K_{w,i} - 0.007465K_{w,i}^2 + 8.359T_{br,i} + \frac{(1.408 - 0.01063K_{w,i})}{T_{br,i}} & \text{for } T_{br,i} > 0.8 \end{cases} \quad (\text{A-7})$$

where $P_{br,i} = \frac{P_{b,i}}{P_{c,i}}$ and $T_{br,i} = \frac{T_{b,i}}{T_{c,i}}$ and where P_b is the pressure at which T_b is measured (e.g., the normal boiling point at 14.7 psia). The pressure and temperature are in psia and R, respectively. $K_{w,i}$ is the Watson characterization factor,

$$K_{w,i} = \frac{(1.8T_b)^{1/3}}{SG} \quad (\text{A-8})$$

The critical volume (Twu 1983) is calculated using

$$V_c = [1 - (0.419869 - 0.505839\psi_i - 1.56436\psi_i^3 - 9481.70\psi_i^{14})]^{-8} \quad (\text{A-9})$$

$$\text{with } \psi_i = 1 - \frac{T_{b,i}}{T_{c,i}}$$

The mixing rule for estimating the critical properties of PCs is

$$T_{c,k} = \frac{\sum_{i=m}^{i=n} z_i MW_i T_{c,i}}{\sum_{i=m}^{i=n} z_i MW_i} \quad (\text{A-10})$$

$$P_{c,k} = \frac{\sum_{i=m}^{i=n} z_i MW_i P_{c,i}}{\sum_{i=m}^{i=n} z_i MW_i} \quad (\text{A-11})$$

$$\omega_{c,k} = \frac{\sum_{i=m}^{i=n} z_i MW_i \omega_{c,i}}{\sum_{i=m}^{i=n} z_i MW_i} \quad (\text{A-12})$$

A3. Optimized BIP, Properties of the PCs, and P_{sat} Regression of One- and Two-PC EOS Models

Please see Tables A-3 through A-8.

Table A-3: Optimized BIP values for one-PC EOS model

	C ₁	C ₂	PC
C ₁			
C ₂		0	
PC	0.001	0.002	

Table A-4: Properties of the components in one-PC EOS model

Component	z_i	MW	P_c (bar)	T_c (°C)	ω	V_c (cm ³ /mol)
C ₁	0	16.04	46.00	-82.55	0.008	99.00
C ₂	0	30.07	48.84	32.25	0.098	148.00
PC	100	185.54	14.13	353.92	0.616	983.44

Table A-5: Experimental and predicted P_{sat} using one-PC EOS model

Mol% C ₁ /C ₂ in gas/oil mixture	Mol% C ₂ in C ₁ /C ₂ mixture	Experimental P_{sat} (bar)	Predictions from EOS Model P_{sat} (bar)
69.8	100	38.61	36.96
71.2	70	71.77	74.60
71.0	50.4	104.73	101.90
72.0	30.3	134.31	136.79
AARD (%)			3.20

Table A-6: Optimized BIP values for two-PC EOS model

C ₁	PC'₁	PC'₂
C ₁		
PC'₁	0	
PC'₂	0.0025	0

Table A-7: Properties of the components in two-PC EOS model

Component	z_i	MW	P_c (bar)	T_c (°C)	ω	V_c (cm ³ /mol)
C ₁	0	16.04	46.00	-82.55	0.008	99.00
PC'₁	27.70	90.29	29.99	260.48	0.314	382.801
PC'₂	72.30	222.02	12.27	404.37	0.693	1077.03

Table A-8: Experimental and predicted P_{sat} using two-PC EOS model

Mol% C ₁ in C ₁ /oil mixture	Experimental P_{sat} (bar)	Predictions from EOS Model P_{sat} (bar)
10.3	22.06	17.79
29.5	58.54	57.36
49.4	113.07	112.45
70.0	227.87	214.08
AARD (%)		6.97

A4. Two-Phase Equilibrium Data Using Four-, Two-, and One-PC EOS Models

Please see Tables A-9 and A-10 and Figure A-1.

Table A-9: Two-phase equilibrium data using the four-PC EOS model with Compositions 1 through 4 for the oil/C₁ systems and Compositions 5 through 8 for the oil/C₁/C₂ systems

Composition 1					Composition 5				
	z_1	Vapor	Liquid	K-values		z_1	Vapor	Liquid	K-values
C ₁	70.000	99.471	57.159	1.74025	C ₁	68.300	90.131	51.662	1.74464
PC1	12.945	0.500	18.368	0.02720	C ₂	10.700	9.294	11.772	0.78949
PC2	8.459	0.026	12.133	0.00211	PC1	8.945	0.531	15.358	0.03458
PC3	5.589	0.003	8.023	0.00042	PC2	6.459	0.036	11.354	0.00320
PC4	3.007	0.000	4.316	0.00011	PC3	4.589	0.007	8.082	0.00090
					PC4	1.007	0.001	1.773	0.00034
Composition 2					Composition 6				
	z_1	Vapor	Liquid	K-values		z_1	Vapor	Liquid	K-values
C ₁	77.000	99.471	57.211	1.73866	C ₁	78.066	93.950	50.314	1.86728
PC1	10.000	0.501	18.365	0.02726	C ₂	5.982	5.444	6.922	0.78653
PC2	6.000	0.024	11.263	0.00212	PC1	7.922	0.567	20.770	0.02732
PC3	5.000	0.004	9.400	0.00042	PC2	5.442	0.033	14.894	0.00218
PC4	2.000	0.000	3.761	0.00011	PC3	2.582	0.005	7.082	0.00077
					PC4	0.007	0.000	0.018	0.00040
Composition 3					Composition 7				

	z_i	Vapor	Liquid	K-values
C ₁	68.500	99.438	54.833	1.81347
PC1	15.000	0.532	21.391	0.02486
PC2	10.000	0.026	14.406	0.00184
PC3	5.000	0.003	7.207	0.00045
PC4	1.500	0.000	2.162	0.00015
Composition 4				
	z_i	Vapor	Liquid	K-values
C ₁	58.698	99.443	56.537	1.75889
PC1	18.885	0.528	19.859	0.02658
PC2	12.087	0.026	12.726	0.00204
PC3	6.574	0.003	6.922	0.00043
PC4	3.756	0.000	3.956	0.00012

	z_i	Vapor	Liquid	K-values
C ₁	88.000	97.541	54.193	1.79988
C ₂	2.000	1.875	2.443	0.76756
PC1	5.000	0.552	20.761	0.02658
PC2	3.000	0.028	13.531	0.00206
PC3	1.500	0.004	6.802	0.00052
PC4	0.500	0.000	2.270	0.00018
Composition 8				
	z_i	Vapor	Liquid	K-values
C ₁	52.000	84.795	50.595	1.67595
C ₂	18.000	14.600	18.146	0.80460
PC1	12.000	0.550	12.491	0.04405
PC2	9.000	0.045	9.384	0.00480
PC3	6.000	0.009	6.257	0.00137
PC4	3.000	0.002	3.128	0.00051

Table A-10: Two-phase equilibrium data using a two-PC EOS model with Compositions 9 through 12 for the oil/C₁ systems and the one-PC EOS model with Compositions 13 through 16 for the oil/C₁/C₂ systems

Composition 9					Composition 13				
	z_1	Vapor	Liquid	K-values		z_1	Vapor	Liquid	K-values
C ₁	92.000	94.348	91.456	1.03163	C ₁	60.500	70.898	60.471	1.17242
PC1	3.000	2.392	3.141	0.76148	C ₂	29.500	26.824	29.507	0.90907
PC2	5.000	3.260	5.403	0.60331	PC	10.000	2.278	10.022	0.22731
Composition 10					Composition 14				
	z_1	Vapor	Liquid	K-values		z_1	Vapor	Liquid	K-values
C ₁	94.000	96.933	89.559	1.08234	C ₁	63.000	73.621	60.792	1.21103
PC1	1.000	0.707	1.444	0.48963	C ₂	27.000	24.471	27.526	0.88902
PC2	5.000	2.360	8.997	0.26229	PC	10.000	1.909	11.682	0.16337
Composition 11					Composition 15				
	z_1	Vapor	Liquid	K-values		z_1	Vapor	Liquid	K-values
C ₁	93.000	95.853	90.275	1.06178	C ₁	66.000	76.704	61.411	1.24903
PC1	2.000	1.471	2.505	0.58720	C ₂	24.000	21.703	24.985	0.86865
PC2	5.000	2.676	7.219	0.37069	PC	10.000	1.593	13.604	0.11707
Composition 12					Composition 16				
	z_1	Vapor	Liquid	K-values		z_1	Vapor	Liquid	K-values
C ₁	90.500	97.554	89.200	1.09365	C ₁	75.000	85.438	64.100	1.33289
PC1	0.500	0.242	0.548	0.44171	C ₂	15.000	13.537	16.528	0.81907
PC2	9.000	2.205	10.252	0.21504	PC	10.000	1.025	19.372	0.05289

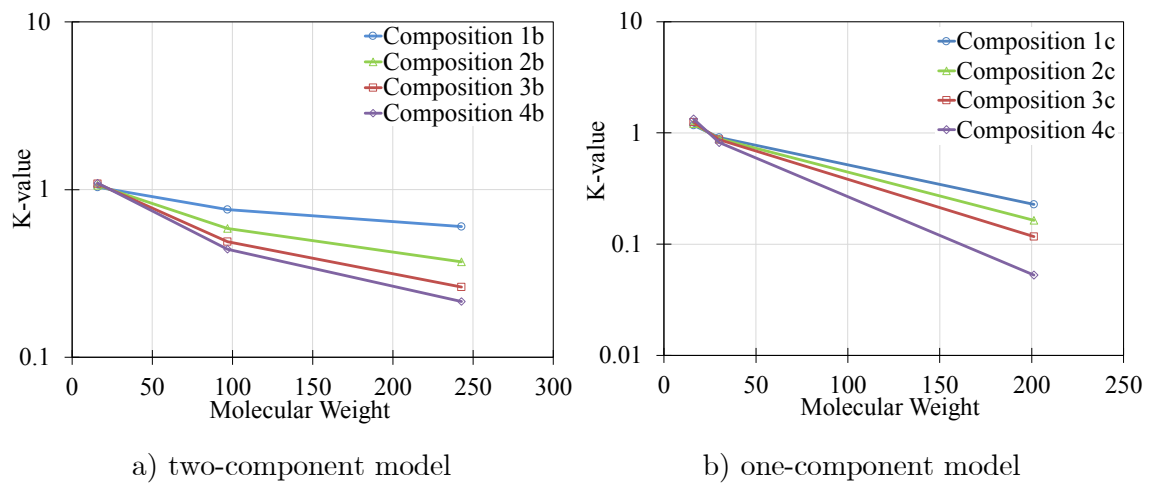


Figure A-1: Two-phase equilibrium K -values vs. MW of PCs in (a) two-PC EOS model and (b) one-PC EOS model at reservoir pressure and temperature of 137.89 bar and 50°C.

Appendix B. Supplementary Material, Pressure-Decline Data, and Summary of k -plane Data Clustering Method

B1. Supplementary Material

Supplementary material to Section 5.4.2 can be found online at <https://drive.google.com/file/d/1HRrTbDwe3hCbsFilkcJKXadoAU8o8Q1N/view?usp=sharing>.

B2. Pressure-Decline Data of Bulk-Phase and HnP Tests at $T = 50^\circ\text{C}$

Bulk-Phase Tests

Table B-1: Pressure-Decline Data of Oil/C₁ Test

Time (hour)	P (bar)	Time (hour)	P (bar)
0	137.59508	10.5	126.27994
0.5	135.26161	11	126.05980
1	134.29299	11.5	125.66355
1.5	133.76466	12	125.44341
2	132.97216	12.5	125.09119
2.5	132.04758	13	125.00313
3	131.51924	13.5	124.82702
3.5	131.16702	14	124.69494
4	130.63869	14.5	124.29869
4.5	130.15438	15	124.03452
5	129.58202	15.5	123.94647
5.5	129.18577	16	123.77036
6	128.92161	16.5	123.63827
6.5	128.70147	17	123.46216
7	128.17313	17.5	123.06591
7.5	127.99702	18	122.97786
8	127.73286	18.5	122.80175
8.5	127.42466	19	122.75772
9	127.07244	19.5	122.58161
9.5	126.85230	20	122.18536
10	126.50008	20.5	122.27341

21	122.14133	42	117.7386
21.5	121.92119	42.5	117.6065
22	121.83313	43	117.5184
22.5	121.61300	43.5	117.4822
23	121.43688	44	117.4304
23.5	121.12869	44.5	117.5624
24	120.99661	45	117.4744
24.5	121.04063	45.5	117.1662
25	120.96212	46	117.2543
25.5	120.82050	46.5	117.1222
26	120.64438	47	117.0968
26.5	120.46827	47.5	116.9901
27	120.51230	48	117.0781
27.5	120.29216	48.5	116.902
28	120.24813	49	116.7699
28.5	120.11605	49.5	116.902
29	119.98397	50	116.6819
29.5	119.89591	50.5	116.6149
30	119.67577	51	116.5938
30.5	119.61852	51.5	116.5058
31	119.54369	52	116.4177
31.5	119.41161	52.5	116.1976
32	119.27952	53	115.9334
32.5	119.36758	53.5	116.0215
33	119.10341	54	115.8454
33.5	119.0154	54.5	115.7133
34	118.9713	55	115.6252
34.5	119.1034	55.5	115.4931
35	118.8833	56	115.3611
35.5	118.6631	56.5	115.2734
36	118.6284	57	115.1409
36.5	118.6	57.5	114.9648
37	118.5311	58	114.8327
37.5	118.3549	58.5	114.7006
38	118.2669	59	114.6566
38.5	118.2229	59.5	114.5686
39	118.1788	60	114.6566
39.5	118.0908	60.5	114.5823
40	117.8266	61	114.4805
40.5	117.9147	61.5	114.2604
41	117.8266	62	114.3484
41.5	117.6065	62.5	114.3924

63	114.4365	65	114.22317
63.5	114.3924	65.5	114.27418
64	114.2604	66	114.09823
64.5	114.1723	66.5	114.16096
		67	114.12827
		67.5	114.07095

Table B-2: Pressure-Decline Data of Oil/C₁/C₂ Test

Time (hour)	P (bar)	Time (hour)	P (bar)
0	138.03536	15.5	117.0781
0.5	132.66397	16	116.902
1	130.85883	16.5	116.814
1.5	129.75813	17	116.6379
2	128.87758	17.5	116.3297
2.5	128.12911	18	116.0655
3	127.20452	18.5	115.8894
3.5	126.72022	19	115.7573
4	125.97175	19.5	115.5372
4.5	125.53147	20	115.273
5	124.87105	20.5	115.0529
5.5	124.29869	21	114.8327
6	123.68230	21.5	114.7887
6.5	123.41813	22	114.4365
7	123.06591	22.5	114.3924
7.5	122.53758	23	114.1283
8	122.09730	15.5	117.0781
8.5	121.65702	16	116.902
9	121.30480	16.5	116.814
9.5	120.77647	17	116.6379
10	120.60036	17.5	116.3297
10.5	120.02800	18	116.0655
11	119.89591	18.5	115.8894
11.5	119.45564	19	115.7573
12	119.19147	19.5	115.5372
12.5	118.97133	20	115.273
13	118.70716	20.5	115.0529
13.5	118.48702	21	114.8327
14	118.17883	21.5	114.7887
14.5	118.00272	22	114.4365
15	117.69452	22.5	114.3924
23	114.1283	44	109.1234

23.5	113.9962	44.5	109.1091
24	113.644	45	108.933
24.5	113.5999	45.5	109.0211
25	113.688	46	108.7569
25.5	113.2918	46.5	108.7129
26	112.9836	47	108.5808
26.5	112.9395	47.5	108.7569
27	112.8515	48	108.4927
27.5	112.7634	48.5	108.4047
28	112.4993	49	108.3519
28.5	112.3672	49.5	108.3166
29	112.4112	50	108.0965
29.5	112.0149	50.5	108.0084
30	112.059	51	108.1405
30.5	111.8388	51.5	107.9644
31	111.7508	52	107.7443
31.5	111.677	52.5	107.6562
32	111.5747	53	107.7002
32.5	111.4426	53.5	107.5241
33	111.3986	54	107.6562
33.5	111.3545	54.5	107.5103
34	111.2665	55	107.4361
34.5	111.0463	55.5	107.304
35	110.8702	56	107.1719
35.5	110.7822	56.5	107.2599
36	110.6941	57	107.1279
36.5	110.6061	57.5	107.0398
37	110.6941	58	107.0838
37.5	110.3859	58.5	107.1279
38	110.474	59	107.2159
38.5	110.2979	59.5	107.0838
39	110.0777	60	107.1279
39.5	110.0337	60.5	107.0398
40	109.9897	61	107.0838
40.5	110.0337	61.5	107.0398
41	109.6815	62	107.1719
41.5	109.5054	62.5	107.2159
42	109.4173	63	107.1531
42.5	109.3733	63.5	107.111
43	109.3293	64	107.0838
43.5	109.1531	64.5	107.1719
		65	106.9518

HnP Tests

Table B-3: Pressure-Decline Data of Set 1-C₁ Test

Time (hour)	<i>P</i> (bar)	Time (hour)	<i>P</i> (bar)
0	138.60772	17	136.992
0.5	138.22311	17.5	137.1681
1	138.04116	18	137.036
1.5	137.89748	18.5	137.1241
2	137.85924	19	137.0776
2.5	137.84388	19.5	137.036
3	137.75582	20	136.9384
3.5	137.66777	20.5	137.0408
4	137.71179	21	137.0694
4.5	137.62374	21.5	137.0336
5	137.55479	22	137.0165
5.5	137.55322	22.5	137.0005
6	137.50919	23	136.9901
6.5	137.43069	23.5	136.8944
7	137.34263	24	137.0145
7.5	137.43069	24.5	137.0003
8	137.40045	25	136.9824
8.5	137.34421	25.5	136.8972
9	137.38823	26	136.8504
9.5	137.40734	26.5	136.9384
10	137.32884	27	137.0265
10.5	137.28481	27.5	136.8504
11	137.37287	28	136.8944
11.5	137.28481	28.5	136.9824
12	137.37287	29	136.9384
12.5	137.31659	29.5	136.9824
13	137.21212	30	136.8504
13.5	137.12407	30.5	136.9384
14	137.16810	31	136.7623
14.5	137.25615	31.5	136.8944
15	137.30018	32	137.0265
15.5	137.14526	32.5	136.7623
16	137.12407	33	137.0265
16.5	137.03601	33.5	136.8504
34	137.0609	55	136.592
34.5	136.8404	55.5	136.7241
35	137.0609	56	136.8121

35.5	136.9729	56.5	136.7376
36	136.8408	57	136.7028
36.5	136.9289	57.5	136.592
37	137.0169	58	136.703
37.5	136.9047	58.5	136.8121
38	136.8848	59	136.6212
38.5	136.7087	59.5	136.5848
39	136.7968	60	136.7041
39.5	136.8848	60.5	136.636
40	136.9289	61	136.6401
40.5	136.8643	61.5	136.7681
41	136.7968	62	136.6801
41.5	136.7681	62.5	136.592
42	136.755	63	136.6144
42.5	136.7123	63.5	136.4944
43	136.6241	64	136.6265
43.5	136.592	64.5	136.5384
44	136.6801	65	136.6705
44.5	136.7241	65.5	136.5824
45	136.7016	66	136.5468
45.5	136.636	66.5	136.4944
46	136.6253	67	136.4011
46.5	136.6675	67.5	136.3183
47	136.6159	68	136.4944
47.5	136.548	68.5	136.398
48	136.8562	69	136.4874
48.5	136.6794	69.5	136.521
49	136.6241	70	136.4944
49.5	136.592	70.5	136.5597
50	136.548	71	136.5123
50.5	136.6642	71.5	136.6265
51	136.6381	72	136.4191
51.5	136.7681	72.5	136.3608
52	136.6801	73	136.4945
52.5	136.5539	73.5	136.3814
53	136.6361	74	136.4212
53.5	136.4599	74.5	136.3623
54	136.6683	75	136.2742
54.5	136.5785	75.5	136.2742
76	136.3183	97	136.4944
76.5	136.3946	97.5	136.3326
77	136.3623	98	136.4504

77.5	136.4357	98.5	136.2302
78	136.4876	99	136.2472
78.5	136.5384	99.5	136.1422
79	136.4952	100	136.1862
79.5	136.5074	100.5	136.4063
80	136.6265	101	136.3623
80.5	136.4504	101.5	136.4944
81	136.6265	102	136.4504
81.5	136.5384	102.5	136.2742
82	136.4903	103	136.3341
82.5	136.5824	103.5	136.4944
83	136.4944	104	136.3183
83.5	136.4609	104.5	136.5824
84	136.6705	105	136.3923
84.5	136.4504	105.5	136.4063
85	136.5824	106	136.4944
85.5	136.4504	106.5	136.3623
86	136.4282	107	136.2742
86.5	136.4154	107.5	136.3981
87	136.4063	108	136.4944
87.5	136.3623	108.5	136.3306
88	136.3183	109	136.3183
88.5	136.2302	109.5	136.2302
89	136.1862	110	136.3644
89.5	136.2551	110.5	136.1422
90	136.2468	111	136.3643
90.5	136.2004	111.5	136.2894
91	136.2707	112	136.1862
91.5	136.3066	112.5	136.2439
92	136.3183	113	136.2183
92.5	136.2657	113.5	136.2542
93	136.1862	114	136.0541
93.5	136.3001	114.5	136.1734
94	136.2742	115	136.1862
94.5	136.4944	115.5	136.2
95	136.3183	116	136.215
95.5	136.2924	116.5	136.2493
96	136.2706	117	136.3324
96.5	136.3924	117.5	136.4004
118	136.2742	139	136.2302
118.5	136.2451	139.5	136.1422
119	136.3183	140	136.1862

119.5	136.4944	140.5	136.2742
120	136.2302	141	136.2108
120.5	136.3623	141.5	136.1422
121	136.4944	142	136.1862
121.5	136.4504	142.5	136.0981
122	136.3183	143	136.2742
122.5	136.1422	143.5	136.3623
123	136.1301	144	136.1756
123.5	136.2051	144.5	136.2302
124	136.2309	145	136.2108
124.5	136.2742	145.5	136.1885
125	136.0981	146	136.2622
125.5	136.3503	146.5	136.3183
126	136.3011	147	136.2019
126.5	136.1933	147.5	136.1862
127	136.1422	148	136.1422
127.5	136.2302	148.5	136.1342
128	136.3183	149	136.1862
128.5	136.4944	149.5	136.0981
129	136.41	150	136.2624
129.5	136.3811	150.5	136.3183
130	136.3922	151	136.4063
130.5	136.4504	151.5	136.1862
131	136.3183	152	136.3057
131.5	136.3623	152.5	136.2862
132	136.2689	153	136.2441
132.5	136.2302	153.5	136.2302
133	136.3099	154	136.1422
133.5	136.2993	154.5	136.2651
134	136.3002	155	136.2002
134.5	136.3143	155.5	136.2742
135	136.242	156	136.1931
135.5	136.1862	156.5	136.1862
136	136.2412	157	136.17
136.5	136.3623	157.5	136.0981
137	136.1422	158	136.0771
137.5	136.4063	158.5	136.0541
138	136.374	159	136.2302
138.5	136.3183	159.5	136.1422
160	136.1551	165	136.2742
160.5	136.1862	165.5	136.3183
161	136.1181	166	135.9661

161.5	136.1422	166.5	136.1422
162	136.1848	167	136.0101
162.5	136.2033	167.5	136.1105
163	136.1862	168	136.0981
163.5	135.9661		
164	136.2307		
164.5	136.1422		

Table B-4: Pressure-Decline Data of Set 1-C₁/C₂ Test

Time (hour)	P (bar)	Time (hour)	P (bar)
0	138.53159	13.5	135.7811
0.5	137.78833	14	135.7684
1	137.39740	14.5	135.9943
1.5	136.99947	15	135.6936
2	136.89960	15.5	135.6496
2.5	136.73530	16	135.6496
3	136.72112	16.5	135.7376
3.5	136.66628	17	135.6936
4	136.64725	17.5	135.7376
4.5	136.73530	18	135.4294
5	136.70156	18.5	135.6978
5.5	136.47114	19	135.6056
6	136.12640	19.5	135.4735
6.5	136.30251	20	135.48
7	136.17043	20.5	135.3854
7.5	136.08237	21	135.1834
8	136.03834	21.5	135.0772
8.5	136.30011	22	135.2974
9	136.20864	22.5	134.8646
9.5	136.03253	23	135.1287
10	135.99930	23.5	134.9086
10.5	135.97035	24	134.9966
11	135.98850	24.5	134.8646
11.5	135.96921	25	134.8355
12	135.94447	25.5	134.6994
12.5	135.92707	26	134.7765
13	135.90045	26.5	134.6885
27	134.7325	48	134.122
27.5	134.8205	48.5	134.3085

28	134.6004	49	134.1974
28.5	134.6211	49.5	134.1952
29	134.6885	50	134.0047
29.5	134.7765	50.5	133.9607
30	134.8646	51	134.1368
30.5	134.7024	51.5	133.9613
31	134.6885	52	133.7791
31.5	134.7325	52.5	133.9835
32	134.3129	53	134.017
32.5	134.4328	53.5	133.9413
33	134.3218	54	133.9713
33.5	134.6242	54.5	133.9412
34	134.6902	55	133.8721
34.5	134.5984	55.5	134.0124
35	134.4398	56	133.9125
35.5	134.4506	56.5	133.9204
36	134.3873	57	134.0549
36.5	134.2066	57.5	133.9139
37	134.407	58	133.941
37.5	134.2347	58.5	133.9128
38	134.3244	59	133.8754
38.5	134.3372	59.5	134.0564
39	134.4958	60	133.9797
39.5	134.5068	60.5	133.7957
40	134.4567	61	133.8609
40.5	134.0814	61.5	133.9607
41	134.259	62	133.7842
41.5	134.2047	62.5	133.8286
42	134.1984	63	133.7405
42.5	134.2433	63.5	133.8286
43	134.3154	64	133.8286
43.5	134.2721	64.5	133.6965
44	134.3011	65	133.8726
44.5	134.2537	65.5	133.7405
45	134.2518	66	133.7506
45.5	134.1881	66.5	133.7846
46	134.3007	67	133.8084
46.5	134.2827	67.5	133.9167
47	134.2303	68	133.7846
47.5	134.1175	68.5	133.9167
69	133.8286	90	133.6856
69.5	133.8726	90.5	133.6085

70	133.7701	91	133.7846
70.5	133.832	91.5	133.7405
71	133.8726	92	133.6642
71.5	133.9167	92.5	133.6965
72	133.6525	93	133.5204
72.5	133.7906	93.5	133.5644
73	133.9421	94	133.6085
73.5	133.9607	94.5	133.6525
74	133.9167	95	133.5915
74.5	133.7846	95.5	133.5644
75	133.8286	96	133.7846
75.5	133.8286	96.5	133.5923
76	133.7846	97	133.6085
76.5	133.5204	97.5	133.6355
77	133.6525	98	133.7405
77.5	133.6612	98.5	133.5644
78	133.7005	99	133.4764
78.5	133.6085	99.5	133.6085
79	133.9167	100	133.6525
79.5	133.6085	100.5	133.671
80	134.0487	101	133.8286
80.5	133.9167	101.5	133.6085
81	133.7405	102	133.5644
81.5	133.7621	102.5	133.8286
82	133.7846	103	133.67
82.5	133.8726	103.5	133.6085
83	133.6965	104	133.8726
83.5	133.6525	104.5	133.7405
84	133.8726	105	133.7846
84.5	133.8101	105.5	133.6965
85	133.7405	106	133.5644
85.5	133.6525	106.5	133.8286
86	133.6085	107	133.4764
86.5	133.6323	107.5	133.7405
87	133.6704	108	133.7031
87.5	133.6965	108.5	133.5963
88	133.7405	109	133.5213
88.5	133.5204	109.5	133.5445
89	133.6144	110	133.514
89.5	133.5204	110.5	133.5903
111	133.7405	132	133.6085
111.5	133.6085	132.5	133.4323

112	133.51	133	133.5204
112.5	133.3883	133.5	133.5644
113	133.4323	134	133.5644
113.5	133.4688	134.5	133.5204
114	133.5644	135	133.5204
114.5	133.6085	135.5	133.6085
115	133.6525	136	133.4323
115.5	133.6965	136.5	133.6525
116	133.635	137	133.4323
116.5	133.7405	137.5	133.3883
117	133.7846	138	133.5204
117.5	133.5644	138.5	133.3883
118	133.6085	139	133.5204
118.5	133.5879	139.5	133.5204
119	133.5311	140	133.4323
119.5	133.4323	140.5	133.3883
120	133.5644	141	133.6085
120.5	133.7846	141.5	133.5644
121	133.6085	142	133.5204
121.5	133.5204	142.5	133.3883
122	133.5204	143	133.6525
122.5	133.6965	143.5	133.5204
123	133.7405	144	133.4764
123.5	133.6085	144.5	133.4323
124	133.6525	145	133.3443
124.5	133.5644	145.5	133.3883
125	133.6085	146	133.6085
125.5	133.6085	146.5	133.3003
126	133.5204	147	133.3922
126.5	133.5644	147.5	133.5204
127	133.6085	148	133.4562
127.5	133.5204	148.5	133.4906
128	133.4323	149	133.5644
128.5	133.5204	149.5	133.4712
129	133.6085	150	133.5644
129.5	133.5644	150.5	133.6085
130	133.6085	151	133.4764
130.5	133.6965	151.5	133.4323
131	133.6965	152	133.5204
131.5	133.6525	152.5	133.3003
153	133.4323	161	133.5505
153.5	133.4762	161.5	133.3366

154	133.6525	162	133.2234
154.5	133.4323	162.5	133.4509
155	133.6085	163	133.2151
155.5	133.3711	163.5	133.4391
156	133.3443	164	133.6133
156.5	133.5644	164.5	133.3306
157	133.6525	165	133.4924
157.5	133.6004	165.5	133.463
158	133.4323	166	133.2967
158.5	133.6112	166.5	133.4859
159	133.5711	167	133.3747
159.5	133.5713	167.5	133.3629
160	133.3192	168	133.3883
160.5	133.222		

Table B-5: Pressure-Decline Data of Set 2-C₁ Test

Time (hour)	P (bar)	Time (hour)	P (bar)
0	138.45255	11	137.2582
0.5	138.32123	11.5	137.2615
1	138.29969	12	137.2566
1.5	138.18830	12.5	137.2487
2	138.08910	13	137.3833
2.5	138.06530	13.5	137.3621
3	138.04408	14	137.3393
3.5	138.00908	14.5	137.3173
4	137.86522	15	137.3456
4.5	137.80471	15.5	137.3833
5	137.77108	16	137.2952
5.5	137.71528	16.5	137.2745
6	137.68775	17	137.2454
6.5	137.66536	17.5	137.2504
7	137.64079	18	137.2894
7.5	137.63043	18.5	137.2639
8	137.44074	19	137.2536
8.5	137.42733	19.5	137.22
9	137.38330	20	137.2012
9.5	137.36446	20.5	137.1912
10	137.33927	21	137.095
10.5	137.30729	21.5	137.0751
22	137.0606	43	136.97
22.5	137.0849	43.5	136.9871

23	137.0538	44	137.0311
23.5	137.0491	44.5	137.0082
24	137.0311	45	136.9297
24.5	137.059	45.5	136.9039
25	137.1632	46	136.881
25.5	137.1491	46.5	136.8956
26	137.123	47	136.943
26.5	137.1092	47.5	136.9245
27	137.0748	48	136.8981
27.5	137.1042	48.5	136.874
28	137.0806	49	136.855
28.5	137.0951	49.5	136.8774
29	137.1191	50	136.943
29.5	137.1031	50.5	136.9501
30	137.0751	51	136.9871
30.5	137.0801	51.5	136.9011
31	137.1191	52	136.7669
31.5	137.0651	52.5	136.7989
32	136.9871	53	137.1191
32.5	136.9701	53.5	137.0931
33	136.962	54	136.9871
33.5	136.9871	54.5	136.9821
34	137.0751	55	137.0751
34.5	137.0319	55.5	137.083
35	136.995	56	136.899
35.5	136.9871	56.5	136.8968
36	137.0311	57	137.1191
36.5	137.0581	57.5	137.123
37	137.1632	58	136.8109
37.5	137.1106	58.5	136.8138
38	137.0311	59	137.0752
38.5	137.0544	59.5	137.0731
39	137.1122	60	136.9871
39.5	137.1089	60.5	136.9861
40	137.0733	61	136.9142
40.5	137.0594	61.5	136.8994
41	136.9239	62	136.943
41.5	136.899	62.5	136.9612
42	137.021	63	136.9871
42.5	137.0751	63.5	136.9801
64	137.0751	85	136.899
64.5	137.0952	85.5	136.9101

65	137.1632	86	137.0311
65.5	137.1461	86.5	137.0177
66	137.0751	87	136.8822
66.5	137.051	87.5	136.9235
67	137.0311	88	137.0131
67.5	137.008	88.5	137.0244
68	136.855	89	136.9871
68.5	136.8701	89.5	136.9466
69	137.0751	90	136.8941
69.5	137.073	90.5	136.8507
70	136.8109	91	136.8676
70.5	136.8126	91.5	136.8308
71	136.893	92	136.9871
71.5	136.8989	92.5	136.966
72	136.855	93	136.8825
72.5	136.8501	93.5	136.855
73	136.8924	94	136.7499
73.5	136.913	94.5	136.7229
74	137.0311	95	136.7038
74.5	137.0581	95.5	136.719
75	136.9547	96	136.764
75.5	136.9386	96.5	136.7107
76	136.795	97	136.8109
76.5	136.7594	97.5	136.8055
77	136.7	98	136.8109
77.5	136.7369	98.5	136.8109
78	136.9412	99	136.7669
78.5	136.9871	99.5	136.7438
79	137.0312	100	136.7243
79.5	137.0751	100.5	136.7566
80	136.8989	101	136.8921
80.5	136.94	101.5	136.8749
81	137.0311	102	136.869
81.5	137.0117	102.5	136.849
82	136.9871	103	136.965
82.5	136.9767	103.5	136.9871
83	136.9413	104	136.748
83.5	136.9311	104.5	136.7229
84	136.9559	105	136.8982
84.5	136.9233	105.5	136.8721
106	136.8674	127	137.0751
106.5	136.835	127.5	137.0401

107	136.885	128	136.943
107.5	136.869	128.5	136.915
108	136.855	129	136.855
108.5	136.8371	129.5	136.8898
109	136.7529	130	137.0311
109.5	136.7101	130.5	137.008
110	136.7348	131	136.8982
110.5	136.7029	131.5	136.898
111	136.6982	132	136.8802
111.5	136.6789	132.5	136.879
112	136.8109	133	136.9421
112.5	136.8345	133.5	136.933
113	136.9422	134	136.8109
113.5	136.9271	134.5	136.7792
114	136.9011	135	136.7229
114.5	136.9371	135.5	136.8247
115	136.9001	136	136.943
115.5	136.868	136.5	136.9302
116	136.7669	137	136.855
116.5	136.7745	137.5	136.8378
117	136.8009	138	136.7669
117.5	136.8112	138.5	136.7445
118	136.8389	139	136.8009
118.5	136.873	139.5	136.8135
119	136.7669	140	136.7669
119.5	136.79	140.5	136.762
120	136.8882	141	136.7456
120.5	136.8982	141.5	136.75
121	136.8109	142	136.7089
121.5	136.8446	142.5	136.7027
122	136.9113	143	136.7211
122.5	136.943	143.5	136.6835
123	136.7669	144	136.699
123.5	136.7832	144.5	136.6683
124	136.8148	145	136.5908
124.5	136.8834	145.5	136.6118
125	136.855	146	136.6472
125.5	136.8976	146.5	136.6789
126	137.0311	147	136.7669
126.5	137.048	147.5	136.7306
148	136.7228	158	136.8925
148.5	136.72	158.5	136.9

149	136.7234	159	136.7607
149.5	136.7001	159.5	136.789
150	136.8549	160	136.8109
150.5	136.8525	160.5	136.841
151	136.6789	161	136.9671
151.5	136.6521	161.5	136.9153
152	136.5468	162	136.8912
152.5	136.5511	162.5	136.8942
153	136.7229	163	136.7968
153.5	136.7229	163.5	136.7669
154	136.6789	164	136.7229
154.5	136.6967	164.5	136.7413
155	136.7001	165	136.7462
155.5	136.7229	165.5	136.7276
156	136.855	166	136.754
156.5	136.852	166.5	136.7165
157	136.8701	167	136.7229
157.5	136.8434		

Table B-6: Pressure-Decline Data of Set 2-C₁/C₂ Test

Time (hour)	P (bar)	Time (hour)	P (bar)
0	138.38758	9	136.51882
0.5	138.07938	9.5	136.22974
1	138.01951	10	136.36182
1.5	137.84340	10.5	136.19341
2	137.49118	11	136.29287
2.5	137.35909	11.5	136.27376
3	137.10074	12	136.33009
3.5	136.89971	12.5	136.18571
4	136.98776	13	136.27565
4.5	136.81165	13.5	136.1417
5	136.67957	14	136.2239
5.5	136.65091	14.5	136.1168
6	136.58354	15	136.0823
6.5	136.56285	15.5	136.2144
7	136.51882	16	136.0383
7.5	136.55108	16.5	136.1703
8	136.40026	17	136.2009
8.5	136.38674	17.5	136.0823

18	136.1421	39	135.5041
18.5	135.9062	39.5	135.4329
19	135.9942	40	135.5481
19.5	135.8622	40.5	135.4601
20	135.9502	41	135.328
20.5	135.8512	41.5	135.284
21	135.5099	42	135.24
21.5	135.7301	42.5	135.1959
22	135.7741	43	135.24
22.5	135.8855	43.5	135.0638
23	135.8181	44	135.24
23.5	135.7114	44.5	135.1274
24	135.8123	45	135.1079
24.5	135.7683	45.5	135.24
25	135.4601	46	135.2026
25.5	135.625	46.5	135.1768
26	135.7243	47	135.1541
26.5	135.6802	47.5	135.0198
27	135.6362	48	135.0638
27.5	135.6199	48.5	135.0929
28	135.5922	49	135.1959
28.5	135.5741	49.5	135.0505
29	135.5481	50	135.0065
29.5	135.4601	50.5	134.9932
30	135.5102	51	134.9784
30.5	135.5241	51.5	134.9932
31	135.6802	52	134.9492
31.5	135.5922	52.5	135.1433
32	135.4601	53	135.1222
32.5	135.5139	53.5	135.1052
33	135.5042	54	135.1427
33.5	135.5964	54.5	135.1693
34	135.7243	55	134.8611
34.5	135.4681	55.5	135.1253
35	135.6362	56	135.0372
35.5	135.4161	56.5	135.0813
36	135.5041	57	135.1253
36.5	135.328	57.5	134.9624
37	135.4601	58	134.9052
37.5	135.5621	58.5	135.2134
38	135.4441	59	134.9901
38.5	135.4161	59.5	134.9052

60	135.0123	81	134.4522
60.5	134.9301	81.5	134.4898
61	134.9741	82	134.4901
61.5	135.0181	82.5	134.6659
62	134.842	83	134.5338
62.5	135.0622	83.5	134.4018
63	134.9836	84	134.524
63.5	134.9741	84.5	134.4229
64	134.9537	85	134.3768
64.5	135.0622	85.5	134.7291
65	134.8861	86	134.597
65.5	135.0622	86.5	134.685
66	134.842	87	134.4649
66.5	134.8176	87.5	134.5529
67	134.794	88	134.4438
67.5	134.7526	88.5	134.4209
68	134.798	89	134.5622
68.5	134.6659	89.5	134.2007
69	134.5338	90	134.5741
69.5	134.754	90.5	134.3768
70	134.4898	91	134.5089
70.5	134.6659	91.5	134.3969
71	134.798	92	134.3328
71.5	134.4018	92.5	134.2007
72	134.6659	93	134.4588
72.5	134.5338	93.5	134.2007
73	134.64	94	134.2447
73.5	134.6075	94.5	134.4649
74	134.5338	95	134.5611
74.5	134.6438	95.5	134.5089
75	134.6252	96	134.3328
75.5	134.6219	96.5	134.2447
76	134.4458	97	134.4209
76.5	134.6045	97.5	134.2007
77	134.582	98	134.3768
77.5	134.4898	98.5	134.2447
78	134.6052	99	134.1567
78.5	134.5906	99.5	134.31
79	134.5779	100	134.2447
79.5	134.6659	100.5	134.2007
80	134.5338	101	134.3768
80.5	134.4458	101.5	134.3328

102	134.3007	123	133.8543
102.5	134.2888	123.5	133.9864
103	134.2152	124	133.9901
103.5	134.0686	124.5	134.1185
104	134.1567	125	134.0745
104.5	134.2007	125.5	134.2506
105	134.2888	126	134.1485
105.5	134.1567	126.5	134.1169
106	134.3119	127	134.0882
106.5	134.4209	127.5	134.0304
107	134.2756	128	134.1625
107.5	134.1567	128.5	133.9424
108	134.2007	129	133.8983
108.5	134.3328	129.5	133.9125
109	134.5089	130	133.9604
109.5	134.2998	130.5	134.0304
110	134.2967	131	133.9911
110.5	134.255	131.5	134.0304
111	134.2447	132	134.2506
111.5	134.2886	132.5	134.1185
112	134.2663	133	134.3386
112.5	134.3328	133.5	134.3826
113	134.2212	134	133.8983
113.5	134.1567	134.5	133.9764
114	134.0246	135	134.1625
114.5	134.0488	135.5	134.0224
115	134.1253	136	133.9424
115.5	134.2888	136.5	134.1185
116	134.2007	137	134.1625
116.5	134.1246	137.5	133.9864
117	133.9174	138	133.8983
117.5	134.1376	138.5	133.8581
118	134.0055	139	133.8103
118.5	134.0495	139.5	133.8543
119	133.9615	140	133.8347
119.5	133.8629	140.5	133.9864
120	133.8134	141	133.6782
120.5	133.7663	141.5	133.7663
121	134.0261	142	133.8605
121.5	134.0004	142.5	133.7663
122	134.0304	143	133.6782
122.5	133.9457	143.5	133.7663

144	133.8103	154.5	133.8543
144.5	133.8543	155	133.6342
145	133.899	155.5	133.8983
145.5	133.9424	156	133.9864
146	133.8543	156.5	134.0304
146.5	133.7946	157	133.9424
147	133.776	157.5	133.9021
147.5	133.8543	158	133.8983
148	133.8103	158.5	133.8543
148.5	133.7889	159	133.8983
149	133.8681	159.5	134.0304
149.5	133.6342	160	133.9253
150	133.8466	160.5	133.9864
150.5	133.8908	161	134.0304
151	133.8604	161.5	133.9424
151.5	133.8147	162	133.6782
152	133.785	162.5	133.7222
152.5	133.5901	163	133.8066
153	133.8983	163.5	133.5901
153.5	133.6782	164	133.6782
154	133.9864	164.5	133.8983
		165	133.6422

B3. Summary of k -plane Data Clustering Method (Bradley and Mangasarian 2000)

The pressure-decline data usually fall into clusters grouped around certain planes. The k -plane algorithm determines k clustering planes that minimize the sum of squares of distances of each given point to a nearest plane.

Let's consider a set of m points in the n -dimensional real space R^n represented by the matrix $A \in R^{m \times n}$. Now we cluster A into k cluster planes in R^n that minimize the sum of the squares of distances of each point of A to the nearest plane. A clustering plane is defined as follows

$$f(x) = w_i^T x + b_i = 0, \quad i = 1, \dots, k \text{ and } x \in R^n \quad (\text{C-1})$$

The k -plane algorithm includes the following steps

1. Randomly select (w_i, b_i) with an assumption that the normal vector w_i is unit norm, i.e. $\|w_i\| = 1, i = 1, \dots, k$
2. Cluster assignment (assigning each point to the closest plane): for each point x , the closest plane is chosen as

$$y = \arg \min_{i=1,\dots,k} |w_i^T x + b_i| \quad (\text{C-2})$$

3. Cluster update (find a plane that minimizes the sum of the squares of distances to each point in a cluster): update the clustering planes (w_i, b_i) by solving

$$\min_{(w_i, b_i) \neq 0} \|A_i w_i + b_i e\|_2^2 \quad \text{subject to} \quad \|w_i\|_2^2 = 1, \quad i = 1, \dots, k \quad (\text{C-3})$$

where $A_i \subseteq A$ is the subset of A belongs to the i^{th} cluster, $\|\cdot\|_2$ means the L_2 norm, and e is a vector of ones of appropriate dimension.

4. Calculation stops if there is a repeated overall assignment of points to clustering planes.

In this study, the value of n equals unity. Considering the nature of pressure-decline data and computation time, the number of clusters (k) equals to 3 or 4.

Appendix C. Composition of Midale Reservoir Brine and Physical Properties of the Surfactants

Please see Tables C-1 and C-2.

Table C-1: Composition of the Midale reservoir brine

Ions (mg/L)	Value
HCO ³⁻	110
Cl ⁻	187 800
SO ₄ ²⁻	793
Ca ²⁺	2990
Mg ²⁺	564
Na ⁺ , K ⁺	107 390
Total Salinity	300 000

Table C-2: Physical properties of the surfactants used in the study (provided by Element Technical Services Inc.)

Surfactant	Molecular Structure	Molecular Weight (g/mol)	Boiling Point (°C)
Polyoxyethylenes		456.68	440.6
d-Limonene		136.23	175.5
Alcohol Polyoxyethylene Ether		230.39	-